Developing Modular Interconnection Techniques for Disassemblable PV Modules

Msc. Sustainable Energy Technology

Mihir Mahajan

Delft University of Technology

TU Delft

Developing Modular Interconnection Techniques for Disassemblable PV Modules

by

Mihir Mahajan

In partial fulfillment of the requirements for the degree of

Master of Science

In Sustainable Energy of Technology

At Delft University of Technology,

To be defended on August 25, 2023, at 10:00

Thesis Supervisor :	Dr. P. Manganiello
Company Supervisor :	Siemen Brinksma
Thesis Committee:	Prof. Dr. I. Gordon
	Dr. M. Cvetkovic
Project Duration :	December, 2022 - August, 2023
Student Number :	5600618
Faculty :	PVMD, TU Delft

TU Delft

BIOSPHERE SOLAR

PVMD Delft University of Technology

Abstract

The remarkable expansion of the PV industry can be attributed to cost reductions and technological advancements, resulting in solar energy becoming an appealing and sustainable option. However, there is a growing concern regarding the environmental impact of disposing decommissioned solar panels. To address this issue, Biosphere Solar, a startup based in Delft, is actively engaged in developing recyclable and repairable solar panels, embracing a circular and sustainable approach. Their ongoing research is centered on solar modules made without EVA lamination, with the goal of facilitating easier disassembly.

A crucial aspect of achieving disassembly of solar cells involves exploring modular interconnections that allow for the disconnection of interconnections between solar cells. Although modular interconnections are already employed in batteries, electrical switches, and communication systems, their potential application in connecting solar cells has not been extensively explored.

This thesis explores various interconnection approaches aimed at facilitating modular interconnections within PV modules constructed using interdigitated-back-contact (IBC) solar cells, following the structure established by Biosphere Solar for PV modules. The objective is to allow for the replacement of damaged solar cells without adversely affecting neighboring functional cells. Four distinct concepts were investigated, each utilizing the dog-bone contact wire to connect IBC solar cells in series. These concepts include a desolderable interconnection using a single dog-bone wire soldered with SnBi (a low melting temperature solder alloy), desoldering between the contact regions of two dog-bones connected through the fusion of tin coatings at overlapping areas, interconnection mechanisms based on contact pressure within a polymer-based cell-bed, and a contact pressure interconnection mechanism based on magnetic force. Both contact pressure interconnection mechanisms involve two dog-bones to create a series connection between a pair of solar cells.

After evaluating the technical feasibility of the aforementioned concepts, prototypes were developed, each incorporating the specified approaches. Furthermore, two reference prototypes were fabricated to establish benchmarks for comparison. Both prototypes employ conventional interconnections with a single dog-bone and SnAgCu solder alloy. The difference lies in the module build-up: one follows the Biosphere Solar approach (without EVA), while the other adheres to the traditional module build-up (with EVA and lamination). For the sake of simplicity, the reference prototype constructed using the Biosphere Solar approach and utilizing the SnAgCu solder alloy is referred to as the 'SnAgCu' prototype, while the one built using EVA lamination is referred to as the 'EVA' prototype.

I-V measurements revealed that the prototypes with single dog-bone based interconnection soldered using the SnBi solder alloy and two dog-bones with molten joint connections achieved the highest efficiencies (21.51% and 21.17%, respectively) compared to the other prototypes based on concepts explored for creating modular interconnections. The improved cell-bed design, which has a screw-based mechanism, showed an increase in efficiency (20.68%) compared to the slider-based mechanism (18.46%). The prototype with magnetic force-based interconnections achieved an efficiency of 19.94%. The two reference prototypes had efficiencies of 21.58% (SnAgCu) and 21.98% (EVA).

All prototypes, except for the one utilizing the slider-based interconnection in the cell-bed, underwent thermal cycle tests. Toward the conclusion of the thermal cycle testing, the prototypes featuring desolderable interconnection mechanisms (a single dog-bone soldered using the SnBi solder alloy and two dog-bones with soldered contact regions) exhibited the highest efficiencies compared to the other prototypes developed to explore potential concepts for modular interconnections.

Contents

List of Figures

List of Tables

CHAPTER 1

Introduction

1.1 Solar Energy Availability and Expansion of the PV Industry

Earth's greenhouse gases are primarily produced through energy production, specifically from the combustion of fossil fuels. In order to achieve the goal of net-zero emissions by 2050, it is crucial to invest in renewable energy sources that are clean, accessible, affordable, sustainable, and reliable [1].

The advancement of solar energy technology has been remarkable since the first public demonstration of a silicon photovoltaic cell in 1954. Over the years, scientists have continuously improved its efficiency and reduced its cost, making solar energy an integral part of the global energy economy [2].

Solar energy can be harnessed in various forms, including solar heat, solar photovoltaic, and solar fuels. It provides humanity with a clean, environmentally friendly, and abundant source of renewable energy [3].

Given the urgency of transitioning to sustainable energy, solar energy stands out as the most promising option due to its year-round availability. Figure 1.1 demonstrates the substantial energy potential of solar power in comparison to finite resources.

The Earth's abundant availability of solar energy has been a driving force behind the significant growth of global photovoltaic installations in recent times.

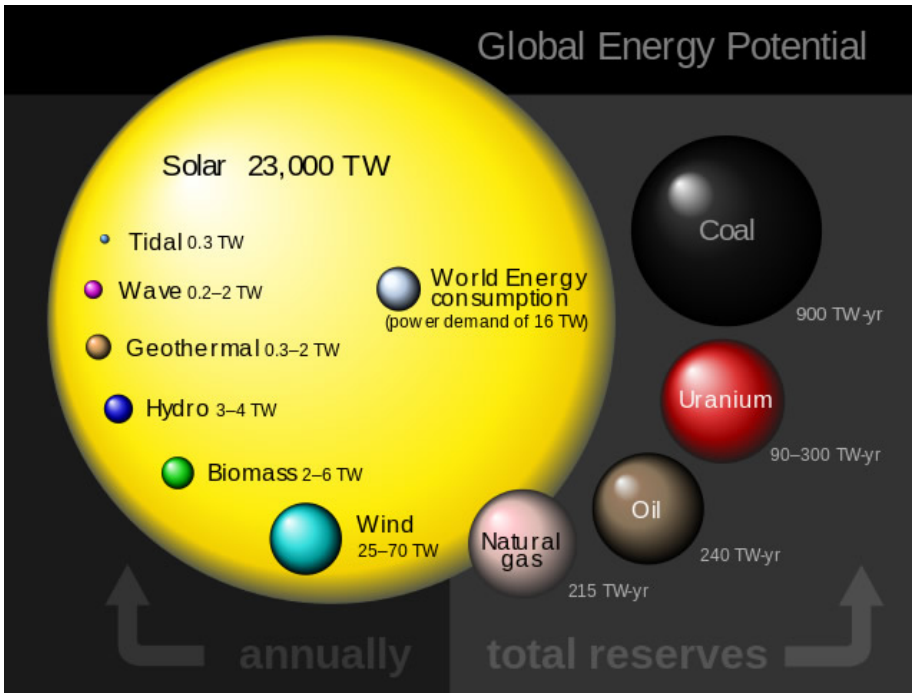

Figure 1.1: Representation of yearly available finite energy resources [4]

1.2 Growth of PV Market

As the global market for PV modules (photovoltaic modules) continues its expansion, the amount of decommissioned PV modules is projected to rise accordingly. Figure 1.2 provides a visual representation of the cumulative PV waste projection in million tonnes and cumulative PV capacity (GW).

This illustration presents two situations:

1. The regular loss scenario: This scenario anticipates a 30-year lifetime for photovoltaic (PV) systems without any premature damages, wear-outs, or replacements. According to this scenario, the total accumulated PV waste worldwide will reach 60 million tonnes by the year 2050 [5].

2. The early loss scenario: This scenario assumes the occurrence of certain failures before the 30-year lifespan is complete. Under this scenario, the global cumulative PV waste is projected to be 78 million tonnes by 2050 [5].

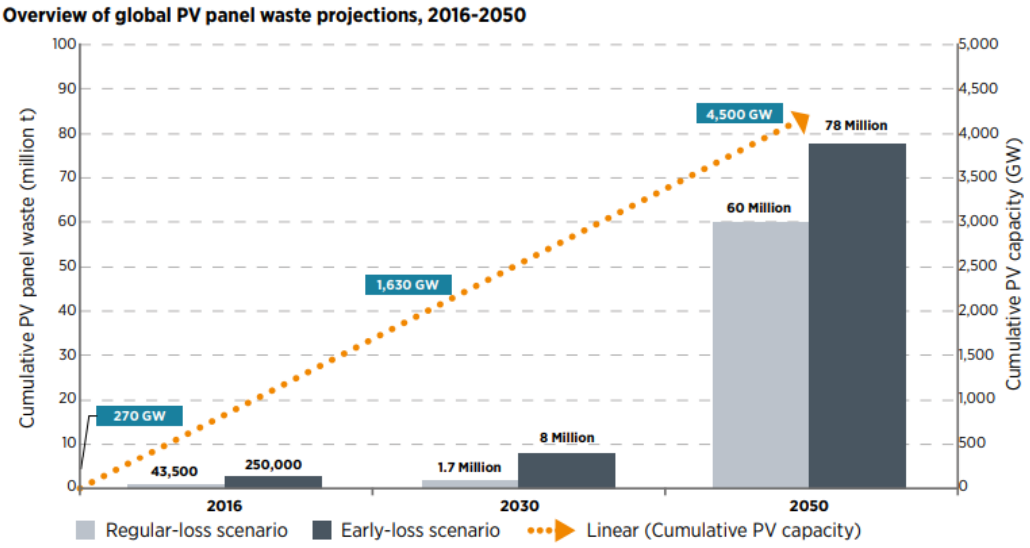

Figure 1.2: Global cumulative PV waste projection [5]

1.3 Global PV Waste and Resulting Negative Externalities

Lead, a hazardous metal, has the potential to accumulate in both humans and the environment. Accumulated lead can negatively affect the immune system, kidney function, and the brain. Ecosystems near lead sources experience adverse effects on vegetation [6, 7].

Crystalline silicon (c-Si) solar panels can contribute to lead leaching. A standard c-Si solar panel contains approximately 12.6 g of lead. The connectivity ribbons are made of lead, and the solar cells are connected with solder. Exposure to low pH, such as nitric acid or rain, causes lead leakage of 13% to 90% of the total lead content in the solar panel. As a result, this leads to a potential of 1.64 g to 11.4 g of lead leaching per solar panel or 75 g to 518 g per ton of solar waste, considering an average weight of a single solar panel to be 22 kg [8].

Assuming a minimum of 60 million tonnes of solar waste by 2050 considering the regular-loss scenario (as shown in Figure 1.2), and multiplying it to the lead leaching in grams per ton solar waste described previously, the total lead leaching in 2050 would be within the range of 4500 to 31080 tonnes.

Negative externalities occur when individuals bear additional costs without having a say in the decision-making process of a production process. For instance, increased industrial waste in a neighborhood can lead to higher healthcare expenses for parents due to pollution-related asthma in their children. These costs, which are not considered by producers, are known as negative externalities [9].

The external cost of air and soil pollution per tonne of PV panels due to lead leaching is 348255 €/t [8]. Considering the regular loss scenario from Figure 1.2 which shows a total of 60 million tonnes of PV waste by the year 2050 and multiplying it with the external cost of lead leaching per tonne of PV waste, the total external cost of air and soil pollution by 2050 due to lead leaching will be approximately 20.89 trillion €.

1.4 Research and Development in PV Recycling

Eventually, PV modules reach the end of their useful lives and need to be replaced. The safe disposal of PV waste has gained attention due to their lengthy lifespans of 30 years or more. Waste management has been established using the 3Rs (reduce, reuse, and recycle), and recycling systems have emerged [10]. It is important to understand the global distribution of PV recycling research, research into the recycling of specific components within a PV module, and approaches to recycle PV modules in order to know the latest trends and research gaps

1.4.1 Global Distribution of Research on Recycling c-Si PV Modules

As discussed in Section 1.3, refraining from recycling PV waste in the future would result in substantial negative externalities and, as indicated by Figure 1.3b, the loss of recyclable materials. This has spurred global research efforts towards solutions for recyclable PV. Figure 1.3a shows that China maintains a dominant position in PV module recycling patents, accounting for half of them due to its high installation rates. Following China, Korea, Japan, Europe, and the US are also actively involved. Corporations are primarily responsible for submitting patents in Europe, France, the United States, China, and Japan, while research institutes contribute most of the patents in Korea. This pattern suggests a strong economic interest in the imminent commercialization of these technologies [10].

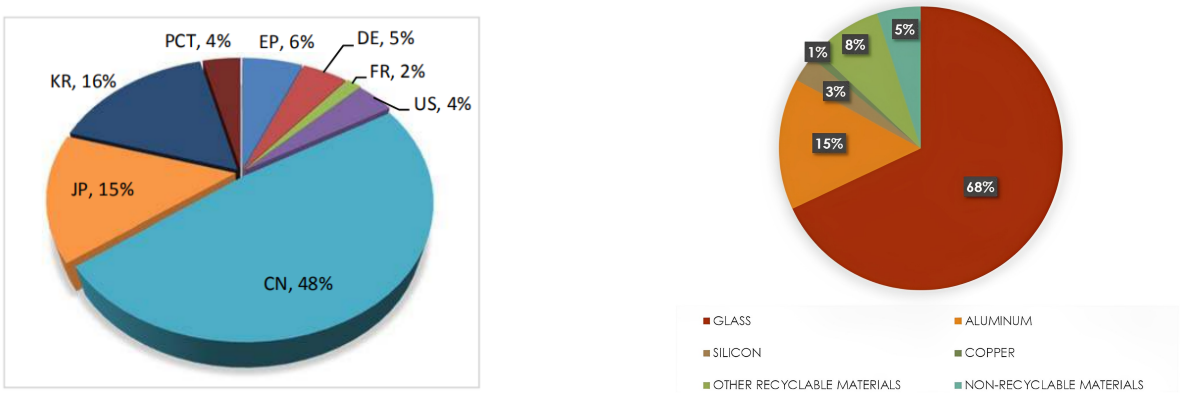

(a) (b)

Figure 1.3: (a) Global Cumulative distribution of patent filings on research for c-Si PV recycling [10], and Composition of recyclable materials in PV panels [11]

1.4.2 Research for Recycling c-Si PV Modules by Material and Components

Before delving into the recycling approaches for PV modules based on materials and components, it is essential to know the fundamental structure of a traditional c-Si solar panel. The conventional c-Si solar panel comprises interconnected solar cells, two layers of EVA lamination (ethylene-vinyl acetate copolymer), which serves as an encapsulant in silicon solar modules to shield cells from stress, cracking, and environmental effects [12], front glass, a back sheet that holds the stack securely in place, and an aluminum frame bonded to the stack using a seal, as depicted in Figure 1.4.

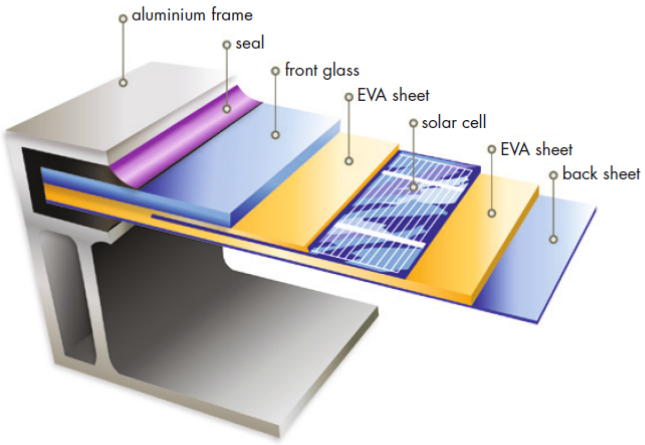

Figure 1.4: Components in a PV module [13]

Due to the strong adhesion applied by the EVA encapsulation to the glass and components within the solar panel, recyclable and reusable resources like aluminum and glass cannot be separated easily. Each c-Si solar panel contains around 10.7 g per Wp of aluminum and 73.4 g per Wp of glass [8]. There are already systems available that can recycle 95-99% of the materials used in PV panels (such as glass, copper, aluminum, etc.). Glass makes up the majority of recyclable elements in PV panels, accounting for 68% of their weight, followed by aluminum (15%), high-purity silicon (3%), and copper wires (1%). The composition of recyclable materials in PV panels is described in the Figure 1.3b. The recovery of the metal components of the panels is complicated and requires extra treatments, which are costly and have an environmental impact. The major PV panel manufacturers have experimented with numerous technologies for the separation and recovery of various materials obtained from PV panels at the end of their life [11]. Physical treatments (shredding with separation by density or magnetism of metals), chemical treatments (acid/alkaline attack or dissolving with organic solvents), and thermal treatments were examined (pyrolysis, incineration and melting of polymeric materials). To date, comprehensive recycling of all components is not done. Numerous ongoing research efforts such as the RESIELP (recovery of silicon and other materials from end of life PV panels) are working in this direction [11]. Encapsulant removal from the module is difficult and can be accomplished via thermal, mechanical, or chemical methods. Metals collected from c-Si cells can be recovered chemically via etching or refining [10].

PV module recycling involves disassembling, separating, and recovering components like frames, encapsulants, cells, and copper ribbons. Figure 1.5 shows that the most interest in recycling is for EVA processing, followed by frames and cells, but less for copper ribbon recovery [10].

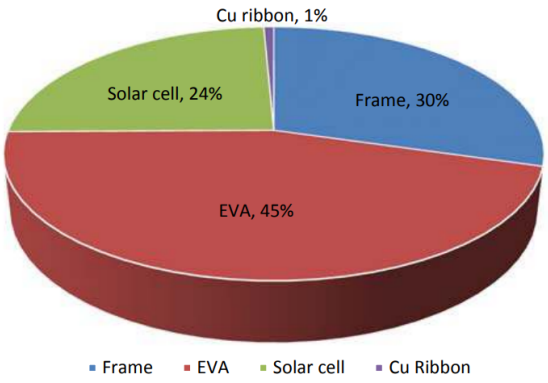

Figure 1.5: Patent filings categorized by targeted components [10]

Recycling c-Si and composite PV modules varies in efficiency, cost, and environmental impact. Procedures for c-Si and compound modules vary based on metal composition and module structure. Delamination of encapsulant is crucial, and various techniques, including thermal, mechanical, and chemical, are being researched for efficient and cost-effective recycling [10].

In the 1990s, the primary goal of c-Si PV module recycling began, with the main objective of recovering intact Si cells for reuse. One method involved a thermal approach, wherein modules were heated in a furnace at temperatures between 500-600°C in two phases, causing the polymer components to break down or burn. Several companies, such as Solarworld, Sharp, and AGC, have tested this technique. Soltech, on the other hand, utilizes a fluidized bed to expedite the recovery of silicon cells. Following the process, the silicon cells are recycled into wafers through etching, which can then be used to create new wafers. However, despite these efforts, this approach has not been commercialized due to financial limitations and a lack of demand for module recycling [10].

1.4.3 Latest Trends in PV Recycling Research and Development

Recent trends in PV recycling research and development have looked into mechanical and new chemical methods for component separation. The most current trends in research and development for recycling PV are depicted in Figure 1.6.

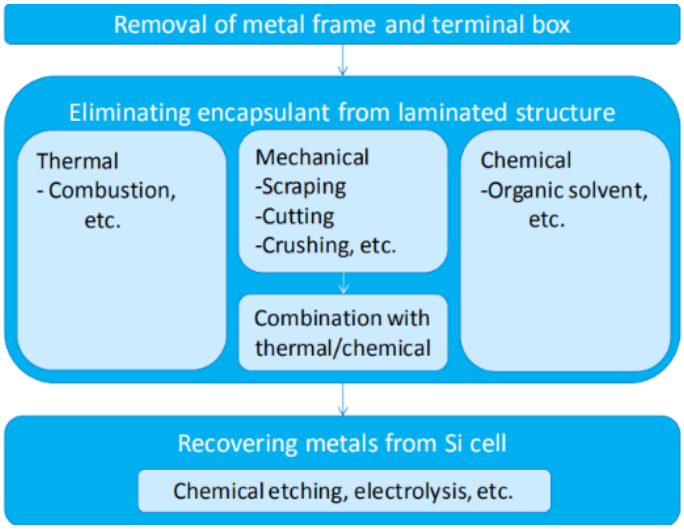

Figure 1.6: Current trends in research and development for recycling PV [10]

Mechanical methods for recovering glass from waste PV modules involve crushing, scraping glass or layers, and cutting the encapsulation layer. Companies such as Mitsubishi Materials, Toho Kasei, Hamada Corporation, and NPC Inc. are researching processes for recovering glass through scraping and

cutting. In Europe, the Full Recovery End of Life Photovoltaic (FRELP) project incorporates procedures for recovering glass, combusting polymers, and recovering metals from Si cells and electrodes using heating and milling equipment [10]. Several organizations and research institutes have been investigating the recycling of PV modules through thermal and chemical processes. The thermal approach shows potential in recovering glass and silicon (Si) cells without damage. The Korea Institute of Energy Research (KIER) is focused on recovering Si cells and metals, while the Korea Electronics Technology Institute (KETI) utilizes thermal and chemical etching processes to recover Si cells. Chonnam National University employs thermal and chemical etching to recover metals, while the Chinese Research Academy of Environmental Sciences (CRAES) uses a tube furnace for combustion and chemical treatment. The Industrial Technology Research Institute, Taiwan (ITRI), along with other research entities, explored a heating method involving PVF (Polyvinyl Fluoride) backsheets. These technologies are being developed further to enhance the recycling of PV modules [10].

Currently, the primary research focus is centered on end-of-life PV recycling, which often disregards the potential benefits of repair, refurbishment, and extending the operational lifespan of PV modules. The average annual failure rate for PV panels is low, with approximately 5 panels out of 10,000, or 0.05%, experiencing issues [14]. As the demand for PV installations increases worldwide, the number of decommissioned solar panels due to failures before reaching their end-of-life is expected to rise. This emerging trend presents a unique opportunity for the development of repairable and upgradable solar panels.

1.4.4 Alternative Approaches for Facilitating Recycling in Photovoltaic Modules

Another way to make PV modules easy to recycle is to modify the structure of the PV module itself. In this section, such approaches are briefly discussed.

Double Encapsulated Modules with a Release Layer

Using double-encapsulated modules with a release layer is one way. A clear coating that does not cling to the PV cells is utilized. It sits between the cells and the EVA encapsulation. EVA encapsulation is also utilized to seal the gaps between the cells. Polyethylene Terephthalate (PET) is mentioned as the sole suitable material because it is transparent and easily removed from cells. The structure of double-encapsulated modules with a release layer is depicted in Figure 1.7. Prototype tests have demonstrated that the cell may be easily recovered by cutting up the back of the module using a knife. Nevertheless, the additional coating degrades the qualities. In the test, light transmission reduces by 3.7-4.2%, while the reflection increases by 3.4-3.7% in the test [15].

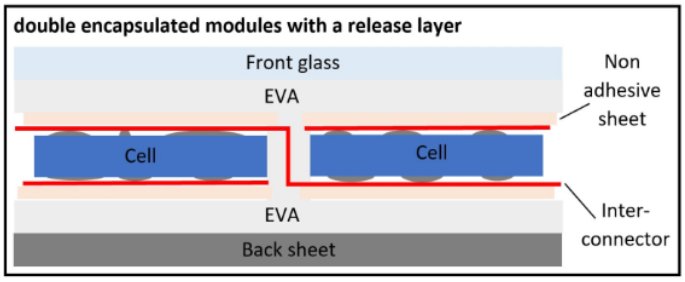

Figure 1.7: Structure of PV module with release layer [15]

NICE Technology

Another method in development is the substitution of encapsulant with nitrogen gas. The company Apollon Solar is developing this concept known as NICE technology ("New Industrial Cell Encapsulation"). The idea draws on tested sealing technology from the insulating glass sector. In the module, nitrogen gas is employed instead of encapsulating material. The cells are surrounded by a front and a back glass. The module stack is sealed with a polyisobutylene (PIB) seal and an extra layer of silicone. NICE PV modules have solder-less cell interconnections, in which bare copper ribbons are mechanically pushed onto the PV cell contacts inside the module as shown in Figure 1.8, which depicts the structure of NICE PV module. The NICE PV modules perform well in IEC certification tests, showcasing low power losses and sometimes even a power increase. Thermal cycling tests have been validated with minimal power loss, and mechanical loads and outdoor exposure tests have shown little to no degradation [16].

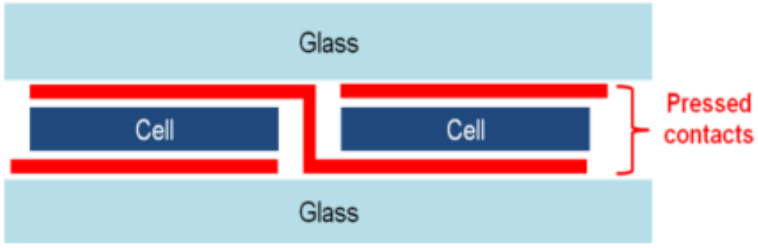

Figure 1.8: Structure of NICE PV module [16]

1.5 Biosphere Solar and the Role of Modular Interconnections

As discussed in Subsections 1.4.2 and 1.4.3, ongoing research explores various thermal, chemical, and mechanical techniques for PV module recycling. The precision demanded by these processes to prevent harm to other components adds to their inherent complexity.

Founded in 2020 by a group of TU Delft students, Biosphere Solar aims to develop recyclable, repairable, and reusable solar panels. Their vision is to instill a sense of responsibility for PV recycling within the community and customer base. The mission of Biosphere Solar is to introduce circularity and equitable standards to the PV market and industry. Their recycling strategy involves designing easily disassembled solar panels, facilitating subsequent recycling and repair.

Figure 1.5 illustrates, significant interest in PV recycling centers around EVA processing. Addressing this, the company focuses its research on eliminating the need for EVA encapsulation and instead creating EVA-free glass-to-glass PV modules. This approach also aims to simplify the intricate thermal, chemical, and mechanical processes outlined in Subsection 1.4.3. The importance of streamlining these processes lies in achieving more process efficiency, reduced costs, and enhanced safety.

To bond the front and back glass, Biosphere Solar are using Polyisobutene (PIB) as an edge sealant for solar PV panels. PIB acts as a protective sealant for the glass, effectively delaying moisture infiltration. This protection helps prevent corrosion and deterioration of conductive oxide coatings on cells, connectors, and other components. Moreover, PIB enhances electrical isolation and reduces module degradation [17].

Instead of using EVA encapsulation to hold the solar cells in place, the approach involves using cell beds or spacers to hold the c-Si solar cells.
Figure 1.9 provides schematic comparing the structures of the Biosphere solar PV module and the conventional PV module.

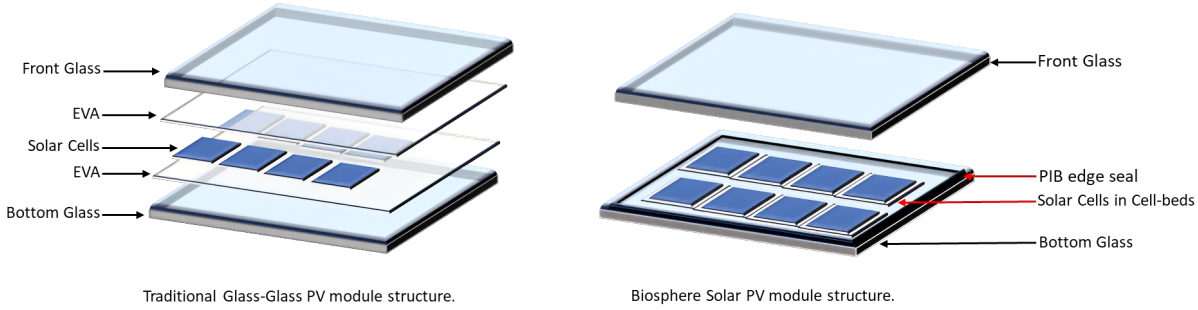

Figure 1.9: Comparison of conventional PV design and biosphere PV design

The function of modular interconnections is to enable the disconnection of solar cells that are damaged by shading, cracks, or other factors within a solar panel, facilitating their easy replacement. Moreover, this process permits the substitution of old cells with new ones when the PV module reaches its end-of-life, thereby prolonging the overall operational lifespan of the module.

The utilization of modular interconnections is contingent upon the particular product and the knowledge or experience of individuals in the repair process. Biosphere Solar is actively involved in developing two products: the standard PV module (depicted in Figure 1.10a during its prototype phase) and the DIY (Do it yourself) kit (shown in Figure 1.10b, representing the prototyping phase).

(a) (b)

Figure 1.10: (a) Biosphere Solar PV module prototype attached to a wooden frame for mechanical load tests, and (b) Prototype of DIY kit designed by Biosphere Solar

The Biosphere Solar PV module prototype, depicted in Figure 1.10a, follows a similar construction approach as the Biosphere Solar PV module structure shown in Figure 1.9 with the exception of not having the cell beds. This module is made using interdigitated-back-contact (IBC) solar cells.

In contrast, the DIY kit presented in Figure 1.10b which is made using half-cut IBC solar cells, targets makers, hobbyists, and serves as an educational tool. This specific audience may lack specialized skills in niche disassembly methods. Therefore, it is essential to employ a user-friendly modular interconnection method that simplifies the disassembly process. This approach enables individuals without extensive training to dismantle the module safely, without compromising critical components.

1.6 Research Questions and Report Outline

Research Questions

The objective of this thesis is to explore potential materials and mechanisms that can enable modular interconnections for solar cells within the Biosphere Solar PV modules. To achieve this goal, specific research questions need to be addressed. The research questions are as follows:

1. Is it possible to desolder the interconnection and separate the damaged solar cell without harming the adjacent solar cells?
2. What strategies can improve the cell-bed-based interconnections that utilize contact pressure?
3. Which materials and mechanisms can offer high contact pressure, ensuring strong and uniform interconnection while permitting easy disassembly?
4. How do the contact pressure-based interconnection mechanisms and desolderable interconnections perform compared to the conventional interconnection mechanism?

Through the investigation of these research questions, the thesis aims to identify and propose solutions that enable the easy to connect interconnections which allow easy and damage-free disassembly.

Report Outline

The forthcoming chapters address the aforementioned research questions.

Chapter 2 explains the relevant theoretical concepts necessary for this thesis.

Chapter 3 delves into the concepts explored for the development of modular interconnections. It outlines the concept of desolderable interconnection, which involves soldering a single interconnection wire with the SnBi solder alloy, known for its low melting point (Section 3.1.1), and introduces the idea of soldering two interconnection wires to connect a pair of solar cells in series (Section 3.2). Additionally, the chapter discusses the existing cell-bed design with a slider mechanism, describing its visible limitations (Section 3.3.1), and presents the concept of utilizing magnetic force to create contact pressure-based interconnections (Section 3.4).

In Chapter 4, the methodology used to assess the technical feasibility and characterize the performance is explained.

Chapter 5 describes the testing of assembly and disassembly for the concepts explained in Chapter 3 and the prototyping processes. It also describes the improvement of the cell-bed design to enhance the electrical performance of interconnections (section 5.3), and describes the reference prototypes in section 5.5.

Experimental tests conducted to gain insights into the performance of the prototypes are discussed in Chapter 6. This chapter briefly describes the setup used for I-V measurements in section 6.1 and elaborates on the analysis of I-V characteristics for all the prototypes in section 6.2. It also includes a comparison of the electrical performance of the reference prototypes with each other and with the prototypes incorporating modular interconnections based on the explored concepts. Additionally, the analysis and comparison of series resistance and performance characteristics obtained for all the prototypes will be described in subsection 6.2.9. The thermal cycle test plan and setup are explained in section 6.3, and the outcomes of the thermal cycle test, including visual observations, EL images, and electrical performance measurements, are presented in section 6.4. Furthermore, a comparison of power-loss observed for all the prototypes that underwent the thermal cycle test is covered in section 6.4.7.

Finally, Chapter 7 concludes the report by providing a concise summary of the thesis outcomes in section 7.1. Additionally, it presents recommendations and identifies future research areas, including developing modular interconnections for front contact solar cells and Zebra IBC solar cells, improving the optical performance of the Biosphere Solar PV modules, and reducing solar cell warping during thermal cycle test (section 7.2).

CHAPTER 2

Theory

In this chapter, the theoretical concepts essential for the thesis are discussed. The chapter begins by explaining the basic working principle of a solar cell, followed by an explanation of the equivalent circuit of a solar cell. Next, the concept of series resistance in solar cells and their interconnections is covered. The chapter then describes the impact of series resistance on I-V measurements, concluding with a brief explaination of the IBC solar cell structure.

2.1 Working Principle of the Solar Cell

Figure 2.1 depicts a simplified solar cell exposed to sunlight, functioning based on the photovoltaic effect. The cell is constructed by combining oppositely doped materials, creating a depletion region between them. When illuminated, the cell generates electron-hole pairs, which are separated by the electric field formed by the opposite polarities. Electrons move towards the n-type region, while the holes move towards the p-type region.

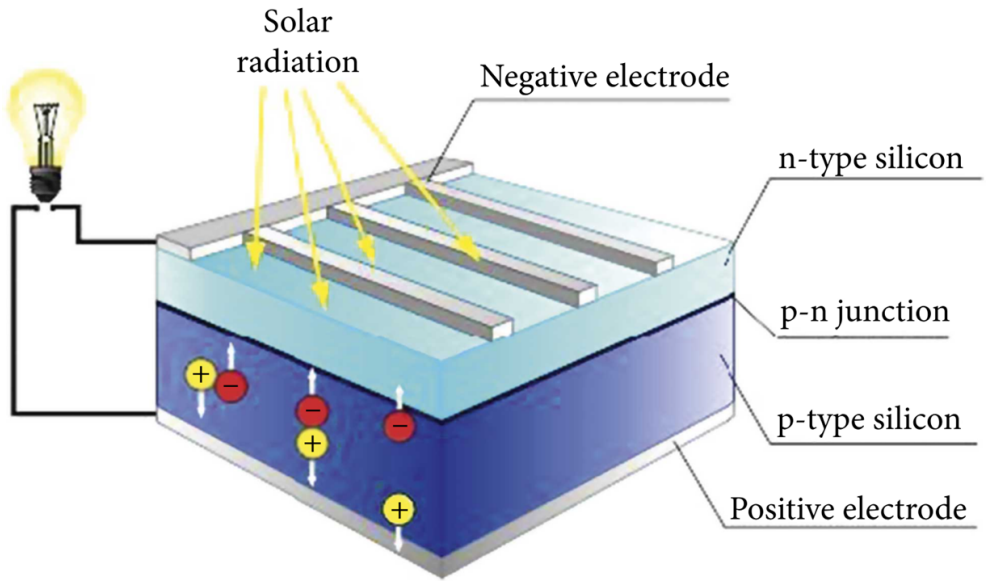

Figure 2.1: Schematic representation of a solar cell [18]

The operation of a solar cell can be broken down into three phases. Initially, when photons interact with the semiconductor p-n junction, electron-hole pairs are created if the photon's energy surpasses the bandgap energy of the semiconductor. Any surplus energy is emitted as heat. In the next step, the charge carriers are divided: the holes migrate through the p-type region and get collected in the positive electrode, while the electrons travel through the n-type region and get collected in the negative electrodes. These electrons can be utilized to supply power to an electrical circuit, which is connected to the terminals of the solar cell, before recombining with the holes.

An external circuit can be connected to the solar cell's electrodes, allowing charges to accumulate and flow through, producing a usable current. Multiple interconnected cells form a module which can be installed on rooftops or other locations to harness solar energy from the sun.

2.2 Equivalent Circuit of a Solar Cell

Figure 2.2 showcases the circuit diagram of the single diode equivalent solar cell. The equivalent circuit comprises a current source, a diode, and resistances.

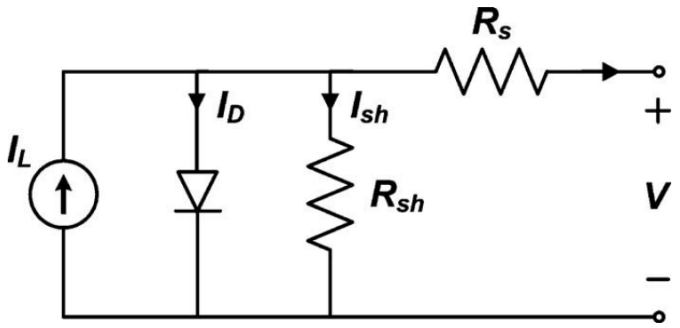

Figure 2.2: Equivalent circuit of a solar cell [19]

In the circuit diagram shown in Figure 2.2, the shunt resistance, represented by R_{sh}, accounts for alternative paths where current can flow between the front and back surfaces due to mechanical defects and material dislocations. It is preferable to have a higher shunt resistance, as it indicates fewer current paths and fewer defects within the cell [19].

The series resistance, denoted as R_s, represents the resistance encountered by the current flow between the semiconductor layer and the two contacts connecting to the external circuit. Ideally, the series resistance should be kept as low as possible, to create easier flow of the charge carriers [20].

The current generated by illumination in the cell is referred to as photocurrent and is represented by I_L. Finally, the current flowing through the diode is identified as I_D [19].

The current flowing through the external load, denoted as I, can be determined by the following equation derived using Kirchoff's current law,

$$I = I_{\mathrm{L}} - I_D - I_{\mathrm{sh}} \tag{2.1}$$

The Shockley diode equation, which provides the current density at a given applied voltage is as follows:

$$I(V_{\mathrm{a}}) = I_{\mathrm{rec}}(V) - I_{\mathrm{gen}}(V) - I_{\mathrm{ph}} = I_{\mathrm{o}}\left[exp^{\frac{qV}{nKT}} - 1\right] - I_{\mathrm{L}}. \tag{2.2}$$

Substituting equation 2.2 and applying Ohm's law to equation 2.1, the following equation is obtained:

$$I = I_{\mathrm{L}} - I_{\mathrm{o}}\left[exp^{\frac{qV}{nKT}} - 1\right] + \frac{V - IR_{\mathrm{s}}}{R_{\mathrm{sh}}} \tag{2.3}$$

Where, I_o represents the reverse saturation current, which accounts for the diffusion and recombination of electrons and holes. The voltage of the cell is denoted as V [20].

The ideality factor (n) is a crucial parameter that indicates how closely a solar cell behaves like an ideal diode (where n=1). Hence, the ideality factor plays a significant role in determining the electrical behaviour of solar cell devices [21].

The constant K corresponds to Boltzmann constant (1.381×10^{-23} J/K) and q represents the charge of an electron (1.602×10^{-19} C) [20].

2.3 Series Resistance

The series resistance in a solar cell is primarily influenced by three factors: the bulk resistance of the material, the contact resistance at the junction between the semiconductor and metallization, and the resistance of the metal [22]. Busbars and fingers play crucial roles in solar cells by connecting and transporting electrical current. Busbars, which are thick conductive strips or ribbons, serve as main pathways for collecting current from multiple regions and transferring it to the external circuit. Meanwhile, fingers are thin and narrow conductive lines that collect current from the emitter and transport it to the busbars. Together, these components ensure efficient current flow and effective current collection in solar cells.
Figure 2.3 shows the direction of electron flow and series electrical resistance components which exist within the solar cell.

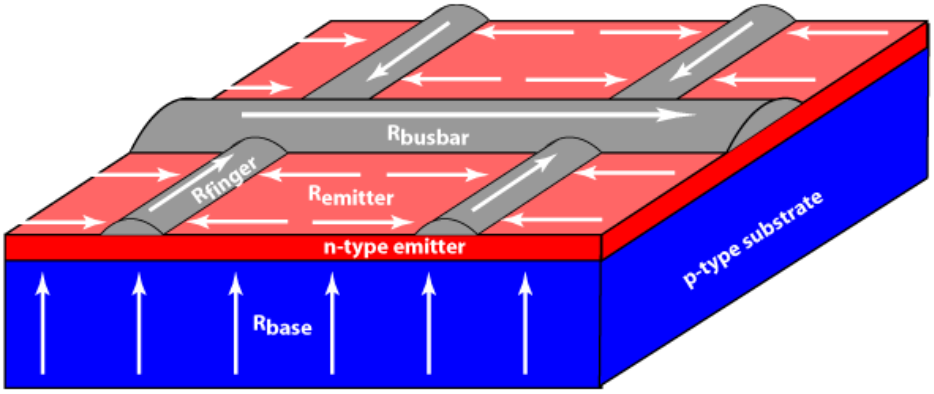

Figure 2.3: Direction of electron flow in a front-contact solar cell [23]

The Figure above illustrates that electrons move from the Base layer (p-type) to the Emitter layer (n-type), during which they encounter electrical resistance R_{base}. This resistance arises due to both the bulk properties of the base material and the specific material properties of the layer.

After reaching the n-type emitter layer, the electrons travel to the top and start moving horizontally towards the fingers. During this movement, they counter electrical resistance of the emitter layer denoted as $R_{emitter}$.

The emitter resistance varies depending on the distance from the electron's collection in the emitter to the contact point of a finger. Shorter the distance between the emitter and the metal contacts which an electron needs to travel, lower the emitter resistance.

The electrons get collected in the fingers and start moving towards the busbars. The fingers and the busbars have their own electrical resistance denoted by R_{finger} and R_{busbar} respectively. After the electrons are collected in the busbar, they travel horizontally across it. To connect two solar cells in series, the busbars on the top of a cell (negative terminal) must be connected to the busbars on the bottom of another solar cell (positive terminal).

The electrical resistance of a material is influenced by its resistivity, as well as the length and cross-sectional area of the conducting medium. This relation can be described by the equation [22]:

$$R = \rho \cdot \frac{L}{A} \tag{2.4}$$

Where R represents the resistance, ρ denotes the resistivity, L represents the length, and A represents the area.

2.3.1 Series Resistance due to Interconnections

The process of connecting two solar cells is called interconnection. Equation 2.4 clearly indicates that the interconnection material and design have a crucial role in determining the series resistance within a PV module.

Figure 2.4 shows the tabbing interconnection connecting two solar cells in series.

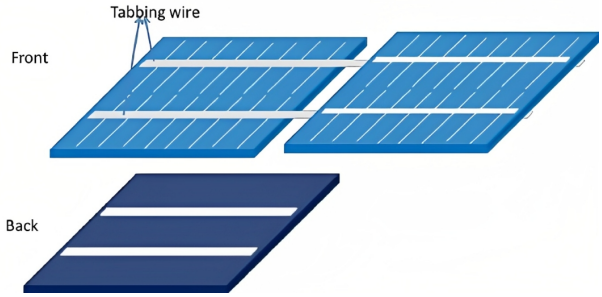

Figure 2.4: Interconnection of two solar cells [24]

A series connection involves connecting front busbars of one cell to equivalent rear busbars of the next cell using flat copper conductors with pre-soldered surfaces. These copper busbars and tabbing ribbons are made of OFHC (oxygen-free high conductivity) copper. The copper is "dead soft," making it easy to bend and solder to the cells without applying much mechanical stress on to the cell [25]. In tabbing wires (Figure 2.4), the series resistance depends on wire length, wire material resistivity, and wire surface area, as described by equation 2.4. The series resistance increases as the length of the wire increases. This is because a longer wire offers more resistance to the flow of current. On the other hand, the series resistance decreases with an increase in the width and thickness of the tabbing wire. Wider and thicker wires have lower resistance due to their larger cross-sectional area, which allows for easier flow of current.

Another important factor that can contribute to series resistance is the type of solder joints utilized to establish contact between the interconnection wires and the solar cell. The resistivity of the solder alloy and the characteristics of solder joints are additional factors influencing series resistance. Asymmetric solder interconnects cause varying electrical resistance across contact microregions, leading to significant electromigration damage [26]. Solder joint shape is influenced by soldering techniques, temperature, alloy brittleness, stress, and thermal expansion coefficient mismatch, contributing to cracks and deformations in the joint microstructure [27, 28, 29] as shown in Figure 2.5.

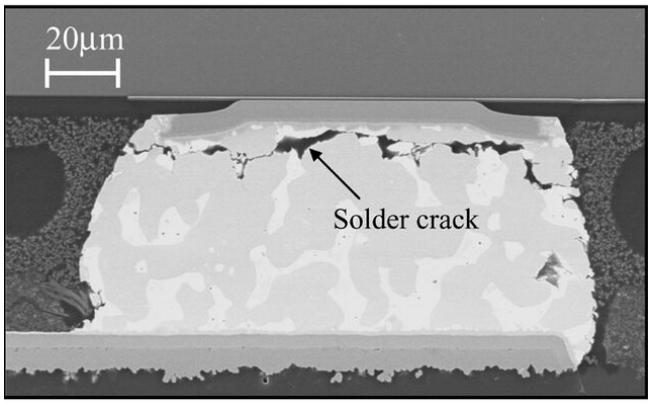

Figure 2.5: SEM image of 63Sn–37Pb flip chip solder joint with crack [30]

2.3.2 Electrical Contact Resistance (ECR)

Understanding the development of contact resistance is vital in interconnections, whether they involve the physical contact of conducting wires or the utilization of solder joints. Electrical contact resistance refers to the resistance encountered by current as it flows through the point of contact between two conducting materials. In electrical connection applications involving plug-in connectors, screw connections, and solder joints, minimizing ECR is advantageous for reducing electrical losses [31].
The formation of ECR occurs when two components are mechanically brought together, as depicted in the provided Figure 2.6.

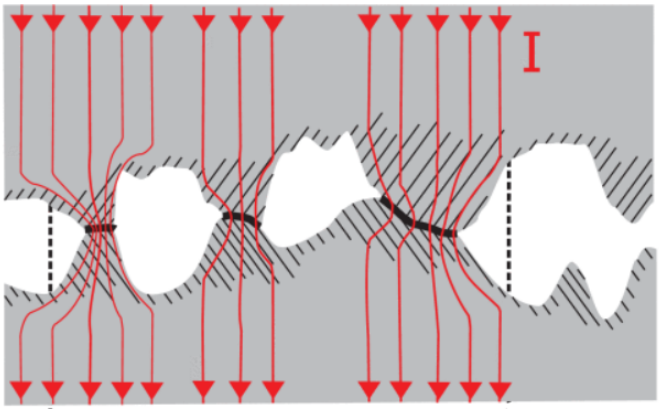

Figure 2.6: The formation of electrical contact resistance (ECR) between two surfaces with rough textures [31]

ECR depends on two factors: surface roughness and waviness, leading to a smaller real contact area compared to the apparent contact area. This creates localized contact spots, limiting current flow [31].

Cracks in solder joints can increase the ECR. When cracks occur, they create gaps or interruptions in the electrical path, leading to increased series resistance. However, electrical contact resistance is more noticeable in physically pressed electrical connections compared to soldered joints due to the direct physical pressure causing irregularities at the contact interface, which can hinder electron flow. In soldered joints, the molten solder helps create a smoother and more uniform contact, reducing resistance.

2.3.3 Electrical Power Dissipation Caused by Series Resistance

The power loss can be understood through the following equation based on Ohm's law [22],

$$P_{\text{loss}} = I^2 \cdot R_{\text{s}} \tag{2.5}$$

Which states that power loss P_{loss} is equal to the square of the current (I) multiplied by the series resistance (R_s). Since power is directly proportional to the product of current and voltage, any voltage drop caused by the series resistance results in a decrease in the overall power output.

2.4 Current-Voltage Characteristics of a Solar Cell

The presence of series resistance impacts the performance of a PV module, which is evident in Current-Voltage (I-V) measurements. Understanding I-V measurements and associated performance parameters is crucial to grasp the role of series resistance.

The I-V characteristics of a PV module play a crucial role in determining important parameters such as open-circuit voltage (V_{oc}), short-circuit current (I_{sc}), and output power.

Figure 2.7 depicts the I-V and P-V (power-voltage) curves, illustrating the relationship between current, voltage, and power output of the solar cell

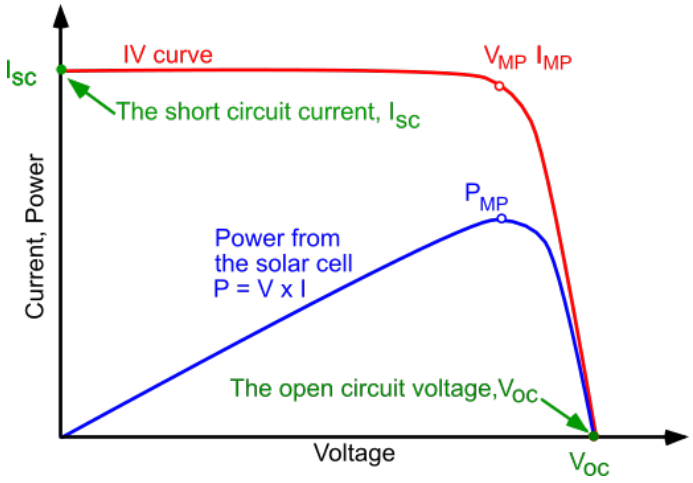

Figure 2.7: I-V and P-V curves of a solar cell connected in forward bias [32]

The open-circuit voltage (V_{oc}) can be defined as the highest voltage observed across a solar cell when there is no current flowing. Similarly, the short-circuit current (I_{sc}) represents the maximum current that flows through the cell when the voltage is zero. Using the measured values of current and voltage, we can calculate the maximum power output of the solar cell, represented graphically by the equation P = V · I. Plotting the power curve allows us to pinpoint the peak power output (P_{max} or P_{mp}) of the PV module. This peak indicates the corresponding voltage (V_{max} or V_{mp}) and current (I_{max} or I_{mp}) values, providing us with the ideal operating conditions for the solar cell.

Fill Factor: The fill factor (FF) measures the efficiency of a solar cell or module in converting sunlight into electrical energy. It is calculated by dividing the maximum power output (P_{mp}) by the product of open-circuit voltage (V_{oc}) and short-circuit current (I_{sc}) [22]:

$$FF = \frac{P_{\text{mp}}}{V_{\text{oc}} \cdot I_{\text{sc}}} \tag{2.6}$$

A higher fill factor indicates a more efficient device, indicating the solar cell's ability to effectively utilize available power. In practical scenarios, an increase in recombination, series resistance, and a decrease in shunt resistance lead to a reduction in the fill factor [22].

Conversion Efficiency: The calculation of the conversion efficiency (η) involves the division of the maximum generated power by the incident power, as expressed in the following formula [22]:

$$\eta = \frac{P_{\text{mp}}}{P_{\text{in}}} = \frac{V_{\text{mp}} \cdot I_{\text{mp}}}{P_{\text{in}}} = \frac{V_{\text{oc}} \cdot I_{\text{sc}} \cdot FF}{P_{\text{in}}} \tag{2.7}$$

Here, P_{in} is the input power to the solar cell. It refers to the total amount of power from the incident sunlight that the solar cell receives.

2.4.1 Impact of series resistance on I-V Characteristics

Figure 2.8 depicts the effect of increased series resistance on the I-V curve. As the series resistance increases, the I-V curve exhibits a steeper slope, indicating a reduction in the fill-factor and a consequent decrease in the maximum power output available to the load. At open-circuit voltage, the solar cell remains unaffected by series resistance as there is no current passing through the external circuit. However, as the solar cell approaches its open-circuit voltage, the presence of series resistance becomes prominent and considerably influences the IV curve.

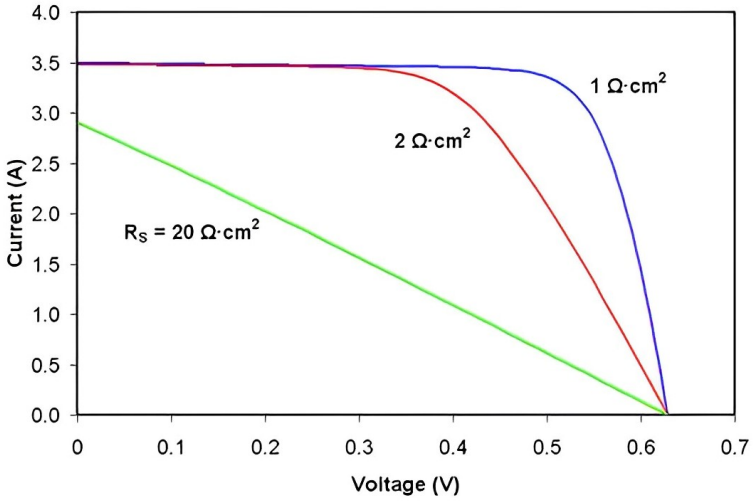

Figure 2.8: Impact of series resistance on I-V curve [33]

By examining Figure 2.8, it becomes apparent that the short circuit current drops at larger series resistance.

2.5 Losses due to Metallization and Interconnections

As described in Section 2.3, busbars and fingers in a solar cell are both essential parts for conducting and distributing the electricity produced by the PV cells. Figure 2.9 depicts the standard busbar and finger topology.

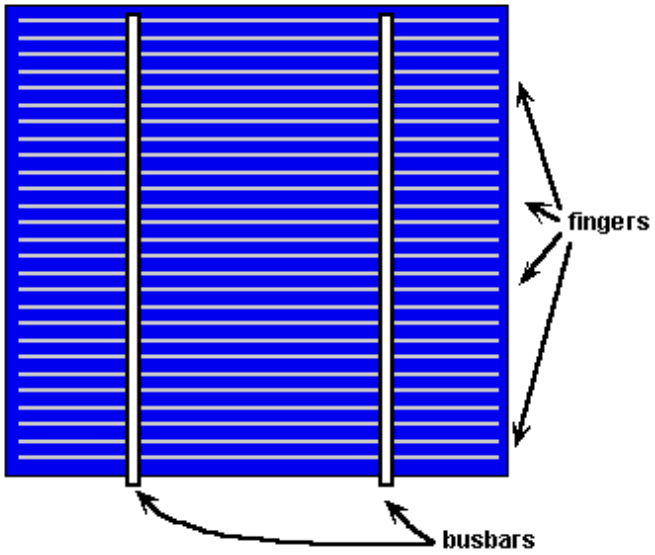

Figure 2.9: Busbars and fingers on a solar cell [34]

The distance between consecutive fingers, commonly referred to as finger-spacing, and the length between fingers and busbars are the two most important factors in determining the electrical resistance in fingers (length of the finger). This is due to the fact that the distance an electron must travel is described by both finger-spacing and finger length.

By multiplying the thickness of the finger by its width, the cross-sectional area of the fingers can be calculated. It is clear from equation 2.4 that enlarging the fingers can reduce their overall electrical

resistance. However, increasing the width of the finger reduces the area that is shade-free on top of the solar cell. This implies that there is always a trade-off between electrical resistance and shading losses.

Figure 2.10 illustrates the trade-off by comparing fractional power loss with the finger spacing and finger width.

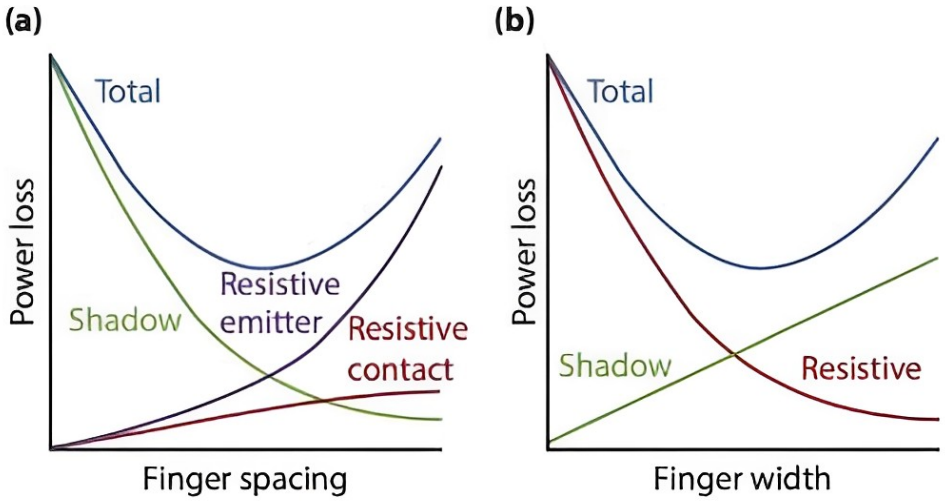

Figure 2.10: (a) Fractional power loss vs finger spacing, and (b) Fractional power loss vs finger width [22]

When it comes to busbars, the electrical resistance is linearly correlated with busbar length and can be decreased by making the busbar wider and taller. However, the trade-off between electrical resistance and shading losses applies to it similar to the fingers [35].

2.6 Smartwire Contacting Technology

Research aiming to reduce electrical and shading losses caused by front contact metalization has yielded various solutions, including the SmartWire Contacting Technology (SWCT). The SWCT employs thin copper wires coated with a low-melting-point alloy, supported by a polymer foil (Figure 2.11). During module lamination, the alloy layer liquefies, establishing a soldered connection to the cell's metallization. This technology, initially introduced by Day4 Energy, serves as a replacement for conventional busbars and ribbons [36].

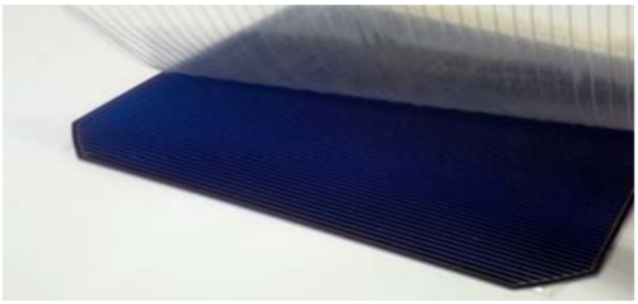

Figure 2.11: Polymer sheet embedded with fingers [36]

The SWCT offers greater reliability, less silver usage in cell metallization, and improved module performance. It uses numerous wire connections, reducing ohmic losses and power loss. This allows for fine-line metallization, reducing shadowing losses and silver usage by 85% or more. The SWCT also contains 1000-2000 electrical contact points, eliminating the need for busbars and soldering pads [36].

Figure 2.12 shows how the polymer sheet enables interconnection with the front side of one solar cell and the back side of the adjacent solar cell.

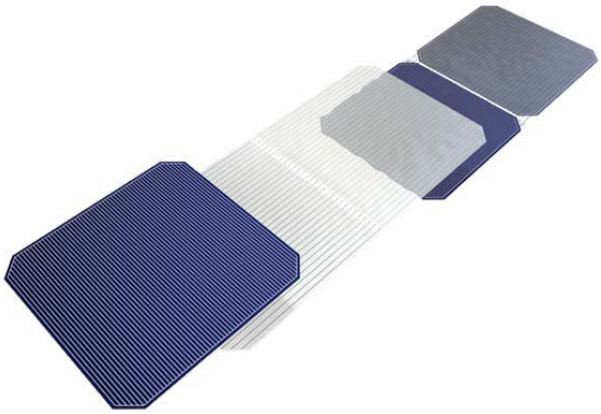

Figure 2.12: SWCT integration in solar cells [36]

The SWCT interconnection method utilizes a Sn-In alloy coating on copper wires, which reduces thermo-mechanical stress on cells due to its lower melting temperature. This method typically operates at temperatures between 140 °C and 160 °C, which is lower than the soldering temperature used in busbar-ribbon technology. However, it relies on the use of indium (In), which is an expensive material. As an alternative approach, a tested technique involves substituting Sn-Bi alloy for Sn-In alloy [36].

2.7 IBC Solar Cells

The interdigitated back contact (IBC) cell, a promising solar cell technology developed in 1975, offers significant advantages. By positioning both metal contacts on the backside of the cell (as shown in Figure 2.13(a)), shading losses on the front side are eliminated. This eliminates the trade-off between shading losses and series resistance. Moreover, the IBC structure enables independent optimization of the front and back of the cell's architecture. The IBC structure brings notable benefits, including the ability to use wider metal contacts without shading losses [37, 38].

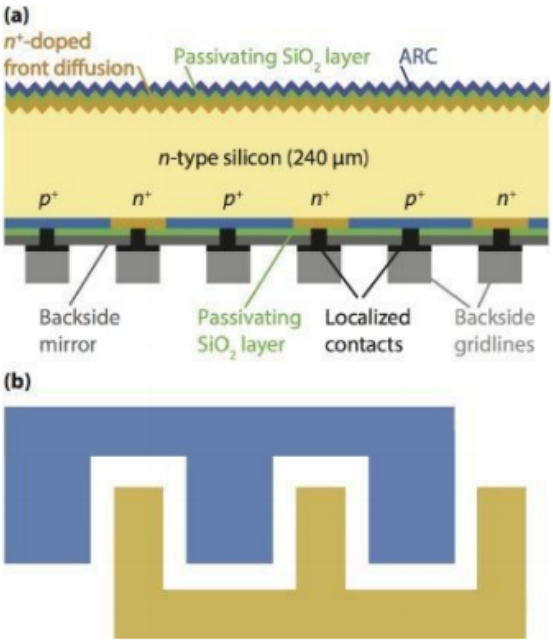

Figure 2.13: (a) Schematic structure of an IBC solar cell and (b) back-side metallization pattern [22]

The back metallization of an IBC solar cell are arranged in a grid-like configuration, with the positive and negative contacts alternating in rows (as shown in Figure 2.13(b)). The semiconductor-metal interfaces are kept as small as possible in order to reduce the undesired recombination at this defect-rich interface [22].

Figure 2.14 shows the front and back side of the IBC solar cell

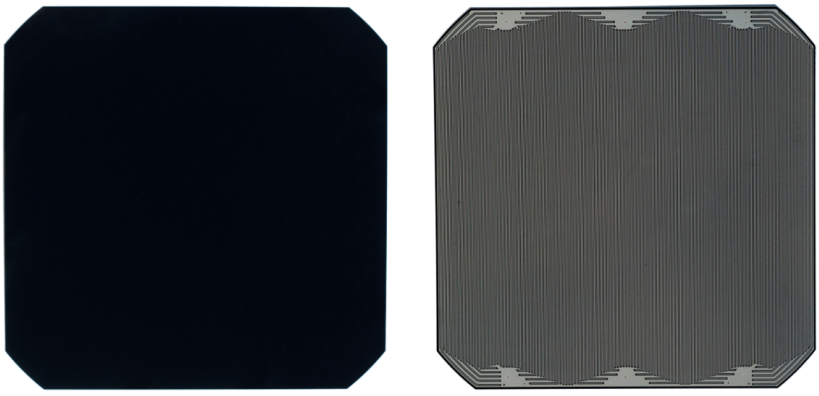

Figure 2.14: Front and Back side of the IBC solar cell [39]

Biosphere Solar's PV module version - 0.4, depicted in Figure 1.10a, incorporates interdigitated back contact (IBC) solar cells. This choice is attributed to Biosphere Solar's recognition of the trade-off between disassembly convenience and performance, with IBC cells offering favorable performance characteristics. In terms of interconnections, manual soldering of these cells is considerably simpler due to the presence of only 6 contact points on the back for creating solder joints.

These solar cells are interconnected using a dog-bone interconnection wire. The dog-bone wire (as shown in figure 2.15a) has six contact regions that can be soldered to two IBC solar cells, connecting the positively charged side of the back side of one IBC cell to the negatively charged side of the back side of another IBC cell to create a series connection (as shown in Figure 2.15b).

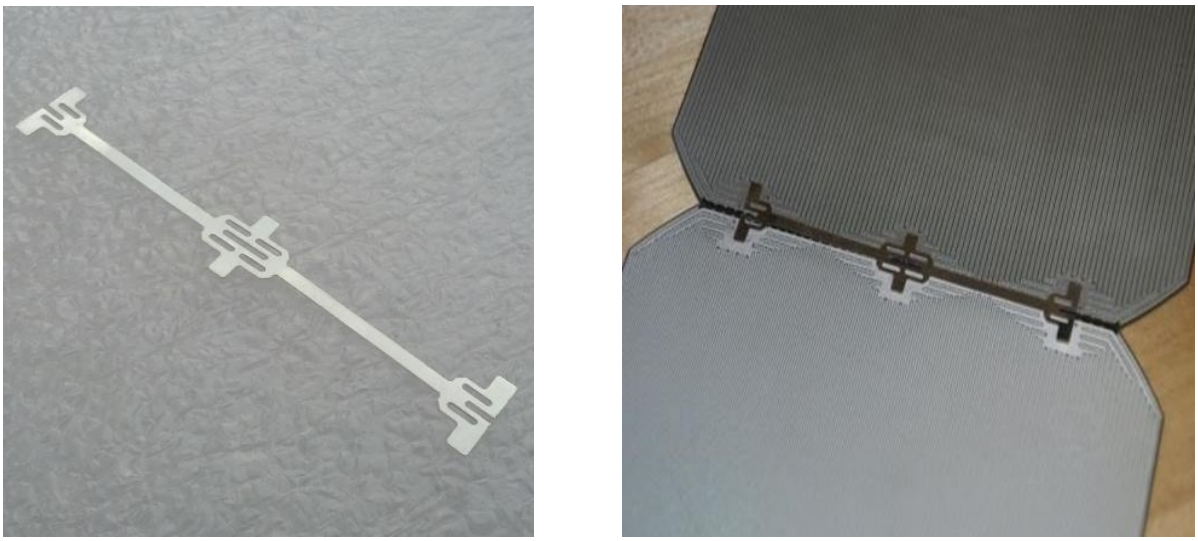

(a) (b)

Figure 2.15: (a) Dog-bone wire, and (b) IBC solar cells interconnected with dog-bone wire [40]

CHAPTER 3

Concepts

This chapter explains the concepts explored for creating disconnectable interconnection mechanisms. It discusses desolderable interconnections, using single dog-bone, and using two dog-bones. Next, it describes the slider-based interconnection mechanism in the pre-designed cell-bed, along with its visible drawbacks. Lastly, it concludes by explaining contact pressure based interconnections that rely on magnetic force.

3.1 Desolderable Interconnections

3.1.1 Assessing the Desoldering Capability of Single Dog-Bone Interconnections

The interconnection process for connecting two IBC solar cells in series using the dog-bone involves soldering six contact regions that connect the dog-bone to the two solar cells (as shown in Figure 3.1).

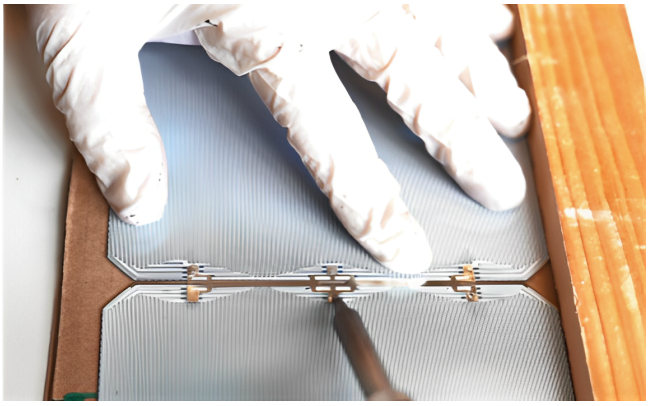

Figure 3.1: Soldering process to connect two IBC solar cells using the dog-bone [41]

Initially, the soldering process was based on using the standard SnAgCu (Sn96.5Ag3.0Cu0.5) alloy which has a melting point of 220°C [42]. To allow quick and efficient soldering, the soldering gun temperature was set to 340°C during the soldering process.

To solder the dog-bone to the solar cell, the following steps were taken:

1. Solder flux was applied to the contact points on the backside of the IBC solar cells.
2. The SnAgCu solder wire was melted using the soldering iron to create solder joints on the contact points. The heat from the melted solder vaporized the solder flux, effectively removing oxides and contaminants from the soldering surfaces.
3. A dog-bone was positioned such that the contact regions were above the solder joints, and then heat was applied to these contact regions of the dog-bone. This melted the solder joints, facilitating the creation of a strong and reliable connection between the dog-bone and the solar cell.

The contact regions of the dog-bone are not in direct contact with the c-Si top layer, which shows potential for safe desoldering without damaging the adjacent solar cell.

Initially, a test was conducted to assess the possibility of desoldering by solely applying heat through the placement of a soldering iron on the contact regions of the dog-bone soldered to the solar cell (as depicted in Figure 3.1). This test aimed to determine if the dog-bone contact region could be disconnected by melting the solder joints using heat.

During this process, it was noticed that due to the high melting point of the alloy and the positioning of the dog-bone on top of the solder joints, it was necessary to increase the soldering iron temperature from 340°C to 380°C to melt the solder joints again. However, this resulted in not only melting the solder joints but also the tin coating on the dog-bone since tin has a melting point of 231.92°C [43]. As a result, this melting of the tin coating created molten joints, which were connecting the contact regions of the dog-bone to the solar cell, requiring the application of horizontal physical force on the solar cells to separate the dog-bone from the solar cell.

Applying horizontal physical force directly to the solar cells to separate the dog-bone was not an optimal method due to the risk of causing cracks and damaging the cells. Therefore, an alternative approach was employed. This approach involved delicately using a needle-file (depicted in Figure 3.2a) to touch the underside of the dog-bone while simultaneously applying heat using the soldering iron to the adjacent contact area of the dog-bone (as shown in Figure 3.2b). After applying heat, the soldering iron was removed to allow the contact region of the dog-bone to get disconnected due to the vertical physical force applied by the needle file and separate from the solder joint.
The underlying principle of this technique was to apply controlled force on the dog-bone to push the contact region upwards while simultaneously melting and deforming the solder joint below the contact region, which can lead to the separation of dog-bone from the solar cell.

The experimental setup for desoldering is shown in Figure 3.2b . In this setup, two wooden planks were strategically positioned to create a gap, allowing the needle-file to access the underside of the dog-bone.

(a) **(b)**

Figure 3.2: (a) Needle-file used for applying force on dog-bone, and (b) Desoldering process

In five repetitions of the experiment, four instances resulted in cracking at the edges of either one of the cells. These cracks were caused by the physical force applied on the dog-bone tending to lift up the edge of the adjacent solar cell due to the contact region still being connected to the solar cell because of the molten tin coating. To tackle this issue, additional research was undertaken to explore solder alloys with lower melting temperatures, aiming to prevent the melting of the tin coating on the dog-bones during the desoldering process. The objective was to investigate whether using such solder alloys for soldering could reduce the physical force required to separate the dog-bone from the solar cell during desoldering.
A literature study was conducted to determine which alloys are suitable for testing. The factors taken into consideration for identifying a suitable solder alloy were as follows:

1. The alloy must be devoid of lead (Pb) for the reasons mentioned in Section 1.3 and silver (Ag) for it's rarity and cost.
2. The alloy's price must not be higher than the price of standard silver-based alloys.
3. The alloy should be easily accessible in the market.

The technical parameters considered for solder alloy selection were as follows:

1. The melting temperature of the alloy must be less than that of the SnAgCu solder alloy (220°C).
2. The alloy should be compatible for soldering using industrial methods such as Infra-Red soldering and Reflow ovens.

3.1.2 Choosing Suitable Solder Alloy

An eutectic mixture is a homogeneous blend with a melting point lower than the individual melting points of its elements. The eutectic temperature represents the lowest attainable melting point across all possible mixing ratios of the constituent ingredients. [44]

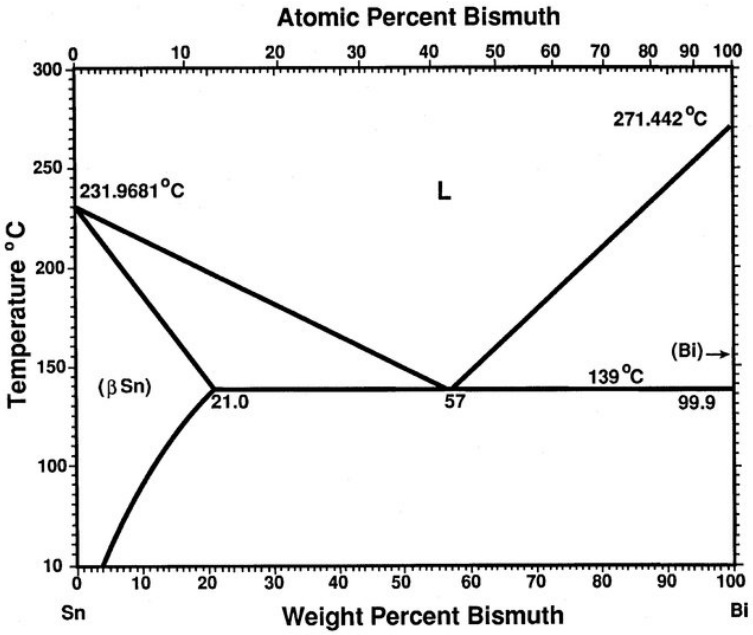

Figure 3.3: Binary phase diagram of SnBi alloy [45]

Figure 3.3 illustrates the binary phase diagram of the SnBi (Sn42Bi58) solder alloy, revealing its eutectic point at 139°C. Notably, this eutectic point is lower than those of SnPb (189°C) and SnAgCu (220°C). [46]

The suitability of the SnBi solder alloy for desolderable interconnections was assessed due to its lower melting point compared to the SnAgCu solder alloy. Furthermore, its application in the SWCT interconnection as an alternative to the SnIn solder alloy demonstrates the potential for using this solder alloy for solar cell interconnections (see 2.6).

While the eutectic point of the SnIn alloy (118°C) is even lower than that of the SnBi alloy [47], its potential as an alternative solder alloy is not feasible due to its rarity, toxicity, and high cost. These factors led to its exclusion from testing.

Another solder alloy that was considered is Sn99.3Cu0.7. This alloy offers an advantage in terms of material abundance compared to SnAgCu. Comprising mainly of tin (Sn) and copper (Cu), both widely available and easily sourced, it holds potential. However, its melting point of 227°C [48] exceeds that of SnAgCu (220°C), rendering it unsuitable for testing.

3.1.3 Analyzing Thermal Expansion Coefficients in Various Solder Alloys

Thermal expansion refers to the volume increase of a material as its temperature rises. Solids exhibit a linear expansion coefficient. [49].

The relationship between thermal expansion and temperature, substance, and original length is summarized by the equation [50] :

$$dL/dT = \alpha \cdot L \tag{3.1}$$

Here, dL represents the change in length, L represents the initial length of the material and dT represents the change in temperature. The coefficient of linear thermal expansion (α or CTE) is a material-specific property that varies with temperature [50].
Since α is nearly constant and very small, for practical purposes, the following linear approximation can be used [50] :

$$dL = \alpha \cdot L \cdot dT \tag{3.2}$$

The mismatch in thermal expansion coefficients can give rise to detrimental effects on solder joints added on solar cells. Solar cell structures often comprise dissimilar materials, such as semiconductor materials and metal interconnects, each possessing unique thermal expansion coefficients. Consequently, when subjected to temperature fluctuations, these materials undergo differential expansion and contraction rates. [28]

Table 3.1: Thermal expansion coefficient mismatch corresponding to various solder alloys

Material and role	CTE (e-6·m/K)	CTE Mismatch
Sn: coating on back side of IBC solar cell	23.4 [28]	-
Sn42Bi58: low melting point solder alloy	16.7 [51]	6.7
Sn96.5Ag3.0Cu0.5: standard solder alloy	23.5 [52]	0.1
Sn99.3Cu0.7: abundant material solder alloy	21 [53]	2.4

Table 3.1 provides a comparative analysis of the thermal expansion coefficients of Sn (back coating on IBC solar cell according to the datasheet [54]) and various solder alloys, including , Sn42Bi58, Sn96AgCu, and Sn99.7Cu0.3. The table also presents the thermal expansion coefficient mismatch between each solder alloy and the Sn back coating. The mismatch is calculated by subtracting the thermal expansion coefficient of the solder alloy from the thermal expansion coefficient of Sn for each alloy.

Based on the data presented, it is evident that Sn42Bi58 exhibits the highest thermal expansion coefficient mismatch when compared to the other three solder alloys. This discrepancy suggests that Sn42Bi58 is more prone to experiencing damage in solder joints when the solar cells are exposed to temperature variations. Furthermore, Sn99.4Cu0.7 exhibits the second highest mismatch, while Sn96AgCu demonstrates the lowest mismatch among the investigated solder alloys.

Evaluating The Wettability of Sn42Bi58

Wetting is a crucial process in soldering, involving the interaction between liquid solder and solid surface components. This interaction, also known as spreading, ensures a proper metallic bond between metals.

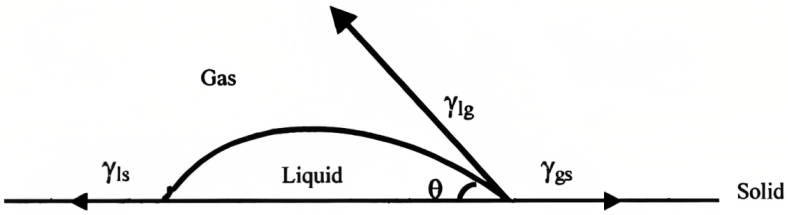

Figure 3.4: Wetting angle θ[55]

The degree of wetting is determined by the contact angle (θ) formed at the interface of the solid and liquid in a specific environment, as depicted in Figure 3.4. Generally, if the contact angle falls between 0° and 90°, the system is considered to exhibit wetting behavior. On the other hand, if the contact angle ranges between 90° and 180°, the system is considered non-wetting [55].

The wettability of Sn42Bi58 solder alloy is lower compared to other solder alloys due to the presence of bismuth (Bi), which is known for its brittle nature. Bismuth has a tendency to form oxide layers on its surface, hindering the proper wetting of the solder alloy on solid surfaces. The brittle nature of bismuth can also lead to poor adhesion and weak bonding between the solder and the substrate. Consequently, Sn42Bi58 solder alloy may exhibit reduced wetting behavior, affecting its ability to form a robust metallurgical bond during soldering processes [56]. Figure 3.5a depicts the temporal variation of contact angles for molten SnBiCu solder alloy on a Cu substrate at different temperatures. The diagram reveals that at higher temperatures and with increased soldering time, the wetting angle decreases.

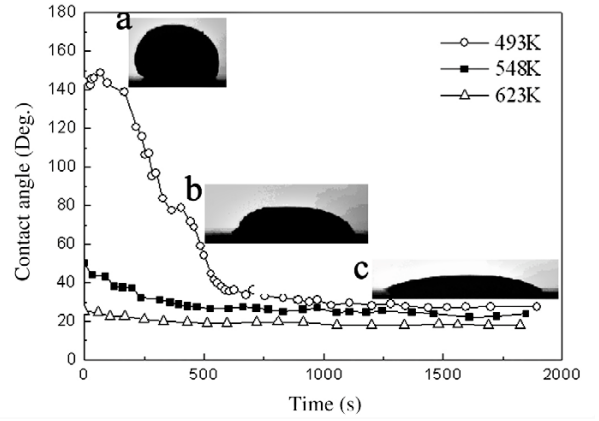

(a)

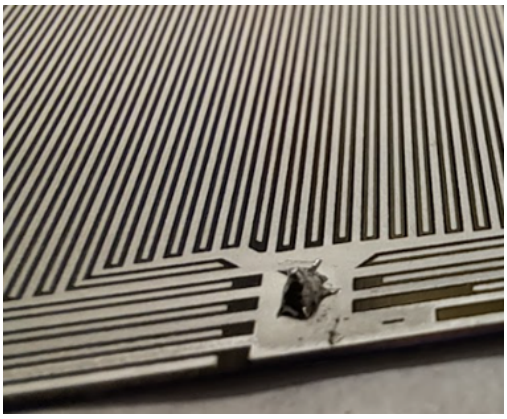

(b)

Figure 3.5: (a) Variation in contact angles over time for molten Sn-Bi-Cu on Cu substrate at different temperatures [56], and (b) Solder joint created with SnBi alloy on IBC solar cell's backside at a soldering temperature of 180°C

Figure 3.5b shows the SnBi solder joint formed on the back side of an IBC solar cell during testing to determine the minimum required soldering iron temperature. In this specific instance, the soldering iron temperature was set to 180°C. It was observed that these joints would fracture when a certain level of force was applied to the dog-bone by the soldering tip. After multiple attempts, it was noted that adjusting the soldering gun temperature to 240°C resulted in a reduced wetting angle for the joint.

This adjustment prevented the joint from breaking under the physical stress created by the soldering tip when placed on the dog-bone.

Assessing Bismuth's Availaility and Supply chain

Understanding the availability of bismuth and its supply chain is crucial for the SnBi alloy if used in Biosphere Solar's PV modules.

Bismuth is obtained as a by-product during mining operations involving lead, tungsten, copper, or gold. However, its recovery is often overlooked when it is found alongside more abundant metals. While certain mines prioritize bismuth as their primary product, the majority of global bismuth production comes from the by-products of lead and tungsten extraction [57].

Figure 3.6 illustrates that Asia is the dominant region for global Bi production, as indicated by annual production statistics. Historically, China has been the largest producer, obtaining Bi as a by-product of both lead (Pb) and tungsten (W) processing. Artisanal mining for Bi is also practiced in China, where manual separation of mineralization rich in Bi contributes significantly to the worldwide production of concentrates [57].

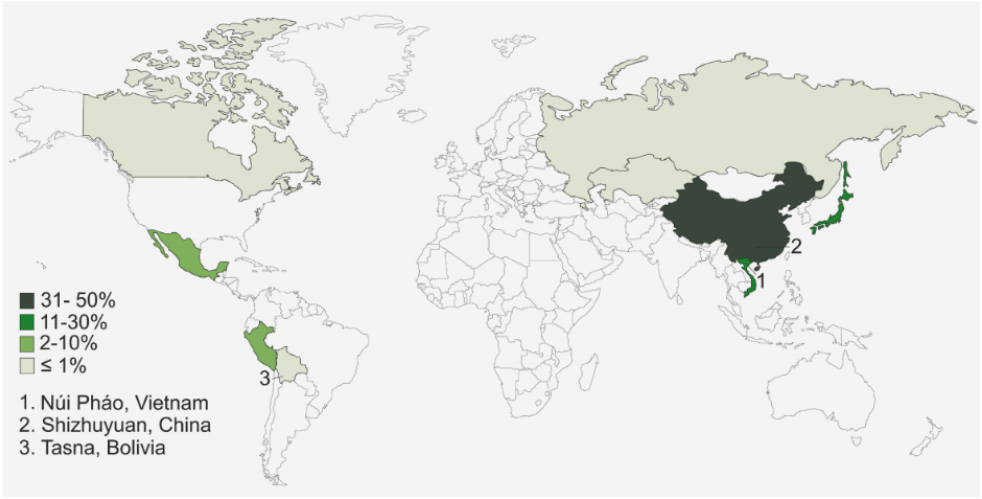

Figure 3.6: The market share distribution of global Bi production in 2019 [57]

Bismuth subcarbonate and bismuth alloys are used in pharmaceuticals, cosmetics, and metallurgy as non-toxic substitutes for lead. They are used in water pipes, ammunition, solder alloys, fishing equipment, paints, and lead-free glass for plasma TVs and displays [57].

The demand for Bi is expected to grow by 4-5%, driven by pharmaceutical applications and the substitution of lead. However, the recovery rate of Bi from end-of-life products is less than 1%, posing challenges for recycling. Solder alloys, particularly in electronic equipment, offer potential for Bi recycling. Hydrometallurgical methods have been explored for recovering Bi from copper smelter converter dust, achieving high recovery rates and commercially viable Bi_2O_3 production [57].

Bismuth is categorized as a critical rare earth material. Its supply security is not mainly determined by its geological availability. Instead, its importance in valuable end-use applications and market concentration play a significant role in its critical status. However, supply bottlenecks arise due to production concentration in only a few countries and industrial inertia, which tends to overlook the value of bismuth as a by-product [57].

Bismuth Availability for Solar Cell Soldering in PV Modules

The amount of bismuth consumed also depends on the type of interconnection and the number of busbars. Bismuth consumption must not exceed 3.5 mg per Watt in order to establish a multi-TW market (e.g., 3 TW of annual PV production) with 50% of world bismuth supply devoted to the PV sector. In a more realistic scenario, with just 20-25% of bismuth supply used in PV, intake should be limited to 1.4 - 1.75 mg per Watt. Figure 3.7 depicts the relationship between bismuth consumption per cell in mg per Watt, wire diameter, and wire count, assuming each wire is coated with a 3 μm thick layer of SnBi (58% Bi in weight). With 300 μm diameter wires, consumption can only be reduced below 1.4 mg per Watt by using 2-3 wires per side, which differs from the current standard of 24 wires for SmartWire and 12 ribbons for the MBB (multi busbar) approach [58].

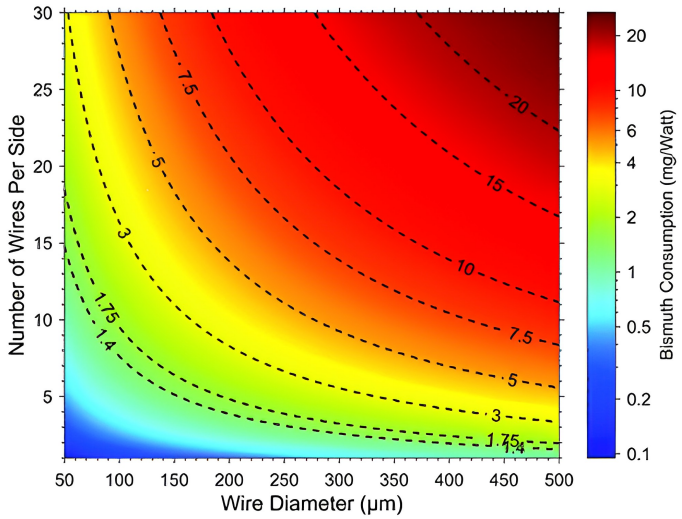

Figure 3.7: Bismuth consumption per cell in mg per Watt, wire diameter, and wire count [58]

The advantage of utilizing IBC cells is that there are only three tiny regions for solder joints to be applied. A calibrated weighing scale with a tolerance of 2% was utilized to determine how much Bi is used in the solder joints of these cells (in mg per Watt). According to the solar cell datasheet [54], the cell weighs approximately 6.5 g and has a rated power of 3.45 W. When measured using the weighing scale, the weight of the cell without any solder joints is 6.455 g (as seen in Figure 3.8a).

(a) **(b)**

Figure 3.8: (a) Base weight of IBC solar cell, and (b) Weight of IBC solar cell with solder joints

After obtaining the initial weight of the cell, solder joints were added to the six contact sites, and the cell was weighed again, resulting in a weight of 6.46 g (as seen in Figure 3.8b). To determine the amount of bismuth consumed, the weight difference between the measurement with solder joints and the measurement without solder joints was calculated to be 6.460 g - 6.455 g = 0.005 g. This weight difference was then multiplied by 0.58, which corresponds to the bismuth composition in the SnBi solder alloy (Sn42Bi58). The resulting weight of bismuth which is 0.0029 g, converted to mg/W (considering the rated power of 3.45 W), resulted in 0.84 mg/W. To address the variability in solder joint size caused by manual soldering, the average of three additional measurements was taken for calculating the mg/W consumption. This approach resulted in an average value of 1.06 mg/W, which is lower than the target weight of 1.4 mg/W for busbar-based interconnection topologies. However, it is important to understand that limited data is available on the availability of bismuth (Bi) resources and reserves since it is not typically included in calculations unless found in significant amounts. The US Geological Survey (USGS) does not provide specific Bi reserve figures due to insufficient quantitative data. Global Bi reserve estimates are generally based on the Bi content of lead (Pb) resources, as Bi production is commonly associated with the processing of Pb ores as a by-product [59]. The calculated target milligrams per Watt for a multi-terawatt scenario takes into account the estimated global reserve of bismuth, which amounts to 320,000 tonnes. This estimation is based on the data provided in the 2015 Mineral Commodities Summaries report published by USGS [60].

To summarize, the literature supports the investigation of the SnBi solder alloy as a potential solution for addressing cell breakage and microcrack formation in IBC solar cells during desoldering, despite the challenges related to thermal expansion coefficient mismatch and lower wettability. Furthermore, the evaluation of bismuth consumption in IBC solar cells demonstrates that the consumption can be significantly reduced to meet the desired weight targets for various interconnection topologies, ranging from 0.84 to 1.06 mg per Watt. However, due to limited data on bismuth availability, further research and testing are needed to comprehensively assess the feasibility and long-term benefits of implementing bismuth-based solder alloys, especially within the context of Circular PV manufacturing. Nevertheless, the availability of the solder alloy in the market is noteworthy, particularly due to its silver and lead-free composition

3.2 Creating an Overlapping Connection through Soldering by Joining Two Dog-Bones.

This interconnection mechanism involves the series connection of a pair of IBC solar cells using two dog-bones, as illustrated in Figure 3.9. In this interconnection, the left-sided solar cell is soldered to the first dog-bone (light grey), while the second dog-bone (dark grey) is soldered to the right-sided solar cell. Subsequently, the dog-bones are soldered together at the contact regions that are not connected to the solar cells. This configuration enables the flow of current from the positive side of the left cell to the negative side of the right cell, establishing a series connection between the two solar cells.

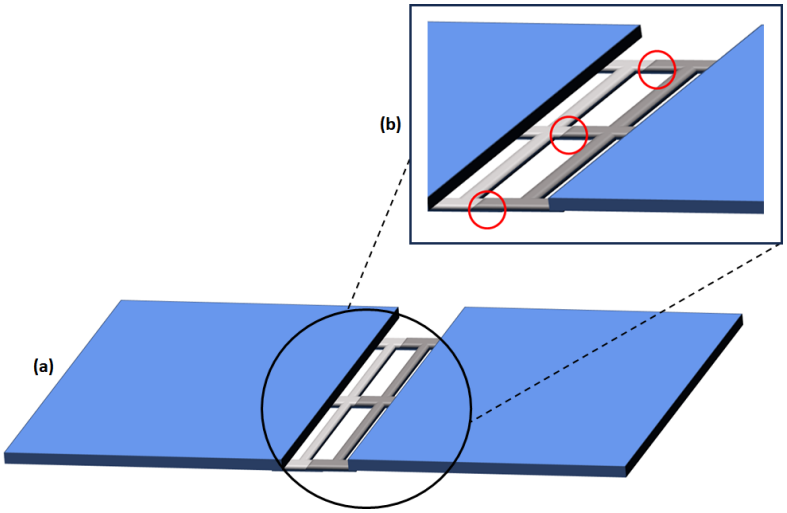

Figure 3.9: (a) Schematic representation of the interconnection based on soldering two dog-bones and creating an overlapping connection , and (b) Zoomed in image indicating the overlapping regions (highlighted in red)

Figure 3.9 (a) depicts the schematic representation of the interconnection mechanism. In this figure, the right-side dog-bone, which overlaps the left-side dog-bone from the top, is intentionally shaded in dark grey, while the left-side dog-bone is shaded in light grey. This shading distinction helps visually understand that there are two dog-bones in this interconnection with overlapping contact regions. Figure 3.9 (b) provides a zoomed-in view of the interconnection, with the overlapping contact regions highlighted in red circles. To create the solder joints, heat is applied to the upper overlapping contact regions (dark grey) using a soldering iron, causing the tin coating to melt onto the lower contact regions (light grey). As a result, the molten coating forms a solder joint, establishing a conductive connection between the components. Note that while creating this connection, no additional solder is used.

To disconnect the interconnection, the left-sided dog-bone can be pressed down while simultaneously applying heat on the overlapping contact regions. This will cause the previously melted tin coating to liquefy once more, facilitating the disconnection of the connected regions.

The investigation of this concept was motivated by the development of the DIY kit by Biosphere Solar. The DIY kit, as described in section 1.5, targets enthusiasts and individuals interested in creating their own miniature PV modules for charging small electronic devices like cell phones. Soldering and desoldering a single dog-bone for interconnection poses challenges due to the risk of damaging the cells, particularly for inexperienced individuals who may struggle with handling the cells without causing breakage. However, by pre-soldering the cells with dog-bones and incorporating them into the DIY kit, the maker only needs to solder and desolder the contact regions connecting the two dog-bones. This approach reduces the physical contact with the solar cells, thereby minimizing the likelihood of cell cracking.

3.3 Interconnections Based on Contact Pressure

Contact pressure-based interconnections, unlike soldered interconnections, use mechanical force to establish and sustain electrical connections, reducing dismantling time and enhancing the disassembly and reconfiguration.

Figure 3.10 shows examples of electrical connections based on contact pressure.

(a) (b) (c)

Figure 3.10: (a) Screw terminal block with connected wires [61], (b) Panel mounted connector [62], and (c) Plastic clamp based connection [63]

As discussed in Subsection 2.3.2, interconnections relying on contact pressure may experience electrical contact resistance caused by non-uniform contact areas, which can limit the flow of current. Nevertheless, these interconnection mechanisms hold promise for convenient disassembly and can be used to connect solar cells in series.

3.3.1 Utilizing the Cell-Bed for Contact Pressure Based Interconnections

As mentioned in section 1.5, Biosphere Solar is currently working on developing PV modules without EVA encapsulation. Before the thesis started, the product developers at Biosphere Solar designed a polymer based cell-bed, which can be seen in Figure 3.11. The purpose of this cell-bed is to securely hold the solar cells in position, compensating for the absence of EVA and ensuring that the solar cells do not collide with each other.

Figure 3.11: Prototype with cell-beds

Another version of the cell-bed was designed with an additional feature to enable modular interconnections. This interconnection mechanism involves using two dog-bone wires to establish connections between the positive terminal of one solar cell and the negative terminal of another. The incorporation of sliding lockers (as depicted in Figure 3.12) creates contact pressure on the right and left overlapping contact regions of the dog-bones. This ensures a consistent electrical contact for the modular interconnection. The interconnection can be disassembled simply by removing the sliders.

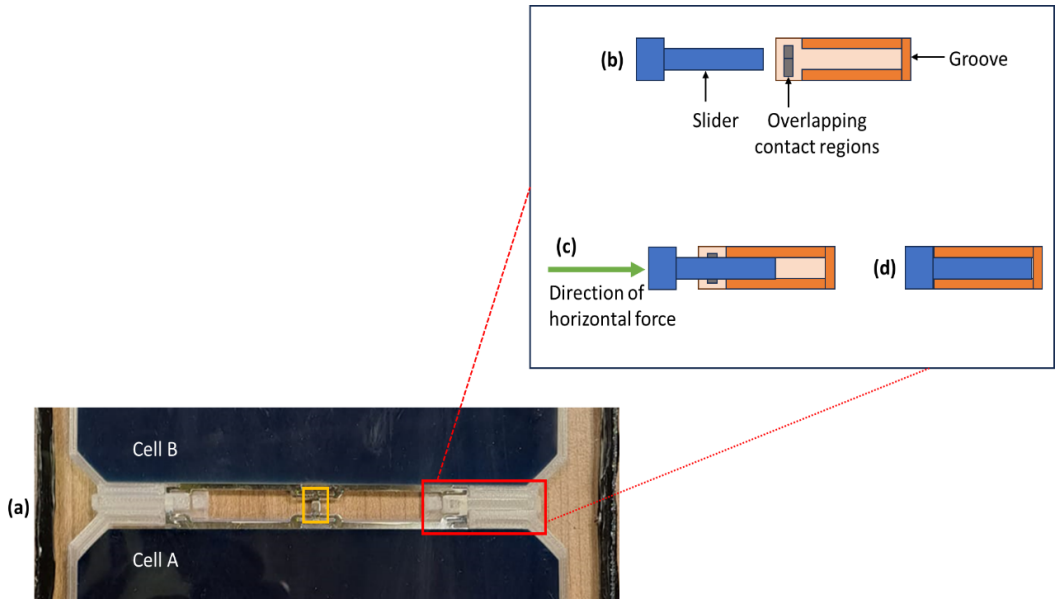

Figure 3.12: (a) Solar cells A and B connected in series using the slider based interconnection mechanism (highlighted in red outline) in the cell-bed, (b) Schematic illustration of the slider, overlapping contact regions of the dog-bones and the groove, (c) Schematic representation of how the slider is inserted using horizontal force, and (d) Schematic illustration of the slider completely inserted in the groove

The assembly procedure of the interconnection mechanism illustrated in Figure 3.12 is as follows:

1. Solder the positive polarity side of Cell A to a dog-bone.
2. Solder the negative polarity side of Cell B to another dog-bone.
3. Position both Cell A and Cell B in the cell-bed, aligning the non-soldered contact regions of the dog-bones in a way that the non-soldered contact regions overlap, as shown in the yellow-highlighted part in Figure 3.12(a).
4. Press down the overlapped contact regions beneath the sliders (highlighted in red in Figure 3.12), and insert the sliders horizontally on top of these regions.
5. Then, press the sliders horizontally into the designated grooves to secure them in place.

An integral aspect of the thesis involved the examination of the cell-bed with slider-based interconnection and the implementation of enhancements in the cell-bed design aimed at improving the interconnection mechanism. Figure 3.12(a) reveals two noticeable limitations in the slider-based interconnection design:

1. There is no contact pressure in the middle section of the two dog-bone configuration (highlighted in yellow in Figure 3.12)(a).
2. The distance between the cells is increased, which can lead to a higher series resistance. This increased resistance is attributed to the longer path the electrons need to traverse, as series resistance is directly proportional to the length of the path.

The work on optimizing the cell-bed design for improving the electrical performance is further discussed in Section 5.3.

3.3.2 Choosing the Optimal Material for the Cell-Bed

Gaining an understanding of the cell-bed material is crucial as it directly impacts the performance of interconnections since the application of contact pressure is done using components made from the same material.

Prior to commencing the thesis, the product designers working at Biosphere solar utilized two amorphous thermoplastic polymers, namely PLA (Polylactic acid) and PETG (Polyethylene terephthalate glycol), for printing the cell-bed.
Thermoplastics are materials that soften (melt) reversibly when heated and harden when cooled [64]. Since the molecular chains have a finite amount of energy to move, thermoplastics are typically solid at room temperature. The molecular chains can, however, absorb energy and move more when heated, causing the plastic to expand and change into a viscous melt that can be molded into various shapes. The energy is released as the plastic cools, and the distance between the molecular chains closes, causing the plastic to solidify and hold its new shape [64].

It is crucial to understand how these polymers behave when subjected to temperature variations. The glass transition temperature (Tg) is the temperature at which amorphous portions in a material transform from rigid to flexible, increasing free volume. Tg is determined by the substance's molecular structure, with flexible backbones in plastics having lower Tg, while rigid, inflexible materials exhibit higher Tg [64]. The melting point (Tm) is the critical temperature at which the crystalline sections of a semicrystalline plastic become flowable. In the "rubbery area" between Tg and Tm, the material can stretch significantly under low load. The melting and softening behavior of semicrystalline and amorphous materials is illustrated in Figure 3.13. This Figure also demonstrates that semicrystalline materials maintain their mechanical properties up to Tm, whereas amorphous materials experience a loss of strength beyond Tg [64].

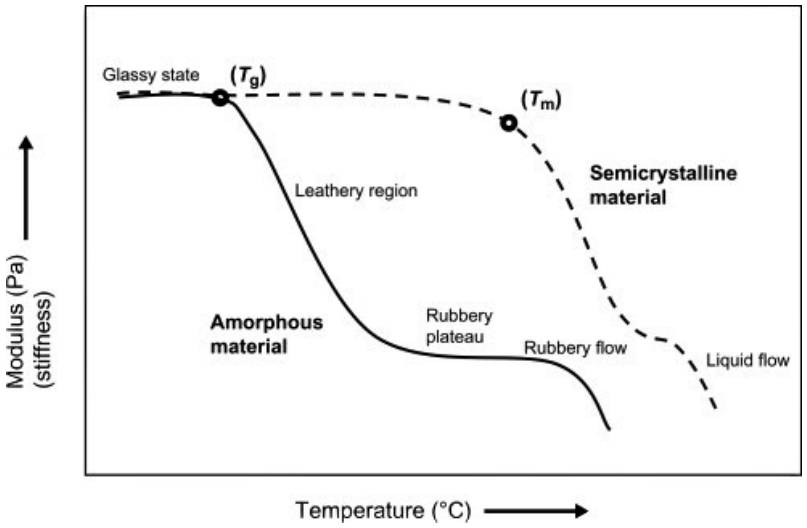

Figure 3.13: Material behavior of amorphous and semi-crystalline polymers with respect to temperature [64]

PETG has a glass transition temperature (Tg) of 80°C [65], while PLA has a Tg of 55°C [66].
Understanding the PV module temperatures during operation and thermal tests required for certification is crucial because if the temperature surpasses the glass transition temperature, the cell-bed can deform and potentially affect the interconnection mechanism. It is also important to understand the impact of ambient temperature on the temperature of a PV module. Figure 3.14 displays a graph illustrating the relationship between PV module temperatures, irradiance levels, and ambient temperature. The graph clearly demonstrates a direct proportionality between PV module temperature and ambient temperature.

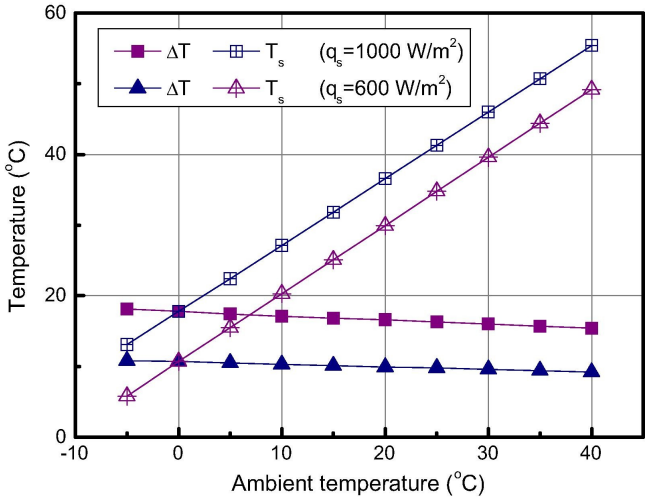

Figure 3.14: PV module temperature with respect to ambient temperature [67]

Considering the temperatures of PV module under specific irradiance levels seen above, it was clear that PLA (Tg = 55°C) is not a suitable material for the cell-bed and PETG (Tg = 80°C) may not be suitable for extreme conditions with high irradiance and high ambient temperature, and under thermal cycle tests where the temperatures can reach up to 85°C [68].

To prevent the cell-bed from deforming and affecting the interconnections, alternative polymers were studied.
Acrylonitrile butadiene styrene (ABS) is a plastic made from a glassy matrix and a combination of styrene-acrylonitrile copolymer and butadiene styrene copolymer. This combination provides optimal properties, including toughness, excellent thermal resistance, and superior characteristics compared to polystyrene plastics. ABS finds extensive application in various fields, including automotive components, household appliances, furniture parts, and toys [69]. The glass transition temperature (Tg) of ABS is around 105°C [70].
Another polymer that was studied was Polycarbonate (PC). Polycarbonates are biocompatible and impact-resistant polymers that are utilized in DVD making and other fields for thermal stability and biodegradability. They are often mixed with other polymers. Polycarbonate has a glass transition temperature of roughly 150°C [71].

In order to decide which polymer to use for printing the cell-beds, the following comparison was made based on market survey and discussions with the product designers at Biosphere Solar:

Table 3.2: Comparison of ABS and Polycarbonate

Filament Material	Cost Difference	Ease of Printing	Material Rigidity
ABS	Cheaper than Polycarbonate. Expensive than PLA and PETG.	Fffers strong layer adhesion, ease of printing, and strong print quality, but has tendency to warp and requires enclosed environment.	Offers strength and flexibility, and impact resistance.
Polycarbonate	Expensive than ABS, PLA and PETG.	Warping-resistant. printing is more challenging and requires air-tight enclosure for proper adhesion.	Excels in rigidity, impact resistance, durability, producing stiffer parts with less flexibility.

In summary, ABS is cost-effective and easier to print with, offering a balance of strength and flexibility. Polycarbonate excels in rigidity and impact resistance, making it suitable for applications that require high durability. After analyzing the comparison mentioned above and availability of the filament in market, it was decided to print the improved cell-beds using ABS filament. For 3D printing ABS, an enclosure with sufficient ventilation needs to be built around the 3D printer to maintain the melting temperature and preventing the toxic fumes released while printing this material from leaking.

An enclosure was made out of plexiglass, wood, and an electric ventilation fan attached to tubes that led the sucked-in air outside of the workspace. Figure 3.15 shows the Prusa-mini 3D printer printing a cell-bed with ABS filament.

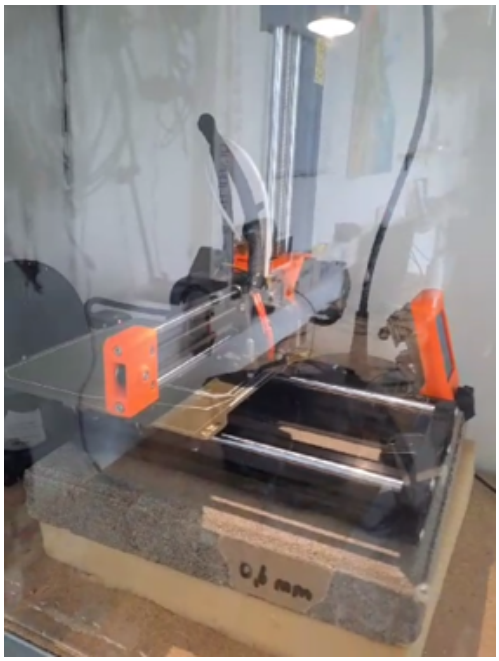

Figure 3.15: Printing improved cell-bed version 2 with ABS filament

In this thesis, 3D printing was exclusively utilized for prototyping purposes. However, for large-scale industrialization, Biosphere Solar intends to employ injection molding for manufacturing the cell-beds.

3.4 Contacts Utilizing Magnetic Pressure.

The core principle of this interconnection relies on employing magnetic force to apply pressure on the overlapping contact areas between two dog-bones, as opposed to using other locking methods such as sliders. Magnets are preferred in this design because they possess a stronger and more consistent force due to their magnetic attraction, ensuring a stable and uniform connection between the overlapping contact regions. Additionally, the convenience of easy disassembly can be achieved as magnets can be separated effortlessly by applying horizontal force.

Figure 3.16 introduces the concept of using magnets to exert contact pressure on the overlapping contact regions of two dog-bones connecting two solar cells in series.

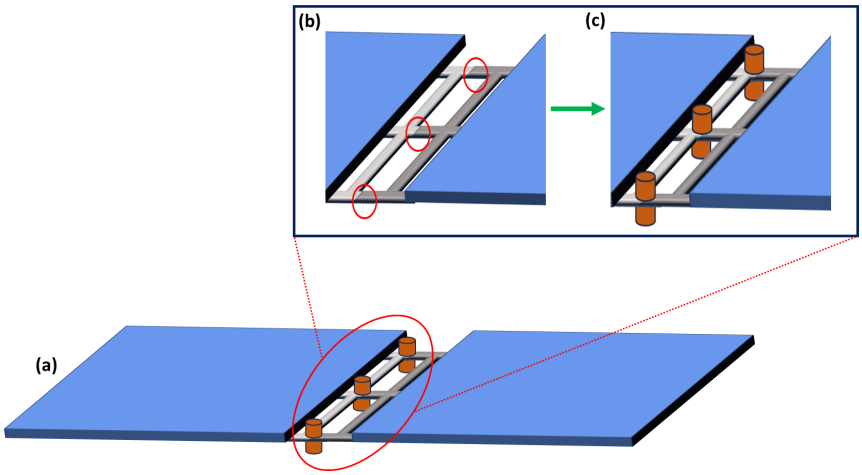

Figure 3.16: (a) Schematic representation of two solar cells connected in series using the magnetic-force based interconnection mechanism (highlighted in red circle), (b) Schematic illustration of two dog-bones soldered to the opposite polarities of two solar cells and placed such that the non-soldered contact regions (highlighted in red) of the dog-bones overlap, and (c) Schematic representation of the magnets placed on top and bottom of the overlapping contact regions to create contact pressure

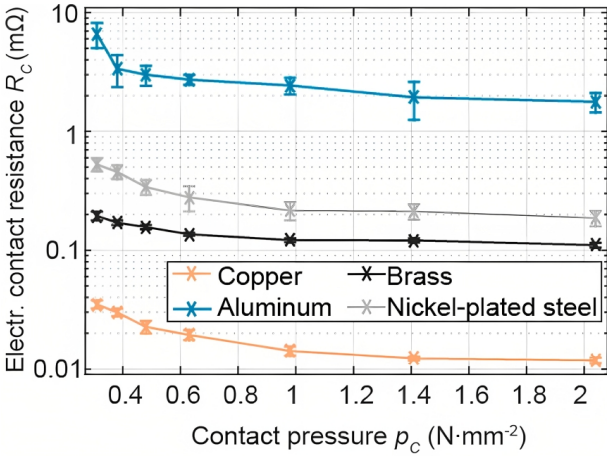

Figure 3.17: Electrical contact resistance vs contact pressure [72]

Figure 3.17 illustrates a graph that compares the electrical contact resistance of different metals against the applied contact pressure, which is achieved using pneumatic force.

The graph clearly demonstrates that as the contact pressure increases, the electrical resistance decreases. Another advantage of utilizing magnets is their flat surface, which can help create an evenly distributed force on the contact regions.

3.4.1 Selecting Suitable Type of Magnet

When choosing a suitable magnet for testing this interconnection, following factors were considered:

1. Magnetic strength: The chosen magnet should possess a high magnetic field strength and must be a permanent magnet.
2. Commercial availability: prioritizing magnets that can be obtained locally, ensuring ease of procurement.
3. Size: It is necessary for the magnet to be available in compact dimensions to match the requirements of the interconnection being tested.

Neodymium (NdFeB) magnets are widely recognized for their higher magnetic field strength compared to Alnico and Ferrite magnets. This characteristic is attributed to the distinctive properties of neodymium and iron, the fundamental components of neodymium magnets.

Typically, neodymium magnets have magnetic field strengths ranging from approximately 1 to 1.4 tesla (T) [73]. In contrast, Alnico magnets (aluminium, nickel and cobalt alloy with iron) have a magnetic field strength of 0.15 T [74], and Ferrite magnets have a maximum magnetic field strength of 0.35 T [75].

3.4.2 Assessing The Availability and Recyclability of Neodymium Magnets

Neodymium magnets (NdFeB) are permanent magnets which are commercially accessible and renowned for their small dimensions. Neodymium (Nd) is a rare earth element (REE), which is classified as one of the lanthanides (f-block elements in the periodic table) found in the Earth's crust, with limited economically viable deposits. REEs find significant usage in advanced technologies such as electronics, transportation, energy, and defense. China has emerged as the predominant supplier of REEs since the early 1990s, accounting for 70% of the world's supply. However, the mining and processing of rare earths in China have resulted in significant environmental pollution [26].

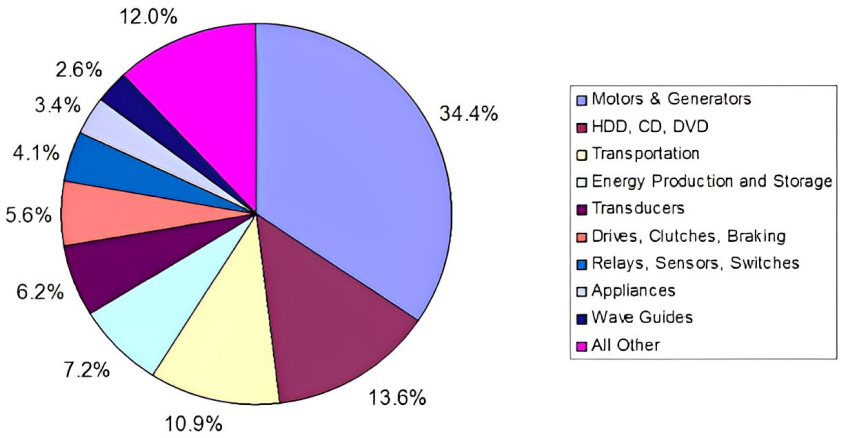

Figure 3.18: Distribution of NdFeB market shares across different applications globally in 2012 [26]

Figure 3.18 illustrates the distribution of market shares for NdFeB across various applications worldwide in 2012, with motors and generators exhibiting the largest share.

In 1983, researchers discovered that combining neodymium with iron and boron led to the development of highly potent permanent magnets, facilitating the miniaturization of electronics, including applications in loudspeakers, computer hard drives, mobile phones, and electronic components for automobiles. The largest demand for high-performance neodymium-iron-boron magnets is in electric and hybrid vehicle motors. Neodymium magnets are also utilized in wind turbines, aerospace, and space technologies [26].
NdFeB magnets are produced by melting a combination of neodymium, iron, and boron, followed by casting the molten mixture into ingots. The ingots are then crushed into powder form, which is

subsequently subjected to sintering and magnetization processes to create the permanent magnet. An alternative technique involves adding boron in a controlled manner to the neodymium iron master alloy, offering a different approach to manufacturing these magnets [76].

Technologies for recycling neodymium and rare earth elements (REEs) from electronic waste, including electric motors, face limited infrastructure and high costs. Despite efforts by companies and researchers, shredded e-waste results in the loss of REEs in dust and ferrous fractions. The economic viability of recycling these materials remains challenging due to the small percentage in electronic waste [77].

After consulting with an assistant professor from the Materials Science and Engineering department at TU Delft's Mechanical, Maritime, and Materials Engineering department, who is actively researching neodymium recycling, valuable insights were gathered regarding the recycling of NdFeB magnets. The ongoing extensive research is currently centered on enhancing the recycling process of these magnets, with the intention of achieving industrialization within the next 5 to 10 years. Notably, a significant challenge in the recycling of neodymium magnets is the effective separation of these magnets from iron-based materials.

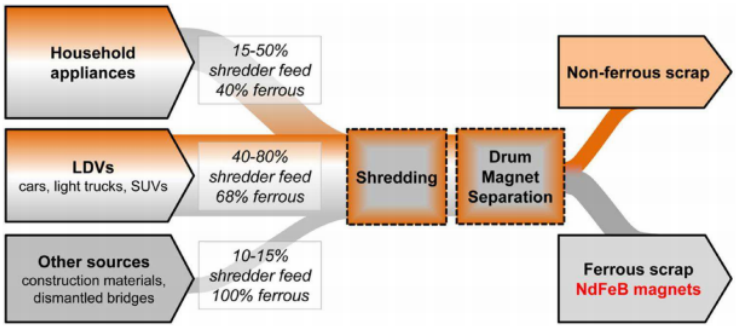

Figure 3.19: Current Industrial shredding process for typical end-of-life products [26]

Figure 3.19 depicts a schematic of the existing industrial shredding process for typical end-of-life products. This diagram illustrates that the shredded materials are separated into ferrous and non-ferrous fractions using a magnetic separation drum. The NdFeB material, which belongs to the ferrous category, presents challenges in separation due to its small particle size and magnetic properties. However, in the specific case of the Biosphere PV module, the absence of iron substances in its constituent materials simplifies the magnet separation process during recycling.

While the potential for recycling exists, the issue of neodymium magnet availability persists. Nevertheless, these magnets were selected for testing their potential in creating modular interconnections due to their strong magnetic field and ease of disassembly, as they can be separated using horizontal physical force. If the electrical performance is unsatisfactory, testing alternative magnets like ferrite magnets, which are made from materials more abundant in the Earth's crust but have lower magnetic field strength, becomes unnecessary.

3.4.3 Temperature Effects on NdFeB Magnets

Understanding how magnets behave in response to temperature changes is crucial for determining their suitability for various applications. The highest temperature at which a magnet can retain its magnetic properties, including magnetic field strength and orientation, is known as its maximum operating temperature. Typically, the maximum operating temperature of a permanent magnet is determined by evaluating the linearity of the B(H) curve or the irreversible loss of flux. As temperature increases, the magnetic flux decreases linearly. However, upon reaching a certain temperature threshold, there is a sudden and non-linear decline in magnetic flux [78]. As per the provided datasheet [79], the selected magnets have a maximum operating temperature of 80 °C. In Section 4.4, it is explained that the thermal cycle test has a maximum temperature of 85°C. This temperature exceeds the rated maximum operating temperature of the magnets.

The Curie temperature signifies the temperature at which the transition from ferromagnetic to paramagnetic behavior occurs [80]. Ferromagnetic materials demonstrate spontaneous magnetization below their Curie temperature, wherein increased thermal motion aligns atomic magnetic moments. This alignment occurs even without an external magnetic field. However, heating the material above the Curie temperature results in random spin orientations, causing a transition to a paramagnetic phase. Paramagnetic materials lack spontaneous magnetization and only align atomic magnetic moments in the presence of an external magnetic field [80]
The Curie temperature for the chosen magnets is 310 °C [79].

CHAPTER 4

Methodology for Characterization

This chapter outlines the testing procedures involved in evaluating the technical feasibility of the concepts discussed in Chapter 3 and the tests planned to characterize the performance of each prototype.

4.1 Electroluminescence Imaging

In order to evaluate the technical viability of the suggested concepts, it is crucial to verify that the solar cells remain intact throughout the prototyping process. Electroluminescence imaging can be used to identify any cracks or defects within the cells, serving as a method of confirmation. PV devices convert light into electrical energy and can emit near-infrared light under electrical excitation. Electroluminescence (EL) is used to analyze PV devices with electrical contacts, where electrons in the valence band are excited and recombine with holes, emitting photons. In crystalline Si solar cells, the emitted light is around 1.1 eV (1150 nm) with a distribution from 950 to 1250 nm due to the nature of an indirect band gap. EL images can detect areas with reduced carrier density, indicating defects such as shunts, interrupted interconnections, and cracks [81].

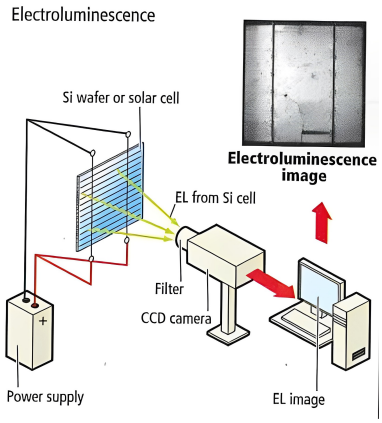

Figure 4.1: Schematic representation of EL imaging setup [82]

Figure 4.1 provides a schematic representation of the setup required for EL imaging.
The procedure for EL imaging is as follows:

1. Create electrical contacts on the PV device to enable current flow and connectivity.
2. Apply a controlled current or voltage to stimulate electron-hole recombination within the device.
3. Photon emission takes place as electrons and holes recombine, releasing energy in the form of light.
4. Utilize a specialized camera equipped with an infrared (IR) filter to capture and record the emitted light from the PV device.
5. Analyze the captured images to identify variations in light intensity and spatial distribution.

Now that the working principle behind EL imaging has been explained, it is important to understand the different types of defects that can potentially be detected using EL imaging. Figure 4.2 demonstrates various types of defects that can be identified using EL imaging.

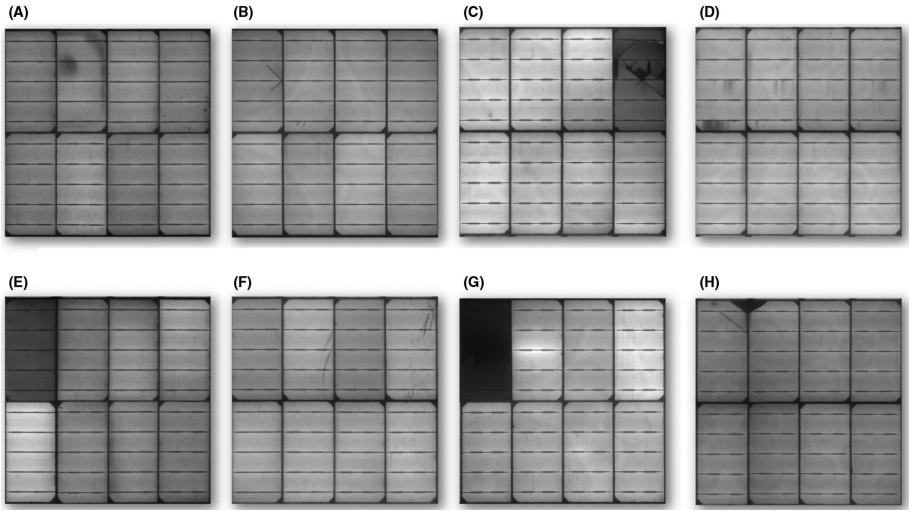

Figure 4.2: Types of defects detected in EL images: (A) Black area, (B) Cracks, (C) Break, (D) Finger failure, (E) Low cell, (F) Scratch, (G) Black cell, and (H) Broken corner [83]

The defects shown in the Figure above are:

1. Black area: An irregular dark region in the EL image, typically resulting from material defects or poor contact caused by improper soldering.
2. Cracks: Cracks that may not be visible to the naked eye but can be detected using EL technology. These cracks can be caused by weak external stresses during manufacturing, transportation, or installation.
3. Break: Severe cracks that completely electrically isolate a portion of the cell from others, appearing as a black area in the EL image. These cracks can be caused by significant external thermal and mechanical stresses.
4. Finger failure: Black lines perpendicular to the bus bar, likely caused by issues such as low printing height, insufficient printing pressure, or problems with bus bar soldering.
5. Low cell: Cells significantly darker than others in the EL image. This is often due to interconnection of cells with different efficiencies onto the same module, resulting in varied minority carrier lifetimes.
6. Scratch: Single or multiple smooth and uneven black lines on the cell, possibly caused by nicks from sharp objects during transportation on the production line.
7. Black cell: One or more cells that appear completely black in the EL image. The causes may include cell short-circuits, low-quality silicon chip material, or cracks from improper soldering processes.
8. Broken corner: Fractured corners in solar cells often result from mechanical stress during handling, manufacturing, or installation processes.

Regions that have lower carrier density, such as shunts, interrupted interconnections, dangling bonds, and contamination, decrease the likelihood of radiative recombination, which makes them identifiable in electroluminescence EL images [81]. Changes in texturing or SiNx layer can affect the amount of the EL light coupled out of the wafer to the camera [82]. The change in intensity of light in EL images of solar cells can be attributed to increased series resistance which in turn causes a voltage drop [84].

4.2 Evaluating Interconnection and Disconnection

Desolderable Interconnections using SnBi solder alloy

In Subsection 3.1.1, the issue of cracking that occurs in cells during the process of desoldering interconnections using the SnAgCu solder alloy is explained. A possible solution to reduce the thermal and mechanical stress during desoldering is to utilize the SnBi solder alloy, which has a lower melting point.

The feasibility of SnBi for desolderable interconnections can be tested using the following procedure:

1. Connect two IBC solar cells in series by soldering the dog-bone wire using the SnBi solder alloy.
2. Desolder the interconnection using the same setup and tools described in Subsection 3.1.1.
3. Resolder the two IBC solar cells that were previously disconnected by desoldering.
4. Configure the string of the two resoldered IBC solar cells in a glass-glass module and analyze the EL image of this prototype to identify if any cracks or defects exist within the cells.
5. Repeat the entire process using the SnAgCu solder alloy and compare the EL image obtained from the SnBi solder alloy prototype.

This procedure can be used for testing the interconnection mechanism which involves soldering two dog-bones as described in Section 3.2.

Contact Pressure based Interconnections within the Cell-Bed

Subsection 3.3.1 explains the interconnection design that relies on a sliding contact pressure mechanism, highlighting its visible disadvantages. It is important to examine the drawbacks that may arise during the assembly of PV modules using this interconnection, as well as during the assembly of PV modules using the interconnection mechanism based on the improved design.

The test procedure to assess the technical viability of the interconnection designs implemented within the cell-bed are outlined below:

1. Construct a glass-glass module configuration prototype comprising two IBC solar cells connected and placed using the cell-bed equipped with the slider-based interconnection mechanism and examine the assembly and disassembly processes for potential faults.
2. Analyze the EL images captured from this prototype to indentify cracks and defects in the solar cells.
3. Construct a glass-glass module configuration prototype comprising two IBC solar cells connected and placed using the cell-bed incorporating the improved interconnection mechanism and observe the assembly and disassembly processes for potential faults.
4. Analyze the EL images obtained from this prototype to indentify cracks and defects in the solar cells.

Magnetic force based contact pressure interconnections

In Section 3.4, the utilization of magnetic force for establishing contact pressure-based interconnections is discussed. It is crucial to examine the assembly and disassembly procedures in order to evaluate potential harm caused by the magnets to the solar cells or the interconnection itself. This is particularly significant due to the high malleability of the dog-bone, which renders it susceptible to bending.

The procedure for evaluating the technical feasibility of the contact pressure interconnection mechanism utilizing magnetic force is described as follows:

1. Create a setup for assembling the magnets and ensure that the selected magnets provide adequate magnetic force to maintain consistent contact and a stable interconnection. Additionally, assess whether the magnetic force causes observable damage to the cells or bending of the dog-bone.

2. Once the assembly is successfully completed, perform disassembly tests by applying horizontal force to remove the magnets. Observe if this step can be carried out effortlessly without causing any harm to the solar cells.

3. Construct a glass-glass prototype that integrates two IBC solar cells connected in series using the interconnection mechanism relying on magnetic force.

4. Utilize EL imaging to inspect the prototype and detect any cracks, damage, or indications of weak interconnections on the cells.

Having outlined the test procedures for evaluating the technical viability of each interconnection mechanism, it is now essential to develop a test procedure to assess the performance of prototypes incorporating different types of interconnection mechanisms.

4.3 I-V Measurement

As explained in Section 2.4, I-V measurements offer a means of analyzing the performance of solar cells and PV modules. These measurements provide insights into the electrical performance of the cells and also allow for the assessment of the influence of series resistance on their overall performance. This is why it is crucial to employ I-V measurements when evaluating the performance of prototypes incorporating different interconnection mechanisms.

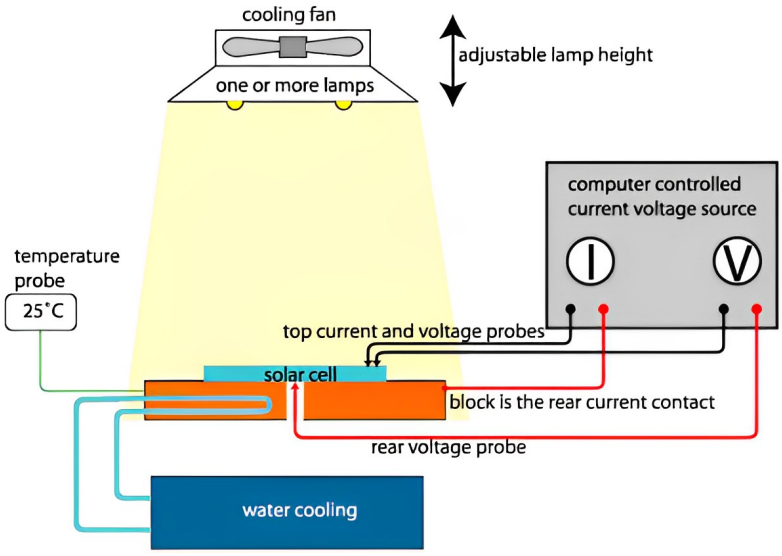

Figure 4.3: Schematic representation of I-V measurement setup [85]

Figure 4.3 provides a schematic representation of the setup required for IV measurement

In this setup, four separate probes are strategically connected to the solar cell. Two probes are used for measuring the voltage across the cell, while the other two probes measure the current flowing through the cell. This 4-probe configuration helps minimize errors caused by contact resistance and long cables, ensuring accurate and reliable measurements of the module's electrical characteristics. The temperature of the solar cell is maintained at 25°C using a water cooling based mechanism.

The measurement is conducted under standard test conditions, which include an irradiance level of 1000 W/m^2, a module temperature of 25°C, and an AM 1.5 spectrum. These standardized conditions enable fair comparisons between different PV modules by providing a consistent benchmark for performance evaluation [22].

4.4 Thermal Cycle Test

Thermal cycle tests play a crucial role in evaluating the reliability and durability of PV modules. These tests simulate extreme temperatures, assessing their ability to withstand temperature variations without degradation or failure. These tests identify potential weaknesses, such as material degradation, solder joint failures, delamination, and provide valuable insights into the long-term performance and reliability of PV modules. Modules that pass these tests demonstrate enhanced durability and are better suited to endure harsh environmental conditions, increasing confidence in their long-term performance and reliability in the field [68].

As outlined in Sections 3.1.3, 3.3.2, and Subsections 3.4.3, the interconnection mechanism's performance can be hindered by effects of temperature variations on solder joints, the polymer utilized in the cell-bed, and the magnets. Therefore, it is crucial to conduct thermal cycle tests on the prototypes to assess the degree of degradation.

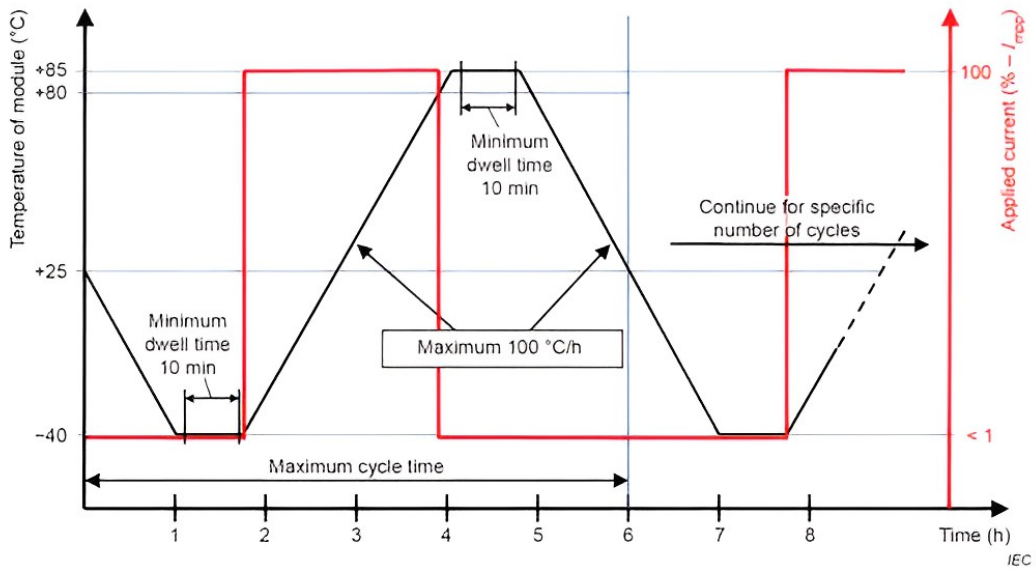

Figure 4.4: Temperature profile for Thermal Cycle test as per the IEC standards [68]

Figure 4.4 illustrates the temperature profile requirements in accordance with the standards set by the International Electrotechnical Commission (IEC). These conditions can be precisely simulated by employing a climate chamber, enabling the conduction of thermal cycle tests within a controlled environment.

The temperature profile must adhere to four key requirements specified by the IEC standards:

1. The thermal cycles temperature set points are -40°C and 85°C.
2. The ramp up and ramp down rates must not exceed 100°C per hour.
3. The dwell time at each temperature extreme must be a minimum of 10 minutes.
4. The entire cycle, encompassing all temperature phases, should not exceed 6 hours.

To conduct the tests, PV modules are placed within the climate chamber, which allows precise control and monitoring of temperature conditions. By programming the climate chamber to follow the defined temperature set points, ramp rates, dwell times, and overall cycle duration, the modules can be subjected to the desired thermal conditions.

The testing procedure for evaluating the performance of the prototypes is outlined as follows:

1. Conduct I-V measurements of the prototypes to assess their electrical performance and evaluate the impact of series resistance on their electrical performance.
2. Place the prototypes inside a climate chamber and subject them to thermal cycles, simulating temperature variations as shown in Figure 4.4.
3. Inspect the prototypes visually for any visible damages or changes in their physical appearance resulting from the exposure to thermal cycles.
4. Remove the prototypes from the climate chamber and perform I-V measurements. Additionally, capture EL images to analyze any degradation in performance.
5. Based on the obtained results, determine if further thermal cycling tests are necessary. If required, repeat steps 3 and 4 with the additional thermal cycles at specific intervals during the thermal cycle test.

By following this testing procedure, the performance of the prototypes can be effectively evaluated, considering both their electrical characteristics and their ability to withstand thermal stress.

CHAPTER 5

Prototyping and Testing of Interconnection Methods

This chapter focuses on the evaluation of technical feasibility for the concepts presented in Chapter 3, as well as the prototyping process for all interconnection concepts, including the reference prototypes.

With the exception of the prototype featuring magnetic force-based interconnections and the EVA reference prototype, the construction of all prototypes adheres to the Biosphere Solar PV module structure.
Figure 5.1 represents the steps involved in the making of prototypes based on the Biosphere Solar PV module structure.

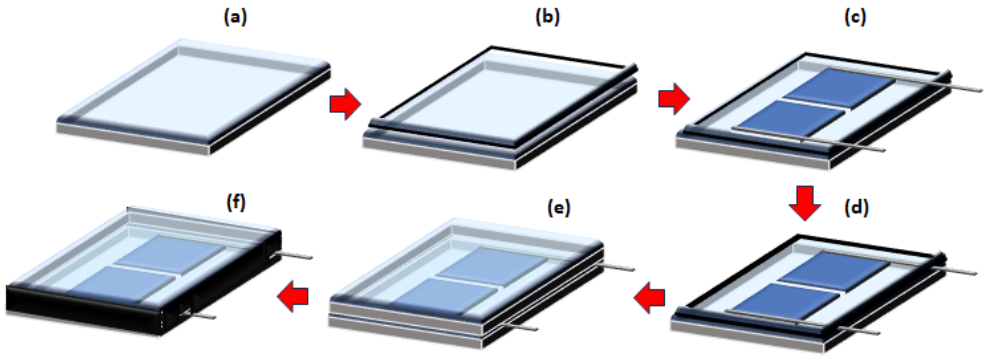

Figure 5.1: Construction process for prototypes built following the Biosphere Solar PV module structure

The construction process for the prototypes built following the Biosphere Solar PV module structure involves the following steps:

1. Cutting 3mm thick glass for the front and back glass such that the dimensions allow sufficient space for two solar cells to be connected in series using the different interconnection mechanisms, spacers, desiccant sachets and the PIB edge seal layers.

2. Applying two layers of PIB edge seal to the bottom glass (as shown in Figure 5.1(b)), and placing a pair of solar cells connected in series onto the bottom glass. These cells should also be connected to the busbars, as depicted in Figure 5.1(c).

3. Applying two more layers of PIB edge seal such that they overlap the busbars (as seen in Figure 5.1(d)).

4. Affixing desiccant sachets on the bottom glass to absorb moisture, and spacers/cell-beds to maintain cell spacing and hold the solar cells.

5. Positioning the top glass on top of the edge seal stack and applying mechanical pressure to ensure strong bonding between the glass and PIB edge seal (as seen in Figure 5.1(e)).

6. Applying EPDM (ethylene propylene diene monomer) rubber tape to the edges to protect the hands from being cut by the glass (as seen in Figure 5.1(f)).

After the construction of the prototypes, EL images are captured to inspect the solar cells for any potential damage. For the EL test, the prototypes are connected in forward bias with a dc-supply and the current of the dc-supply is set to 90% of the solar cell's rated short circuit current. The EL images of all the prototypes except the EVA reference prototype were taken at the Biosphere Solar workspace.

5.1 Desolderable Interconnection using Single Dog-bone

To conduct the desoldering test on the dog-bone soldered with the SnBi solder alloy, we utilized the setup and tools described in Section 3.1.1. As explained earlier, the temperature of the soldering iron was set to 240°C, specifically chosen to achieve solder joints with lower wetting angles. With this temperature, both the soldering and desoldering processes were implemented successfully. During the test, it was observed that the tin coating on the dog-bone no longer melted, resulting in a significant reduction in the amount of physical force needed to separate it from the solar cell. The desoldering process of the dog-bone is illustrated in Figure 5.2a, while Figure 5.2b demonstrates the successful separation of the dog-bone from the solar cell.

(a) **(b)**

Figure 5.2: (a) Desoldering dog-bone soldered using SnBi solder alloy, and (b) Dog-bone desoldered from adjacent solar cell

In order to evaluate the presence of cracks resulting from the desoldering process, the desoldered cells were resoldered and incorporated into a glass-glass configuration of the Biosphere Solar PV module structure, forming a prototype. Subsequently, EL image ofthe prototype was captured to detect any potential micro-cracks or cracks along the edges of the solar cells. Figure 5.3 displays the finished prototype, while Figure 5.4a presents the electroluminescence (EL) image of the prototype.

Figure 5.3: Prototype with cells soldered using Sn42Bi58 solder alloy

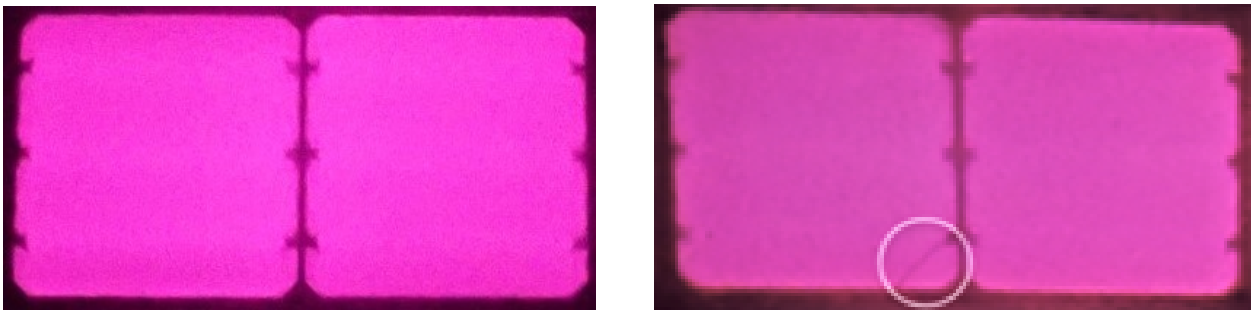

(a) (b)

Figure 5.4: (a) EL image of the SnBi solder based resoldered cells prototype, and (c) EL image of the SnAgCu solder based resoldered cell prototype

The EL image presented in Figure 5.4a shows that both cells in the prototype depicted in Figure 5.3 remain crack-free even after the desoldering and resoldering process. In contrast, Figure 5.4b illustrates the EL image of a prototype containing two solar cells soldered with the standard SnAgCu solder alloy, which were subsequently desoldered and resoldered. The presence of cracks in this case resulted from the additional physical force applied during the separation of the dog-bone from the solar cell during the desoldering process. Another prototype, made by connecting two solar cells in series using a single dog-bone soldered with the SnBi solder, was created for performance assessment.
The testing of soldering using IR lamp is described in Appendix A.

5.2 Melting Two Dog-bones for Desolderable Interconnection

To assess the desoldering capabilities of the interconnection method discussed in Section 3.2, a test was conducted. In this test, two separate dog-bones were soldered to the positive and negative sides of two solar cells using the low melting point SnBi solder alloy. The solar cells were positioned in a way that the contact regions of the dog-bones, which were not soldered to the solar cells, overlapped. A soldering iron set at 270°C (since the melting point of tin is around 240°C) was used to create a molten joint by fusing the tin coating of the overlapping contact regions together.
Figure 5.5a illustrates the soldered configuration of the two dog-bones.

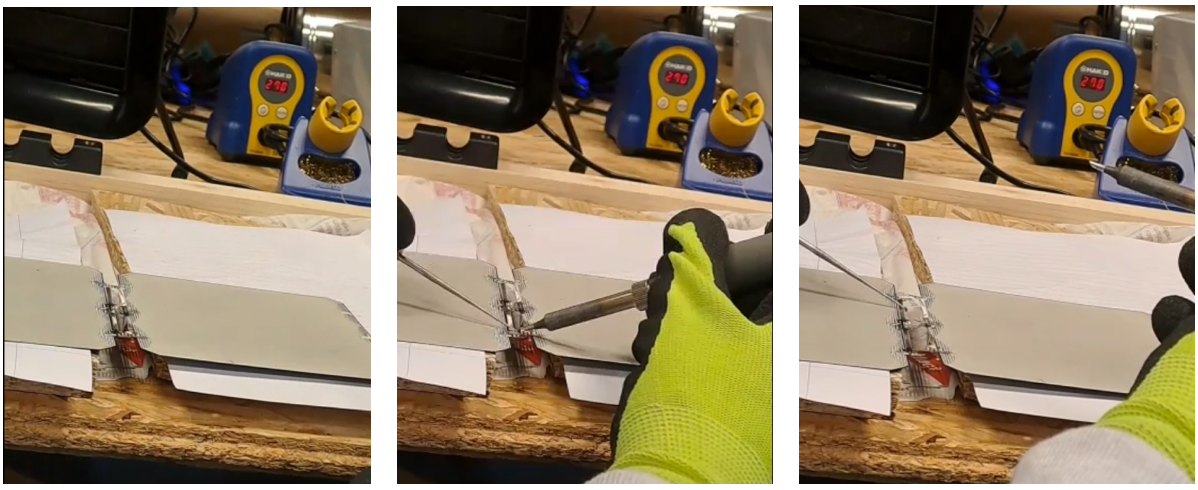

(a) (b) (c)

Figure 5.5: (a) Interconnection based on two dog-bones soldered to each other (b) Desoldering process for disconnecting two dog-bones soldered to each other, and (c) Disconnection of the two dog-bones after the desoldering process is completed

During the desoldering process, the same setup that was used for desoldering a single dog-bone was utilized. Throughout this procedure, the contact regions of the left-side dog-bone, which were overlapped

by the right-side dog-bone's contact regions, were pressed down using a needle-file. Simultaneously, heat from the soldering iron, set at a temperature of 270°C, was applied to the contact regions of the right-side dog-bone (as seen in Figure 5.5b). This heat was sufficient to melt the existing molten joint, and as the needle-file exerted physical pressure to depress the overlapped contact regions of the left-side dog-bone, the connected contact regions were successfully desoldered. Figure 5.5b illustrates this process, while Figure 5.5c shows the completion of desoldering process. Throughout this entire procedure, it was observed that there was no direct or indirect physical stress exerted on the IBC solar cells, minimizing the risk of damage.

Incorporating the glass-glass configuration of the Biosphere Solar PV module, a prototype was fabricated using a pair of solar cells initially connected in series through a soldered two dog-bone interconnection, as depicted in Figure 5.5a. The interconnection was then disassembled by desoldering the contact regions, as shown in Figure 5.5b. Subsequently, the interconnection was reestablished by soldering the overlapping contact regions. An EL image of the prototype was captured to detect possible micro-cracks, cracks, and other defects in the solar cells. Figure 5.6a depicts the prototype after it was built and Figure 5.6b shows the EL image of the prototype. The EL image shows no visible defects and cracks in the cells.

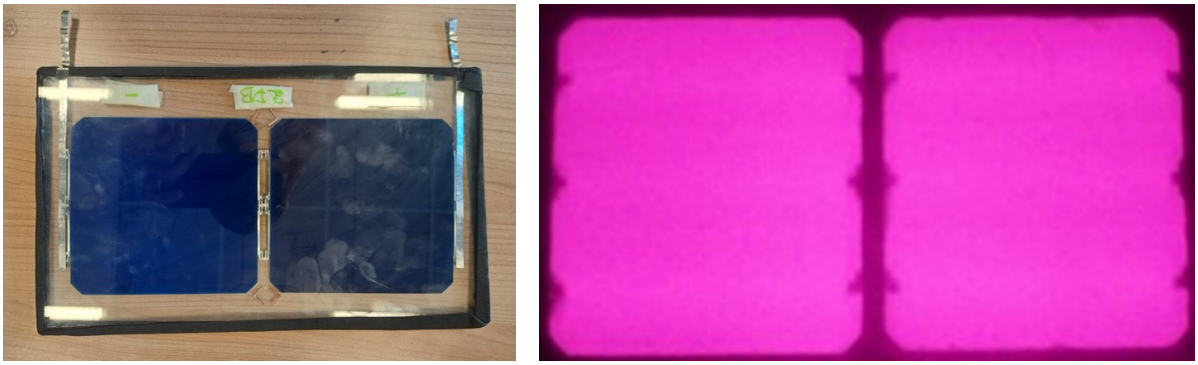

(a) **(b)**

Figure 5.6: (a) Prototype with interconnection based on two dog-bones resoldered to each other, and (b) EL image of the prototype with interconnection based on two dog-bones soldered to each other

5.3 Interconnections based on the Cell-Bed

To examine the EL image of two solar cells connected using the cell-bed with slider based interconnection mechanism, as described in Subsection 3.3.1, a prototype was created. The two dog-bones utilized to create the interconnection are soldered to the solar cells using the SnAgCu solder alloy.

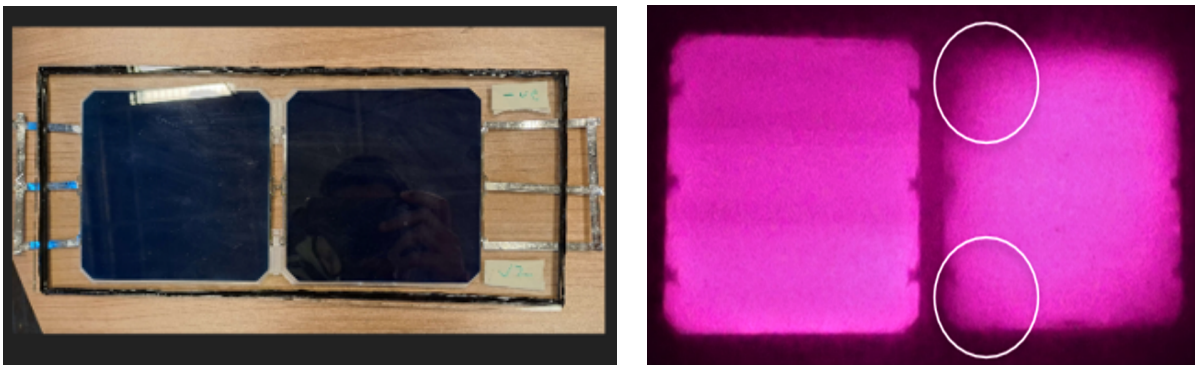

(a) (b)

Figure 5.7: (a) Prototype consisting the cell-bed with slider based interconnection mechanism, and (b) EL image of the prototype consisting the cell-bed with slider based interconnection mechanism

Figure 5.7a depicts the prototype featuring the cell-bed mechanism, while Figure 5.7b displays the electroluminescence (EL) image obtained from this prototype. In Figure 5.7b, the highlighted areas indicate dark regions, which can indicate material defects, or non-uniform interconnections as described in Section 4.1.

Further examination of the slider mechanism revealed that when the required force is applied to the contact region between the two dog-bones to enable smooth sliding of the slider, the dog-bones, being malleable, tend to bend. This bending leads to uneven contact, which cam impede the flow of current and resulting in the observed dark regions.

To summarize the previously mentioned drawbacks in Subsection 3.3.1 and the subsequent discussion, three main issues were identified:

1. Insufficient contact pressure in the central contact region between the two dog-bones.
2. Increased distance between adjacent solar cells.
3. Lack of uniform contact caused by the slider mechanism.

To address these limitations, the product designers at Biosphere Solar were advised to implement the following recommendations:

1. Decrease the cell-cell spacing by replacing the slider-based mechanism with a single strip, thereby eliminating the need for a groove to fit the slider.
2. Ensure that the single strip is wide enough to apply evenly distributed contact pressure on the contact regions of the dog-bones such that it does not lead to deforming or twisting of the dog-bones. Also, the single strip should enable contact pressure to be applied in the central overlapping regions of the interconnection.
3. Incorporate holes in both the strip and the cell bed, allowing the use of screws to apply contact pressure while ensuring that the screws do not come into direct contact with the dog-bones.

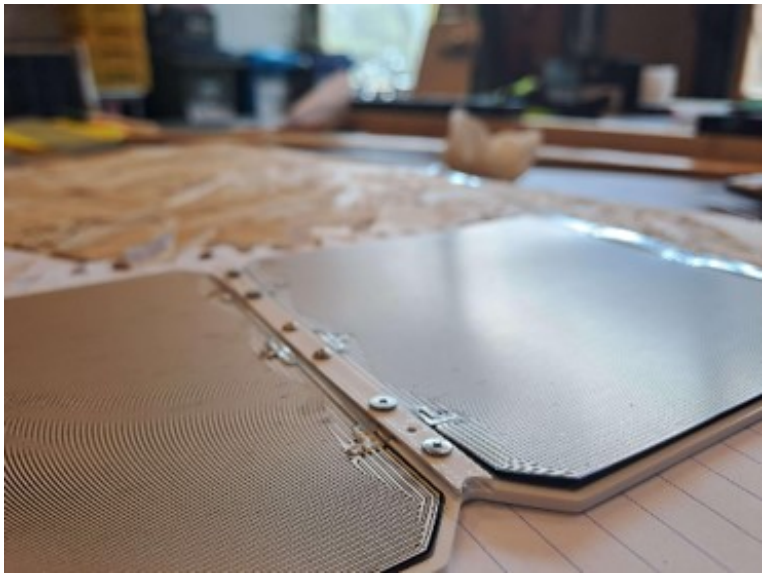

Figure 5.8: Initial Improved cell-bed with with single-strip based interconnection

Following the implementation of the recommendations mentioned above, a new cell-bed was printed (as seen in Figure 5.8).
This new design showed several changes compared to the cell-bed with slider based mechanism. Firstly, the cell spacing was reduced by 0.3 cm (0.15 cm on each side). Consequently, the distance between cells was decreased from 1.1 cm in the cell bed with a slider-based interconnection mechanism (depicted in Figure 5.9(a)) to 0.8 cm in the improved cell bed with interconnections based on a single strip (as shown in Figure 5.9(b)). Nevertheless, the cell-to-cell spacing in the improved cell bed still exceeds that of the conventional single dog-bone based interconnection, which measures approximately 0.38 cm (as shown in Figure 5.9(c)).

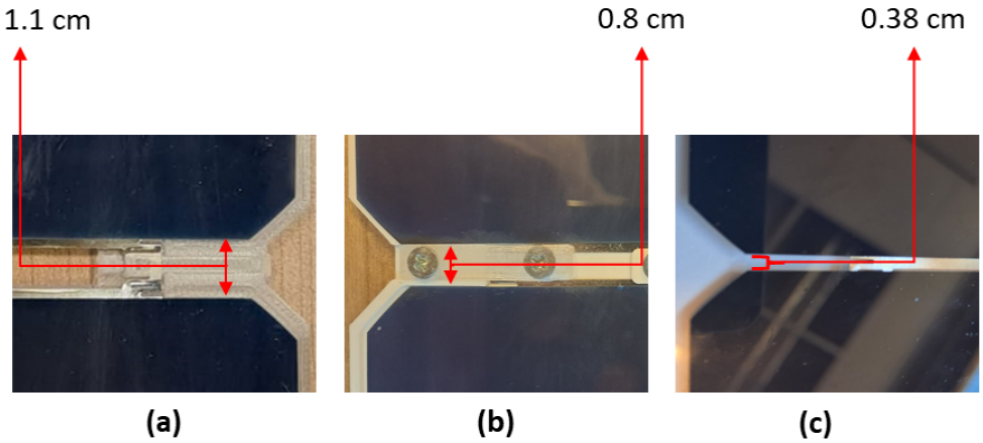

Figure 5.9: (a) Cell-Cell distance in slider based interconnection mechanism in the cell-bed, (b) Cell-Cell distance in the improved cell-bed design based on single-strip, and (c) Cell-Cell distance in the conventional single dog-bone based interconnection

Secondly, the overlapping contact area between the two dog-bones increased by approximately 50% compared to the slider-based mechanism. The dimensions of the overlapping regions were measured using a vernier caliper. Figure 5.10(a) illustrates the overlapping regions of the dog-bone (highlighted in red) in the cell-bed with the slider-based interconnection mechanism. In this figure, three overlapping regions with the dimensions 3 mm × 4 mm each can be observed. Using these dimensions, the area of the overlapping contact is calculated: 3 mm × 3 mm × 4 mm = 36 mm^2. Figure 5.10(b) shows that with the improved cell-bed design, there is an additional overlapping area (highlighted in yellow) in comparison to the overlapping area in the cell-bed based on the slider-based interconnection mechanism (highlighted in red). The overlapping contact area for the improved cell-bed design is calculated: 3 mm × 3 mm × 6 mm = 54 mm^2. The percentage increase in the overlapping area is calculated by subtracting the overlapping contact area of the dog-bone in the improved cell-bed design from the overlapping contact area of the dog-bone in the cell-bed with the slider-based interconnection and dividing the result by the overlapping contact area of the dog-bone in the cell-bed with the slider-based interconnection.

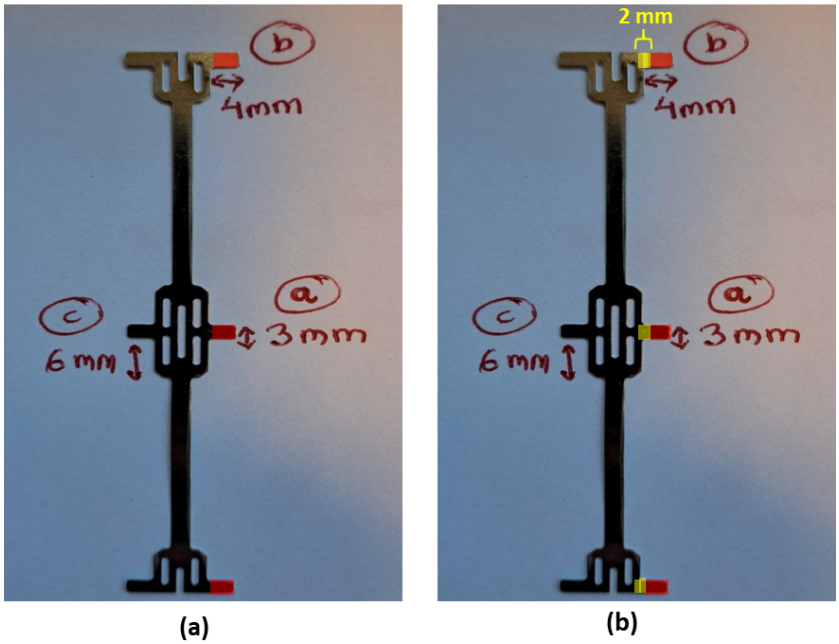

Figure 5.10: (a) Overlapping regions of the dog-bones in slider based interconnection mechanism in the cell-bed, and (b) Overlapping regions of the dog-bones in the improved cell-bed design based on single-strip

Lastly, the overlapping regions of the dog-bones would no longer twist and deform and contact pressure was applied to the central overlapping region in the interconnection. Figure 5.8 illustrates two solar cells connected in series using the single strip-based contact pressure mechanism.

During the assembly process, it was noticed that the single strip did not distribute pressure evenly across all contact regions. This uneven distribution occurred because it was challenging to keep the single strip in place while tightening the screws, leading to incomplete pressing towards the edges. Furthermore, tightening the screws resulted in frequent shaking of the solar cells. These issues were resolved by dividing the strip into three parts, allowing each part to apply pressure on the overlapping regions of the two dog-bones (as seen in Figure 5.11a). This solution improved the contact pressure distribution and reduced shaking during screw tightening.

The illustration depicted in Figure 5.11b exhibits a pair of strips fastened onto the upper and middle sections of the two dog-bone configuration using screws, while the holes that have been created to accommodate the screws can be seen in the lower portion. Note that the solar cells are covered with paper to avoid scratching of the top surface.

(a) (b)

Figure 5.11: (a) 3D printed cell-bed with three-strips based interconnection, and (b) Interconnection mechanism with the three-strips based cell-bed design

A prototype was constructed following the Biosphere Solar PV module structure. Initially, two solar cells were connected using the improved cell-bed with three-strips based interconnection. Subsequently, the solar cells were disconnected by loosening the screws, removing the strips, and removing the solar cells. The solar cells were then reconnected by placing them into the cell-bed and tightening the screws on the three strips, applying contact pressure to the overlapping regions of the dog-bones. Figure 5.12a illustrates the prototype featuring the improved cell-bed version. One out of the three contact strips is printed using PETG, while the other strips and the cell-bed are printed using ABS. This choice was made to observe any potential warping of the PETG strip during thermal cycle tests.

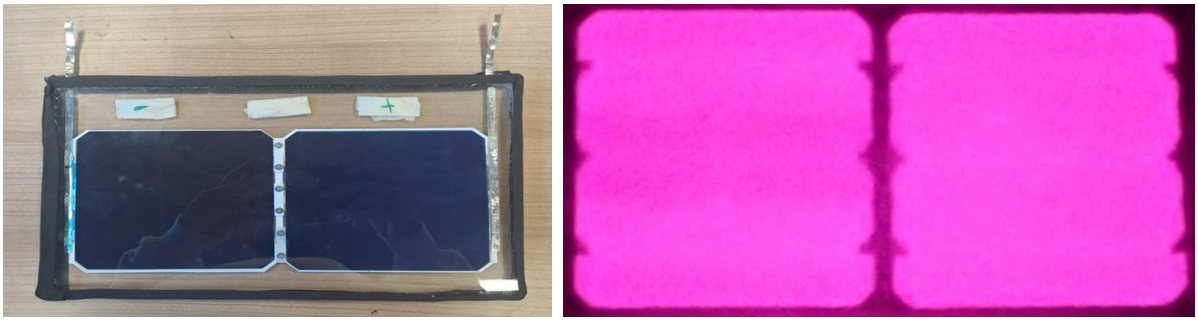

(a) (b)

Figure 5.12: (a) Prototype with the improved cell-bed made after reassembly of two solar cells, and (b) EL image of the prototype consisting final improved cell-bed

Figure 5.12b presents the EL image of this prototype. Notably, the image demonstrates the absence of cracks and dark regions observed in Figure 5.7b.

The disassembly of this interconnection involves loosening the screws, removing the strips, and then taking out the solar cells.

5.4 Magnetic Force based Interconnections

To test the assembly and disassembly of this interconnection, initially cylindrical magnets with the dimensions: 1mm radius and 1.5mm height were procured. During the assembly, it was discovered that the bottom and top surface area of a single magnet (6.8mm^2) was not large enough to cover the overlapping contact region between two dog-bones (surface area = 12mm^2) and the dog-bone contact regions would slip away, have uneven contact pressure and bend in the center due to their highly malleable structure. Thus magnets with radius 2mm, 2mm height and base area 12.56mm^2 were used (as seen in Figure 5.13a). Each of this magnet can apply a force of approximately 4.12 N [79].

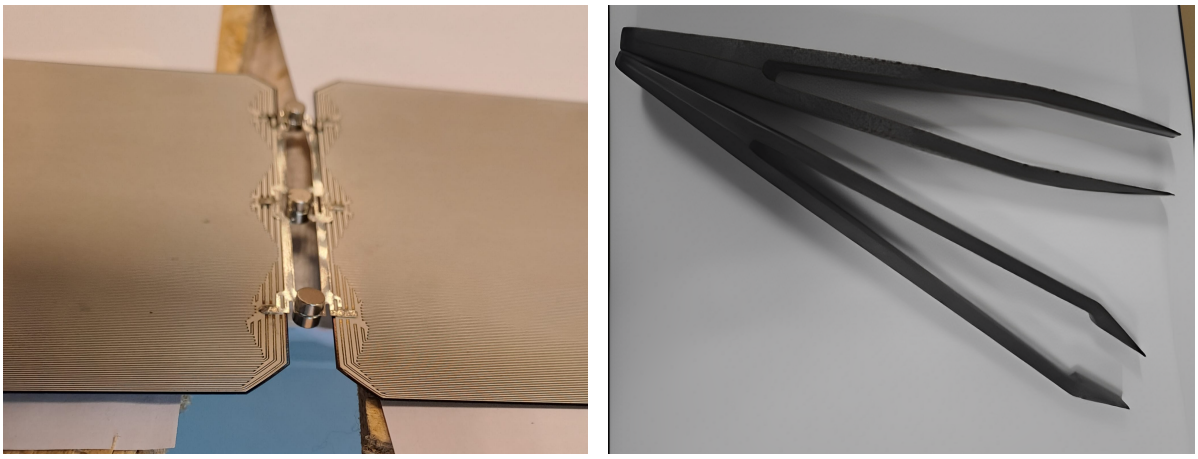

(a) (b)

Figure 5.13: (a) Magnets placed on overlapping contact-regions between two dog-bones, and (b) Polycarbonate tweezers used for placing the magnets

It was observed during the assembly that the magnets would unnecessarily become attracted to each other and stick together when brought closer to the overlapping regions, failing to align properly. This issue stemmed from the insufficient grip when attempting the task manually by hand. To overcome this difficulty, polycarbonate tweezers (shown in Figure 5.13b) were used. These tweezers ensured a secure grip on the magnets, enabling them to be held closely together without experiencing undesired magnetic attraction and subsequent sticking to one another.

It was also observed that placing these magnets in perfect alignment was challenging due to their high magnetic strength. When attempting to align them using horizontal force after placing them on the dog-bone contact regions, it was observed that the solar cells would crack closer to the dog-bone - solar cell contact regions, likely due to the physical force exerted by these magnets.
Despite this, removal of the magnets was easy, it could be achieved by applying horizontal force on both the magnets in the same direction.

The prototype based on the interconnection of two IBC solar cells using the magnetic force-based contact presssure mechanism (as seen in Figure 5.14a) was constructed following these steps:

1. Two appropriately sized glass sheets were cut out of 3mm glass.
2. A layer of PIB edge seal was applied to the bottom glass, and a window spacer rod (known as IGU spacer [86]), typically used in window systems, was cut and placed on top of the edge seal layer. The spacer rod contained desiccant to absorb moisture through tiny holes on one the insides. The height of the magnets posed a challenge in creating the prototype solely with the edge seal, necessitating the use of the window spacer rod.
3. Two dog-bones were soldered to two IBC solar cells using the SnAgCu solder alloy, with the non-soldered contact regions of the two dog-bones overlapping each other to create a series connection.
4. NdFeB cylindrical magnets measuring 2mm in radius and 2mm in height were placed on top and bottom of the overlapped contact regions, as depicted in Figure 5.13a, to apply contact pressure and create the interconnection.
5. Once the series interconnection of the two solar cells was completed, busbars were soldered onto the opposite sides of the solar cells using two additional dog-bones. The solar cells were then disconnected from each other by removing the magnets through the application of horizontal force. After separating the solar cells, they were reconnected by reproducing the assembly depicted in Figure 5.13a and the solar cells were then placed onto the bottom glass. A layer of thick silicone adhesive was added beneath the busbars to compensate for the 2mm height elevation caused by the magnets.
6. Another layer of PIB edge seal was added on top of the window spacer rod to facilitate adhesion between the top glass and the spacer rod.
7. The top glass was placed over the top layer of the PIB edge seal, and adequate mechanical load was applied to ensure proper bonding between the glass and the edge seal.

The EL image of the prototype (depicted in Figure 5.14b) demonstrates a consistent and uniform current distribution across the solar cells, with no observable cracks.

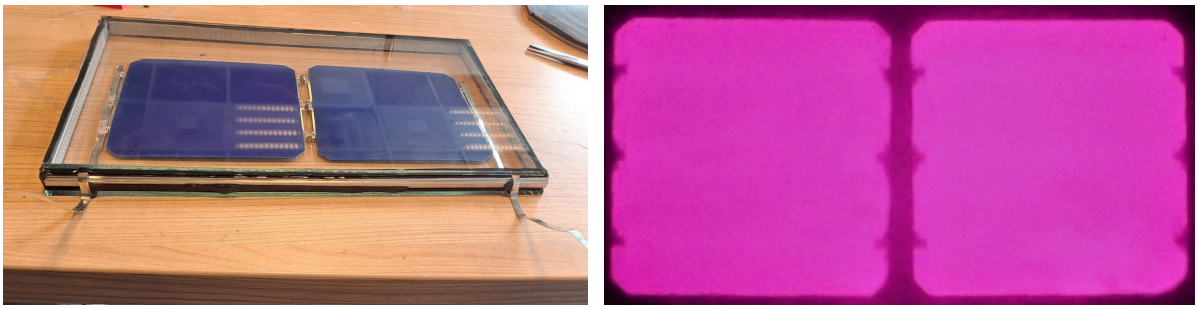

(a) **(b)**

Figure 5.14: (a) Prototype with magnetic force based contact pressure interconnection, and (b) EL image of the prototype consisting magnetic force based contact pressure interconnection

5.5 Reference Prototypes

To facilitate performance comparison among the prototypes, two reference prototypes were created. The first reference prototype is based on the Biosphere Solar PV module structure with interconnections made using a single dog-bone soldered with the standard SnAgCu solder alloy. This prototype is referred to as the "SnAgCu" prototype.
The second reference prototype followed the conventional glass-glass PV module structure, where solar cells were encapsulated between two layers of EVA laminate and interconnected using a single dog-bone soldered with the SnAgCu solder alloy. This prototype is referred to as the "EVA" prototype.
These reference prototypes serve as benchmarks for evaluating the performance of the prototypes made with the disconnectable interconnection techniques mentioned previously.

SnAgCu Prototype

Figure 5.15a depicts the prototype after it was built and Figure 5.15b depicts the EL image of the prototype which shows no visible defects and cracks in the cells.

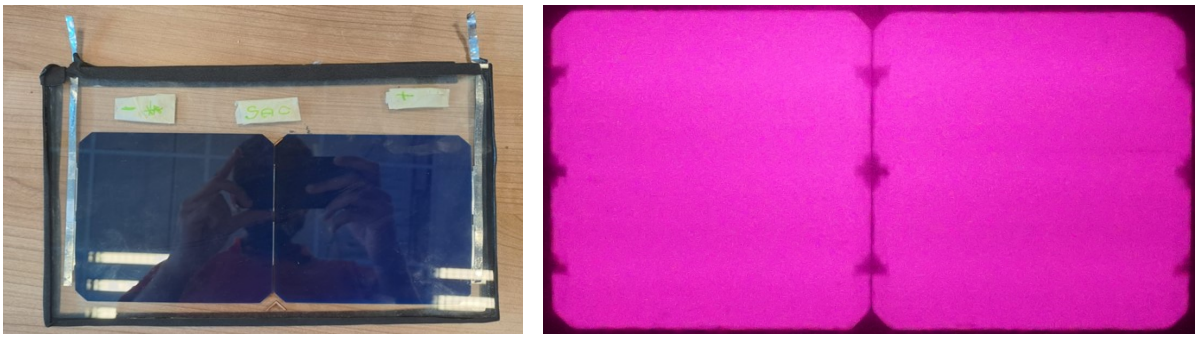

(a) (b)

Figure 5.15: (a) SnAgCu reference prototype, and (b) EL image of the SnAgCu reference prototype

EVA Prototype

The EVA prototype is designed as an industrial standard reference for comparing measurements among prototypes with different disconnectable interconnection mechanisms. This is because the PV industry commonly employs EVA encapsulation, unlike Biosphere Solar. The prototype consists of two IBC solar cells connected in series using a single dog-bone interconnection soldered with the standard SnAgCu solder alloy. The cells are encapsulated using EVA for consistency with industry practices.

The construction of this prototype was carried in the ESP lab of TU Delft and followed the subsequent steps:

1. Two glass pieces were cut out of 3mm thick glass to meet the specified size requirements.
2. Two sheets of EVA laminate were cut to match the size of the glass sheets.
3. Two IBC solar cells were interconnected using a single dog-bone soldered with SnAgCu solder alloy. They were placed on top of an EVA sheet and the EVA sheet was placed on the bottom glass, with the smooth side of the EVA sheet touching the rear-side of the cells and the textured side touching the bottom glass.
4. The front side of the solar cells was covered with a second EVA sheet, and then the top glass was placed on top of the EVA sheet. The arrangement ensured that the smooth side of the EVA sheet made direct contact with the front side of the solar cells, while the textured side of the EVA touched the top glass. This setup effectively protected and insulated the solar cells, allowing them to efficiently generate electricity from sunlight.
5. This stack was placed inside the laminator at ESP lab and the laminator was set for the standard recipe in order to melt the EVA sheets and create an encapsulation which also bonds the top and bottom glass.

(a) **(b)**

Figure 5.16: (a) EVA reference prototype, and (b) EL image of the EVA reference prototype

Figure 5.16a depicts the prototype after it was built and Figure 5.16b shows the EL image of the prototype.

For the EL test, the prototype was connected in forward bias with a dc-supply and the current of the dc-supply was set to 90% of the solar cell's rated short circuit current. Note: the color of this EL image is different than the other EL images because this EL image was taken in the PVLAB at TU Delft, which has a different filter lens attached to the camera. The EL image shows no visible defects and cracks in the cells.

CHAPTER 6

Experimental Results and Discussion

This chapter is dedicated to presenting the experimental results aimed at characterizing the performance of all prototypes. The analysis begins with a comparison of I-V measurements for the reference prototypes. Subsequently, the I-V measurements of all prototypes employing disconnectable interconnections are compared with those of the reference prototypes. The comparison encompasses parameters such as maximum power and series resistance for all prototypes. The chapter concludes by presenting visual observations, observations based on EL images, and the electrical parameters acquired during the thermal cycle test.

6.1 I-V Measurement Setup.

The I-V measurements of the prototypes were performed using the Enlitech lamp as the light source and a Keithley 2651a source meter unit as the variable load. Enlitech software was utilized to collect measurement data, control the source meter unit's voltage, operate the lamp shutter, and set the light intensity to $1000 W/m^2$. The Keithley 2651a source meter unit is a versatile device with a 200W DC power rating that serves as both a source and sink. It limits current to 20 A for 10 V, 10 A for 20 V, and 5 A for 40 V [87]. To ensure accurate measurements, the voltage limit was set to 20 V, considering the total current flowing through series-connected solar cells. The IBC cells used in this thesis have a rated short circuit current of approximately 6.3 A [54].
Figure 6.1 shows the Enlitech lamp emitting $1000 W/m^2$ light onto a prototype, and the I-V measurement is recorded using Enlitech software. Four probes are connected to the busbars of the prototype, linked to both the positive and negative sides of the two cells interconnected in a series configuration based on the four-point contact method described in Section 4.3.

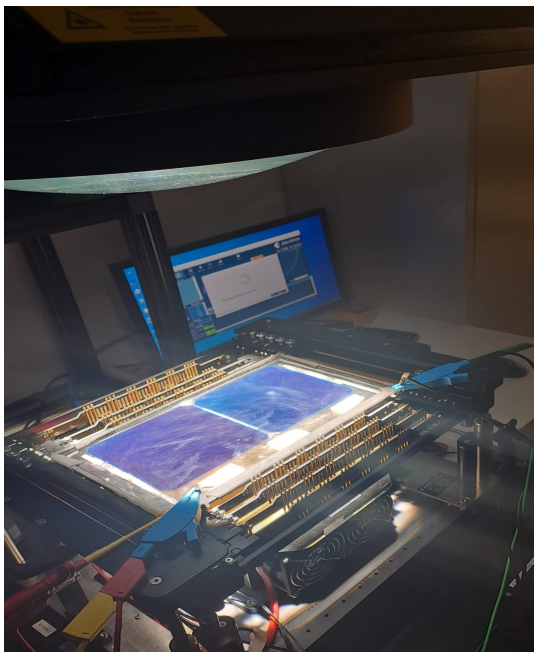

Figure 6.1: Prototype placed under the Enlitech lamp during I-V measurement

The chosen voltage range of -0.1 V to 1.4 V ensures that the maximum total voltage across the prototypes can be measured considering the V_{oc} of two IBC solar cells connected in series to be around 1.38 V. As per standard practice, the step-size was set to 0.04 with a delay time of 150 μs is set between each measurement.

6.2 Analysis of I-V Characteristics

In this section, an analysis of I-V measurements is presented, which involves comparing the performance of reference prototypes with one another and with prototypes containing different disconnectable interconnection mechanisms.

6.2.1 I-V Curve Comparison of Reference Prototypes.

The I-V curves of the reference SnAgCu and EVA prototypes are depicted in Figure 6.1.

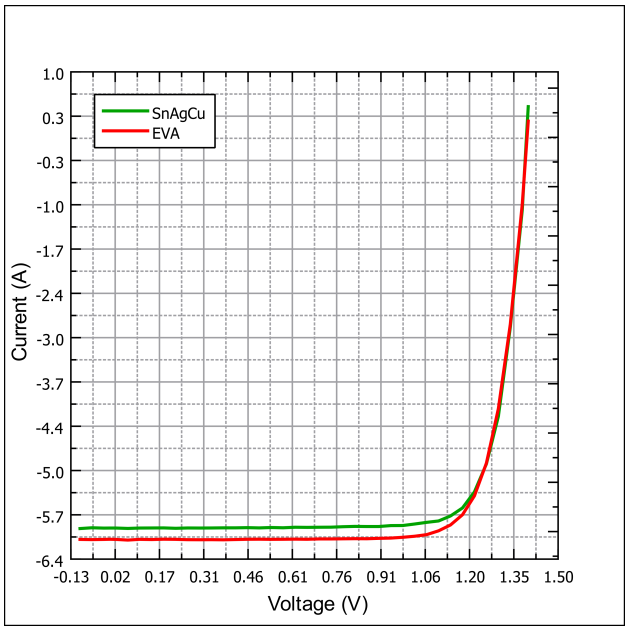

Figure 6.2: I-V curves of reference prototypes

As discussed in Section 5.5, the reference prototypes are based on an identical interconnection mechanism, utilizing a single dog-bone soldered with the SnAgCu solder alloy. The sole distinction between the two lies in the lamination process: the EVA prototype is laminated using EVA and based on the traditional glass-glass PV module structure, while the SnAgCu prototype is based on the Biosphere Solar PV module structure (has no lamination).

Table 6.1 presents the performance parameters obtained from I-V measurements of the reference prototypes. From the I-V curves shown in the Figure 6.2 and the data shown in the Table 6.1, it can be observed that the V_{oc} is the same for both prototypes, however the EVA prototype has a larger short circuit current I_{sc} than the SnAgCu prototype. The EVA prototype shows a higher maximum power (P_{max}) primarily due to its greater maximum current. The EVA prototype achieves higher efficiency as a result of its increased P_{max}.

Table 6.1: Performance parameters of reference prototypes

Prototype	V_{oc} (V)	I_{sc} (A)	P_{max} (W)	Efficiency (%)	Fill-Factor (%)
SnAgCu	1.39	5.90	6.60	21.58	80.47
EVA	1.39	6.07	6.72	21.98	79.64

The slightly lower fill-factor (FF) of the EVA prototype can be attributed to the higher short circuit current.

In order to comprehend the differences in short circuit current variation, it is crucial to acknowledge that the EVA prototype incorporates a layer of EVA material between the glass and the front side of the solar cells. Conversely, the SnAgCu prototype has air between the glass and the front side of the solar cells. This variation in medium can impact the light transmission characteristics of the prototypes, leading to differences in short circuit current.

6.2.2 Unraveling the Implications of Optics.

The inclusion of EVA in PV modules improves performance by enhancing optical performance through refractive index grading. EVA's refractive index helps minimize interface reflections, which contributes to improved efficiency.

In order to investigate the impact of EVA on optical parameters, two different structures are analyzed: the glass-glass PV module structure with EVA (Figure 6.3a) and the Biosphere Solar PV module structure (Figure 6.3b).

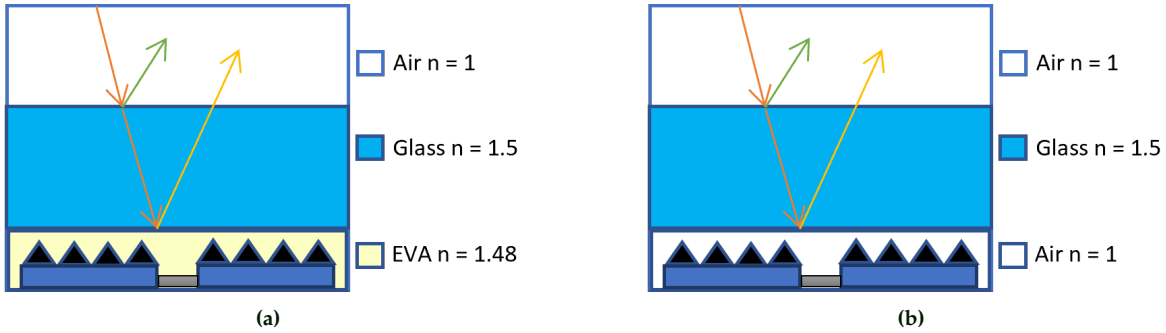

Figure 6.3: (a) Structure of glass-glass PV module with EVA, and (b) Structure of glass-glass PV module without EVA

Using the reflectivity formula for normal incidence of light [22]:

$$R = \left(\frac{n_1 - n_2}{n_1 + n_2}\right)^2 \tag{6.1}$$

Where R represents reflectivity and n denotes refractive index, the reflectivity of the air-glass interface is calculated to be 4%. This is based on the refractive index values of air = 1 [88] and glass = 1.5 [89]. Similarly, considering the refractive index of EVA as 1.48 [90], the reflectivity of the glass-EVA interface is found to be 0.0045%, which can be approximated as 0% due to its negligible value.

Combining these results, the total reflectivity for the glass-glass PV module structure with EVA is 4%. Notably, the reflectivity of the solar cell is not considered in this analysis for simplicity.

Examining the structure in Figure 6.3b, both the top air-glass interface and the glass-air interface have a reflectivity of 4% each, as the refractive indices remain unchanged. Consequently, the total reflectivity for this structure amounts to 8%. Therefore, the reflectivity of the Biosphere PV module is 4% higher than that of the conventional EVA module.

To evaluate reflectivity's role in the measurements, the rated short circuit current of the single solar cell is considered, which is 6.34 A [54].

By adding the 4% reflectivity loss in the top air-glass interface of the EVA prototype, the short circuit current can be adjusted by: 6.34 · (1 - 0.04). This yields a short circuit current of 6.086 A, which is close to the measured short circuit current of 6.07 A of the EVA prototype.

In contrast, based on the reflectivity calculations for the biosphere PV module structure, it is evident that the prototype without EVA would experience at least a 4% higher reflectivity compared to the EVA-equipped version. Considering this additional 4% loss, the short circuit current can be adjusted: 6.34 · (1 - 0.08) = 5.83 A. This value is approximately 1.18% lower than the measured short circuit current of the SnAgCu prototype (5.9 A). This 1.18% deviation can be attributed to factors such as potential measurement equipment errors, temperature variation and height difference created by the back glass of the prototype.

6.2.3 Prototypes with Cell-Bed based Interconnections

Figure 6.4 depicts the I-V characteristics of two prototypes: one employing the cell-bed with slider-based interconnection configuration and the other featuring the improved cell-bed design.
The "Cell-Bed with sliders" prototype utilizes a slider mechanism for contact pressure, as discussed in Subsection 3.3.1, which was developed prior to the initiation of this thesis.
In contrast, the "Cell-Bed improved" prototype incorporates screws and strips to apply contact pressure on the interconnections, as explained in Section 5.3.

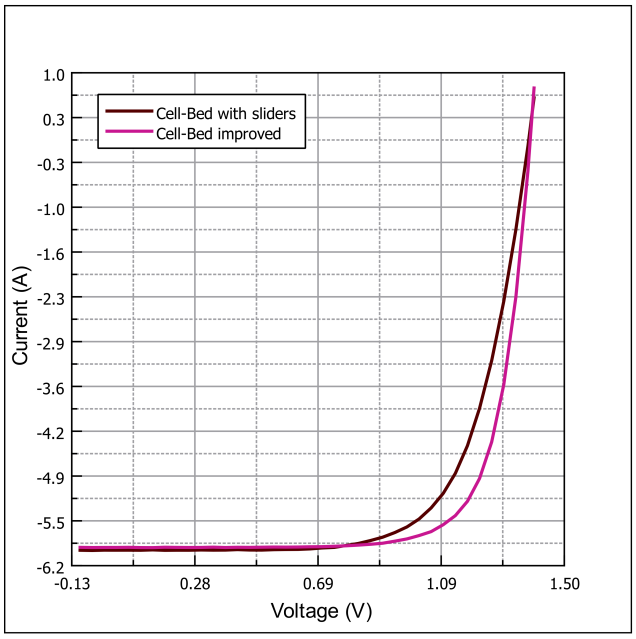

Figure 6.4: I-V curves of prototypes with cell-bed based interconnections

Section 5.3 describes the improved cell-bed design, which achieves a reduction of the cell-cell distance by 0.3 cm by eliminating the slider mechanism entirely. This reduction increases the overlapping contact area between the two dog-bones by 50%. Furthermore, the design resolves issues of insufficient contact pressure in the middle region by utilizing screws and strips, replacing sliders and reducing non-uniform contact caused by bending. These improvements can effectively decrease electrical contact resistance within the interconnection.

Based on the theory regarding the impact of series resistance on I-V curves mentioned in Subsection 2.4.1, Figure 6.4 clearly demonstrates that the prototype with the improved cell-bed exhibits a significantly lower series resistance compared to the prototype with the cell-bed featuring sliders. This difference is evident from the slope of the corresponding I-V curves near the V_{oc}.

Table 6.2: Performance parameters of prototypes consisting cell-bed based interconnections

Prototype	V_{oc} (V)	I_{sc} (A)	P_{max} (W)	Efficiency (%)	Fill-Factor (%)
Cell-Bed with sliders	1.379	5.94	5.64	18.46	68.88
Cell-Bed improved	1.385	5.90	6.33	20.68	78.54

Table 6.2 shows the I-V measurement based performance parameters for the prototypes.

Variations in V_{oc} are influenced by factors like temperature, illumination, doping concentration, saturation current, and recombination. I_{sc} depends on factors like optical properties, defects, recombination, and temperature [22].

The slider-based interconnection prototype has lower P_{max} due to increased series resistance, resulting in reduced efficiency and fill factor.

6.2.4 Cell-Bed based Interconnection Prototypes versus Reference Prototypes

Figure 6.5 depicts the I-V curves of the prototypes utilizing cell-bed based interconnections, as well as the I-V curves of the reference prototypes. Table 6.3 presents the derived performance parameters obtained from the I-V curves.

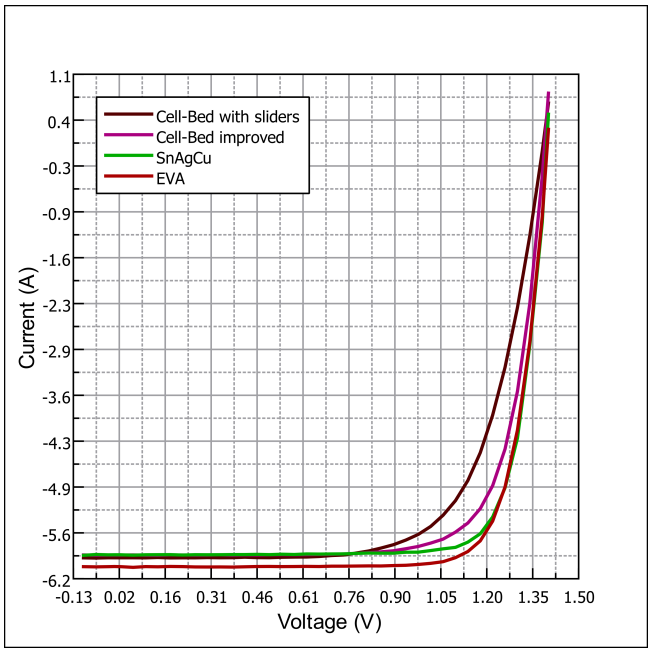

Figure 6.5: I-V curves of cell-bed based prototypes and reference prototypes

Table 6.3: Performance parameters of the cell-bed based prototypes and reference prototypes

Prototype	V_{oc} (V)	I_{sc} (A)	P_{max} (W)	Efficiency (%)	Fill-Factor (%)
Cell-Bed with sliders	1.379	5.94	5.64	18.46	68.88
Cell-Bed improved	1.385	5.90	6.33	20.68	78.54
SnAgCu	1.394	5.90	6.60	21.58	80.47
EVA	1.395	6.07	6.72	21.98	79.64

Observing the slopes of the I-V curves closer to the V_{oc} in Figure 6.5, it is evident that the cell-bed based prototypes exhibit higher series resistance in comparison to the reference prototypes.

In the cell-bed based prototypes, the presence of solder joints on the cell-dog-bone interface, along with the contact pressure-based mechanism for connecting the two dog-bones, introduces additional contact resistance, as discussed in Subsection 2.3.2. Conversely, the reference prototypes only incorporate solder joints on the dog-bone-cell interface, which reduces the contact resistance compared to the cell-bed based prototypes. A notable design difference between the two sets of prototypes is the interconnection length. The cell-bed prototypes use two dog-bones to connect two cells in series, while the reference prototypes use a single dog-bone for the same purpose. As a result, the interconnection wire length is longer in the cell-bed prototypes, leading to higher series resistance.

The higher series resistance observed in the cell-bed based prototypes, as depicted in Figure 6.5, leads to a reduction in the maximum power output, as indicated in Table 6.3. Consequently, the efficiency and fill-factor of the cell-bed prototypes are lower compared to the reference prototypes.

6.2.5 Magnetic Force based Interconnection Prototypes versus Reference Prototypes

Figure 6.6 illustrates the current-voltage (I-V) characteristics of the prototypes that employ magnetic contact pressure-based interconnections (Magnets Prototype) as described in Section 5.4, along with the I-V curves of the reference prototypes.

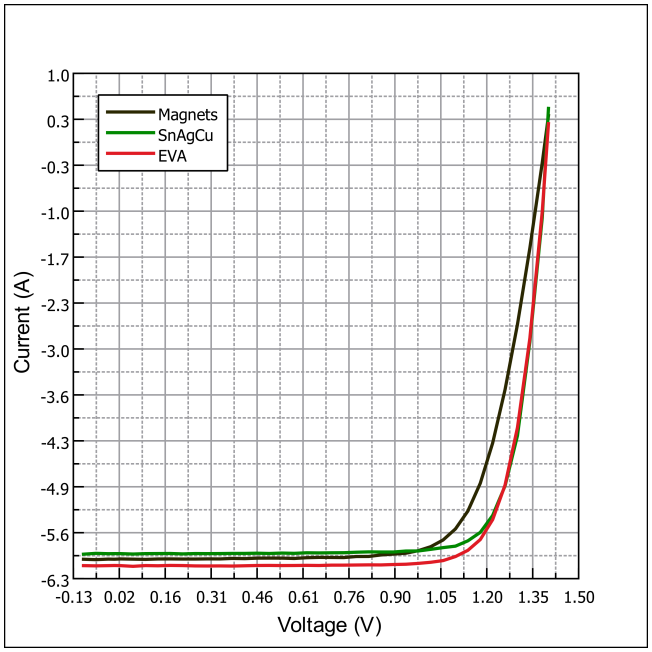

Figure 6.6: I-V curves of prototype consisting magnetic force based interconnection and reference prototypes

Figure 6.6 illustrates that the I-V curve of the prototype utilizing magnetic contact pressure-based interconnection demonstrates a steeper slope closer to the V_{oc} when compared to the reference prototypes. According to the theory discussed in Subsection 2.4.1, this observation suggests that the series resistance of the Magnets prototype is higher than that of the reference prototypes. This can be attributed to two factors. Firstly, the magnetic force-based interconnection involves two dog-bones instead of one, resulting in an increased length of the interconnection. Secondly, the introduction of electrical contact resistance occurs in the regions where the overlapping portions of the two dog-bones come into contact, along with the electrical resistance of the solder joints used to connect the two dog-bones to the solar cells.

Table 6.4: Performance parameters of the magnetic pressure contact based prototype and reference prototypes

Prototype	V_{oc} (V)	I_{sc} (A)	P_{max} (W)	Efficiency (%)	Fill-Factor (%)
Magnets	1.389	5.98	6.10	19.93	73.65
SnAgCu	1.394	5.90	6.60	21.58	80.47
EVA	1.395	6.07	6.72	21.98	79.64

Table 6.4 presents the performance parameters extracted from the I-V curves presented in Figure 6.6. The data reveals that the Magnets Prototype exhibits a higher short-circuit current in comparison to the SnAgCu prototype. It should be noted that the short-circuit current of a solar cell can be influenced by various factors, as discussed in the analysis of the I-V characteristics of the cell-bed based prototypes (6.2.3), in addition to the height elevation created by the magnets. Another aspect to consider is the potential light reflection from the top surface of the magnets. This light might be reflected onto the rear surface of the top glass and then, a fraction of it could be further reflected onto the solar cells. However, the extent to which light is reflected and the direction of such reflection are not explored within this thesis.

The increased series resistance leads to a voltage drop, resulting in reduced P_{max}. As a consequence, the Magnets prototype exhibits lower efficiency and fill-factor compared to the reference prototypes.

6.2.6 Prototype with Interconnection based on Soldering Two Dog-Bones to Each Other versus Reference Prototypes

Figure 6.7 depicts the I-V characteristics of the prototypes utilizing an interconnection method involving soldering of two dog-bones (referred to as the 2 Dog-bones soldered prototype) as described in Section 5.2, in addition to the I-V curves of the reference prototypes. Performance parameters obtained from the I-V curves are presented in Table 6.5.

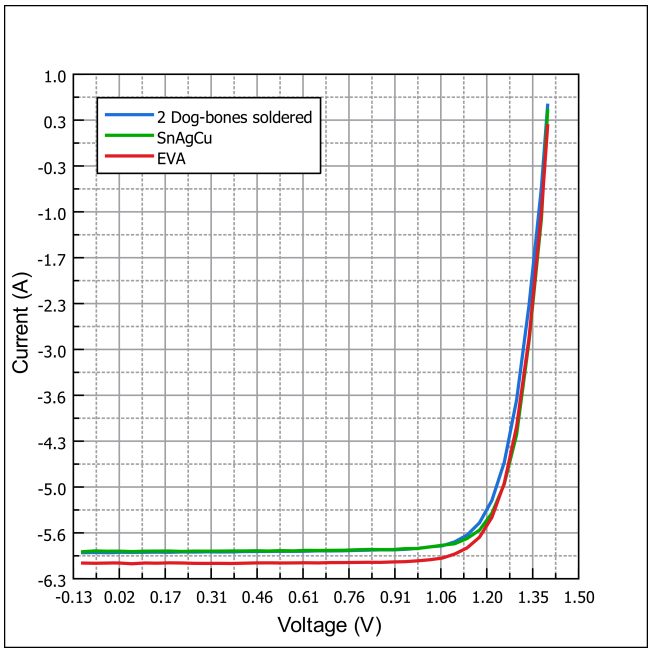

Figure 6.7: I-V curves of prototype consisting interconnection based on soldering two dog-bones and reference prototypes

Table 6.5: Performance parameters of the prototype consisting of interconnection based on soldering 2 dog-bones and reference prototypes

Prototype	V_{oc} (V)	I_{sc} (A)	P_{max} (W)	Efficiency (%)	Fill-Factor (%)
2 Dog-bones soldered	1.390	5.92	6.47	21.14	78.62
SnAgCu	1.394	5.90	6.60	21.58	80.47
EVA	1.395	6.07	6.72	21.98	79.64

Figure 6.7 illustrates that the I-V curve of the prototype utilizing interconnection through soldering two dog-bones displays a slightly steeper slope in its high-voltage region, in comparison to the I-V curves of the reference prototypes. This trend indicates an increase in series resistance, which can be attributed to two factors. Firstly, the interconnection in the 2 Dog-bones soldered prototype involves two dog-bones instead of one, resulting in an extended length of the interconnection. The cell-cell distance for the 2 Dog-bones soldered prototype is 0.92 cm, whereas the cell-cell distance for the reference prototypes is around 0.38 cm. Secondly, the manual process of melting tin coating to create the joint between the 2 Dog-bones may lead to non-uniform joints, potentially contributing to the higher series resistance.

The increased series resistance leads to a voltage drop and a decrease in the maximum power output, as indicated in Table 6.5. Consequently, the 2 Dog-bones soldered prototype exhibits lower efficiency and fill-factor compared to the reference prototypes.

The variations in V_{oc} and I_{sc} can be attributed to various factors as mentioned in the discussion of I-V characteristics of the cell-bed based prototypes in Subsection (6.2.3)

6.2.7 All the Prototypes Employing Two Dog-Bone based Interconnections.

Figure 6.8 illustrates the current-voltage (I-V) behavior of all the prototypes based on an interconnection method that involves two dog-bones. The performance metrics derived from these I-V curves are provided in Table 6.6.

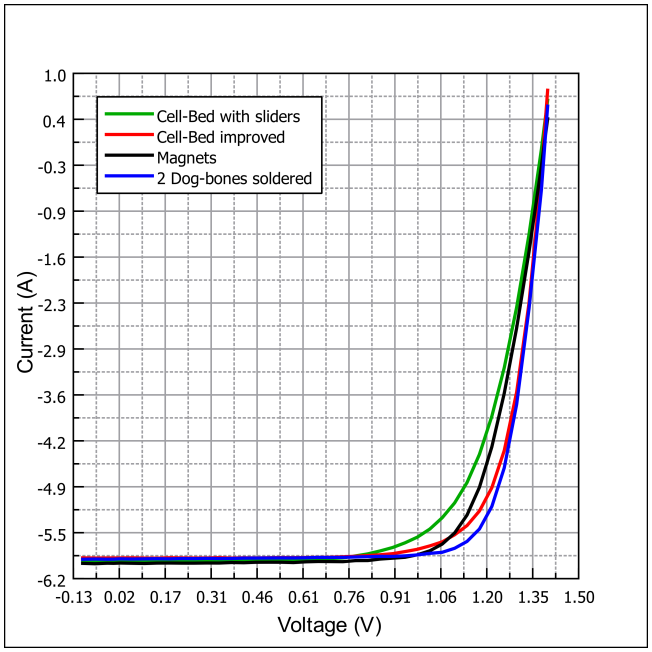

Figure 6.8: I-V curves of all prototypes consisting interconnection based on two dog-bones

Table 6.6: Performance parameters of the prototypes consisting interconnection based on two dog-bones

Prototype	V_{oc} (V)	I_{sc} (A)	P_{max} (W)	Efficiency (%)	Fill-Factor (%)
Cell-Bed with sliders	1.379	5.94	5.64	18.46	68.88
Cell-Bed improved	1.385	5.90	6.33	20.68	78.54
Magnets	1.389	5.98	6.10	19.93	73.65
2 Dog-bones soldered	1.390	5.92	6.47	21.14	78.62

Figure 6.8 illustrates the variations in series resistance among prototypes using interconnection with two dog-bones. The Cell-bed with sliders prototype exhibits the highest series resistance, followed by the prototypes using magnetic force-based contact pressure interconnection, which has lower series resistance compared to the cell-bed with sliders prototype. The Cell-bed improved prototype shows lower series resistance compared to the magnetic force-based contact pressure interconnection prototype, while the 2 dog-bones soldered prototype displays the lowest series resistance. Despite the enhanced contact pressure in the Magnets prototype, it exhibits higher series resistance. This is primarily attributed to its longer interconnection length and smaller overlapping contact area between the dog-bones, which mirrors the conditions of the Cell-bed with sliders prototype (cell-cell distance = 1.1 cm and overlapping contact area = 36 mm^2). On the contrary, the Cell-bed improved prototype achieves a 50% increase in overlapping contact area of the dog-bones by reducing the cell-cell distance to 0.8 cm. However, the Magnets prototype encounters limitations due to the powerful magnetic force, which has the potential to damage the cell edges when attempts are made to reduce the interconnection length. The 2 dog-bones soldered prototype achieves the lowest series resistance, likely because it enhances the contact area between the overlapping regions by melting the contact regions, rather than solely pressing them against each other as done in the prototypes based on contact pressure based interconnection mechanisms. The maximum power output (P_{max}) delivered by the prototype, efficiency and fill-factor are inversely proportional to the series resistance. This can be observed by comparing Figure 6.8 and Table 6.6.

6.2.8 Prototype with SnBi based Interconnection versus Reference Prototypes.

Figure 6.9 depicts the current-voltage (I-V) characteristics of the SnBi prototype, which utilizes a soldered single dog-bone interconnection method with the SnBi solder alloy, alongside the reference prototypes.

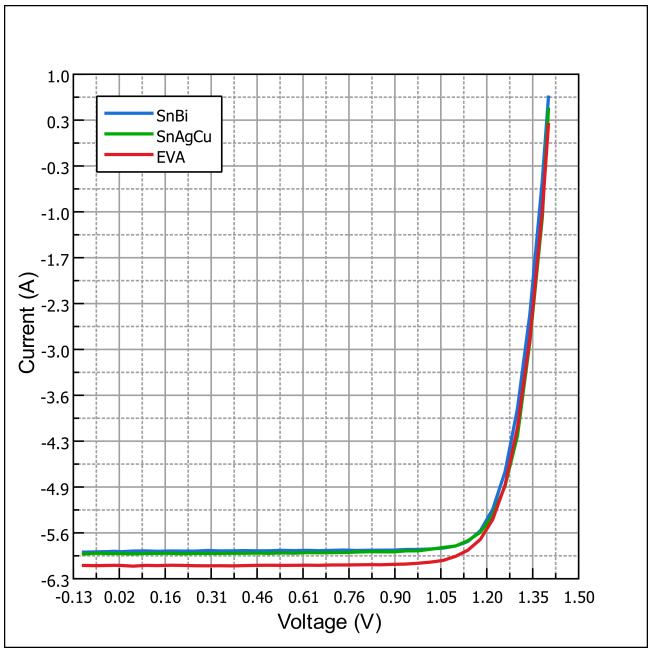

Figure 6.9: I-V curves of prototype consisting interconnection based on SnBi solder alloy and reference prototypes

As mentioned in Subsections 2.3.1 and 2.3.2 the series resistance in solder joints is influenced by two main factors: electrical contact resistance, determined by the joint structure and the impact of irregularities on current flow, and the solder alloy material, as its electrical resistivity is a material property.

Although Figure 6.9 does not clearly indicate higher series resistance in the SnBi prototype compared to the SnAgCu reference prototypes based on the slope of it's I-V curve close to the V_{oc}, the higher electrical resistivity of SnBi solder alloy (34.5 $\mu\Omega$·cm [91]) compared to that of the SnAgCu solder alloy (12.5 $\mu\Omega$·cm [53]) suggests a potential for increased series resistance.

To gain further clarity on the series resistance, a relative measure was calculated.
To determine the relative series resistance (*Rs*), the slope of the voltage and current near the V_{oc} (open circuit voltage) in an I-V curve can be used, as illustrated in Figure 6.10.

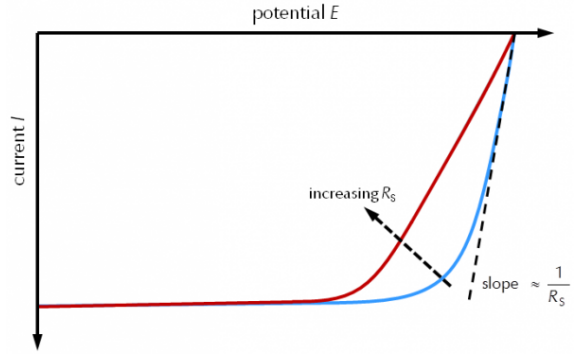

Figure 6.10: The impact of the series resistance RS on the shape of an I-V curve [92]

The calculation of R_s for analyzing the performance of the prototypes involved utilizing the following formula [93] :

$$R_s = \frac{V_1 - V_2}{I_1 - I_2} \tag{6.2}$$

Where, V_1 and V_2 represent voltage measurements taken in close proximity to V_{oc}, while I_1 and I_2 represent the corresponding current values measured at V_1 and V_2. To improve precision, four data points near V_{oc} were chosen instead of two.

Table 6.7: Performance parameters of the prototype consisting of interconnection based on SnBi solder alloy and reference prototypes

Prototype	V_{oc} (V)	I_{sc} (A)	P_{max} (W)	Rs (milli-Ohms)	Efficiency (%)	Fill-Factor (%)
SnBi	1.389	5.87	6.58	23.59	21.50	80.7
SnAgCu	1.394	5.90	6.60	21.77	21.58	80.47
EVA	1.395	6.07	6.72	21.26	21.98	79.64

Table 6.7 showcases the performance metrics and the calculated values for relative series resistance obtained from analyzing the I-V curves of both the SnBi prototype and the reference prototypes.
The data presented in Table 6.7 clearly shows that the SnBi prototype exhibits a higher resistance compared to the reference prototypes. Specifically, the SnBi prototype has the highest series resistance and the lowest P_{max}, while the SnAgCu prototype has a lower series resistance and a higher P_{max}.

The EVA prototype, which uses the same solder alloy as the SnAgCu prototype (SnAgCu solder), demonstrates the lowest series resistance and the highest P_{max}. The difference in series resistance between the EVA and SnAgCu prototypes is not substantial, but the EVA prototype has a higher P_{max}, likely due to better current generation and more uniform solder joints. The SnBi prototype has a slightly lower maximum current (I_{max}) of 5.57 A compared to the SnAgCu prototype (5.59 A) and the EVA prototype (5.70 A). However, the maximum voltage (V_{max}) remains the same (1.18 V) for all prototypes. This indicates that the lower P_{max} of the SnBi prototype can also be due to reduced current collection or current generation capability.

The efficiency of a PV module is directly related to its P_{max}, as observed in Table 6.7. The fill-factor does not follow a similar trend, with the SnBi prototype having the highest fill-factor, followed by the SnAgCu prototype, and then the EVA prototype. This pattern is influenced by the measured values of V_{oc} and I_{sc}, where the SnBi prototype has lower values than the SnAgCu prototype, and the SnAgCu prototype has lower values than the EVA prototype.

6.2.9 Analysis of Series Resistance, Power Output, and Efficiency for All Prototypes.

Table 6.8 showcases the calculated relative series resistance measurements using Equation 6.2, along with the measured maximum power output (P_{max}) and conversion efficiency, for all the prototypes, obtained through analysis of their I-V curves. As per the datasheet, the rated efficiency of the solar cell is 22.7% and the rated maximum power output is 3.48 W [54].

Table 6.8: Calculated series resistance, efficiency, and measured maximum power output for all prototypes

Prototype	Rs (milli-Ohms)	P_{max} (W)	Efficiency (%)
Cell-bed with sliders	41.28	5.64	18.43
Cell-bed improved	26.09	6.33	20.68
Magnets	34.58	6.10	19.94
2 Dog-bones soldered	24.69	6.48	21.17
SnBi	23.59	6.58	21.50
SnAgCu	21.77	6.60	21.58
EVA	21.21	6.73	21.98

From Table 6.8, the results indicate that the prototype employing Cell-Bed with sliders exhibits the highest series resistance, followed by the prototype utilizing magnetic-force based contact pressure

interconnections. The prototype with the improved Cell-Bed shows lower series resistance, while the prototype featuring interconnections based on soldering 2 dog-bones exhibits the lowest series resistance among all the prototypes employing two dog-bones. The lowest series resistance and the highest power output is delivered by the SnBi prototype compared to all the prototypes except the reference ones.

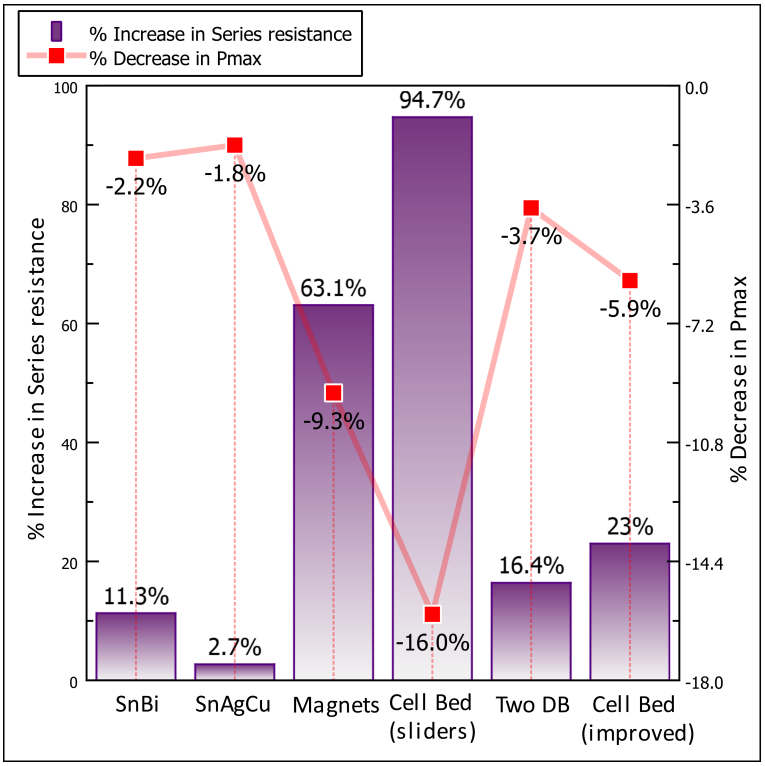

Figure 6.11: Percentage increase in series resistance and Percentage P_{max} decrease with respect to EVA prototype

Figure 6.11 shows the percentage increase in Series resistance and the percentage decrease in P_{max} for the prototypes compared to the reference EVA prototype. The percentage increase in series resistance is determined by subtracting the series resistance of the specific prototype from that of the EVA prototype and then dividing the result by the series resistance of the EVA prototype. Similarly, the percentage decrease in P_{max} is calculated.

It is clear from this Figure that the drop in P_{max} increases with increasing series resistance.
The SnAgCu prototype has a minimal increase (2.7%) in series resistance likely due to its similarity in solder alloy and interconnection mechanism with the EVA prototype and has the lowest drop in P_{max} (-1.8%). The SnBi prototype has the second lowest increase (11.3%) in series resistance and the second lowest decrease in P_{max} (-2.2%) compared to the EVA prototype. The prototype employing interconnection based on soldering the overlapping contact regions between two dog-bones (referred to as Two DB in the graph) exhibits a slightly higher series resistance (16.4%) and decrease in P_{max} (-3.7%). The improved cell-bed-based interconnection prototype shows a higher increase (23%) in series resistance and a higher decrease in P_{max} (-5.9%).
The prototypes using magnetic force-based interconnection and cell-bed with slider-based interconnection show the highest increases in series resistance, reaching 63.1% and 94.7%, respectively. Consequently, they also experience the highest drops in P_{max} (-9.3% and -16%, respectively) compared to the EVA prototype.

6.3 Thermal Cycle Test

As mentioned in section 4.4, it is vital to conduct thermal cycle tests to assess the performance of different interconnection mechanisms in the prototypes.

It is crucial to consider potential degradation mechanisms that may affect the prototypes during thermal cycling. As described in section 3.1.3, one area of concern involves the potential damage to solder joints caused by thermal expansion and contraction. Furthermore, since all the prototypes except the EVA prototype lack lamination and follow the structure of the Biosphere Solar PV module, there is only air between the glass and the solar cells. Consequently, the cells lack any physical support, making them more susceptible to warping and bending, which can lead to structural damage. This warping of cells can also adversely affect the optical texturing on the cells, thereby impacting overall performance.

An important factor to consider is that, with the exception of the EVA prototype, all other prototypes solely depend on desiccant sachets and powder to absorb moisture. In the absence of a certification confirming the absence of moisture or humidity inside the prototypes, there is a risk of cell degradation due to exposure to high humidity. This could adversely affect the performance and reliability of the solar cells in the prototypes.

For these tests, all prototypes except the one using a cell-bed with slider-based interconnection mechanism were chosen, including the reference prototypes. The reason for excluding the cell-bed with sliders prototype was its remarkably low efficiency (18%), and the fact that both the cell-bed and sliders were made of PLA, which has a glass transition temperature of 55°C, which can lead to deformation of the structure when the thermal cycle reaches temperatures above the glass transition temperature.

6.3.1 Testing Strategy

Originally, the intention was to conduct fifty thermal cycles for various reasons. Firstly, there was uncertainty regarding the availability of the climate chamber. Secondly, most of the prototypes had unique structures and did not contain EVA, making it challenging to predict whether the edge seal, solar cells, and supporting structures would withstand 50 cycles without experiencing substantial damage.

After completing 50 cycles, all prototypes with the Biosphere Solar PV module configuration remained intact without any damage. Therefore, it was decided to remove the prototypes from the chamber after an additional 30 cycles and evaluate their condition based on observations. If visible moisture ingress, breakage of cell-supporting structures, breakage of solar cells, or any damage compromising the measurements was detected in any of the prototypes, the thermal cycle test would be concluded immediately. On the other hand, if no such damage was found, the same procedure of conducting an additional 30 cycles would be repeated until a total of 200 cycles were completed. Eventually, the prototypes underwent a total of 200 thermal cycles.

To evaluate the impact of thermal cycles on the performance of the prototypes, I-V measurements and EL images were captured at specific intervals between the thermal cycles. As mentioned previously, first interval was after 50 thermal cycles (TC 50), and the rest of the intervals were planned with the difference of 30 thermal cycles between each of them such that the intervals are at TC 50, TC 80, TC 110, TC 140, TC 170 and TC 200.

The climate chamber in the ESP lab at TU Delft was used to conduct the thermal cycles. The I-V measurements were carried out in the ESP lab using the setup described in Section 6.1, while the EL images were captured at the Biosphere Solar workspace.

6.3.2 Climate Chamber

The climate chamber at ESP lab encompasses several functional aspects that need to be addressed. It is necessary to program the thermal cycles with specific steps, where the program concludes after the final step without the option of repetition.

The ramp rate setting of the chamber was non-functional, resulting in a fixed ramp up rate of 133°C per hour. This value exceeds the recommended limit of less than 100°C per hour stipulated by the IEC standards, as mentioned in Section 4.4.

Furthermore, the auto-drain function, designed to maintain relative humidity at zero percent, was nonfunctional. As a result, the humidity level could not be sustained at zero; instead, it fluctuated between 40% and 95% with changes in temperature ranging from -40°C to 85°C.

Despite these limitations, the tests proceeded, as accelerated thermal tests hold potential for assessing the durability of innovative interconnection mechanisms and novel module concepts [94].

Figure 6.12 illustrates the trend lines depicting the thermal cycles and the fluctuations in relative humidity.

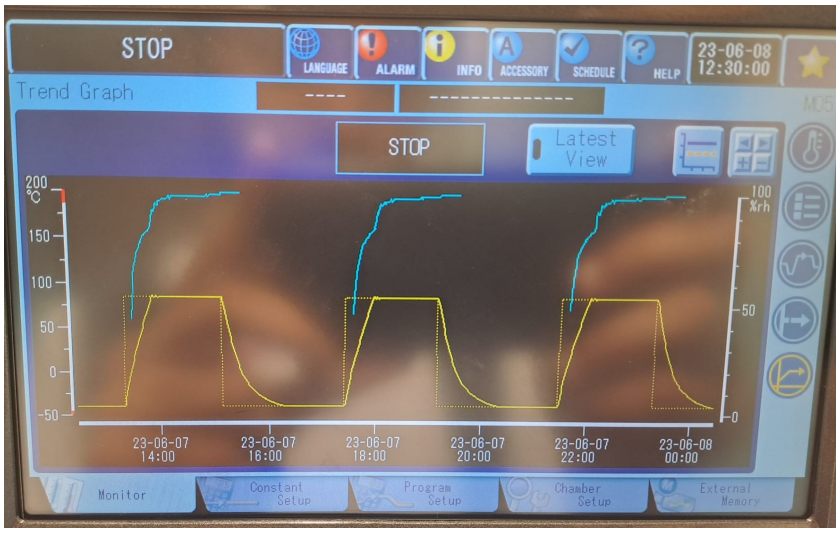

Figure 6.12: Trend lines depicting the thermal cycles (yellow, left y-axis) and change in relative humidity (blue, right y-axis)

Based on the Figure, it can be observed that the dwell time for each cycle is approximately 40 minutes, which adheres to the IEC standards' recommendation of a minimum of 10 minutes.

6.3.3 Changes in I-V Measurement Equipment

It is important to note that the Enlitech lamp and the cabling used in the I-V measurement setup underwent multiple modifications prior to the thermal cycle tests due to technical errors like misalignment of internal mirrors in the lamp, damaged cables, and connectors. The adjustments made to address these issues have the potential to introduce additional errors and result in measurement inaccuracies.

Before conducting the I-V measurements during the TC 50 interval, the illumination intensity was calibrated based on the short circuit current of a bare IBC solar cell to achieve more accuracy in the measurements.

6.4 Outcomes of Thermal Cycle Tests

This section provides an analysis of visual observations, electrical performance, and EL images captured at specific intervals during the 200 thermal cycles. TC 0 represents the initial instance before commencing the thermal cycle test. Additionally, the thermal cycle test process flow explained in Subsection 6.3.1 was modified at TC 110 due to laboratory maintenance. Consequently, the I-V measurements and EL images could not be taken after 110 cycles, and they were instead recorded after 115 cycles.

6.4.1 SnBi Prototype

The SnBi prototype exhibited minimal visual observations, with only minor solar cell warping and bending being observed. Figure 6.13 displays the EL images of SnBi prototype captured before the thermal cycle test and at specific intervals while conducting the thermal cycle test.

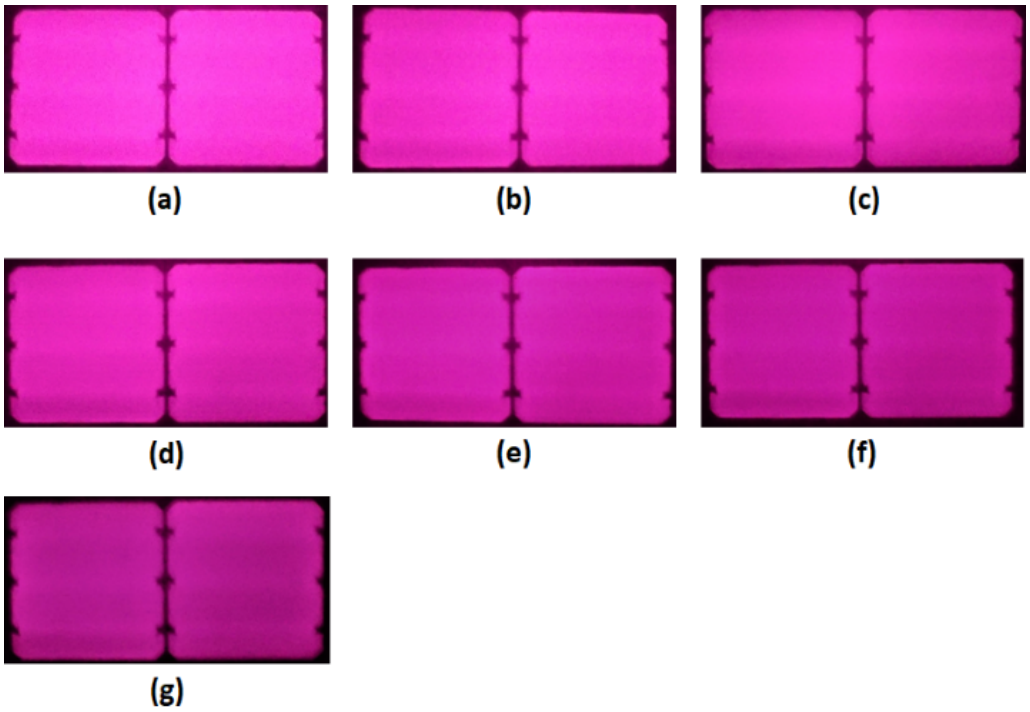

Figure 6.13: EL images of the SnBi prototype at (a) TC 0 (b) TC 50, (c) TC 80, (d) TC 115, (e) TC 140, (f) TC 170 and (g) TC 200

Figure 6.13 demonstrates that the light intensity in the EL images diminishes as the number of thermal cycles increases. After 115 thermal cycles, a slightly darkened region can be observed in the lower area of the left-side cell. These observations can potentially be attributed to the factors mentioned in Section 6.3 such as warping of the solar cells and reasons such as material defects mentioned in Section 4.1 along with potential degradation of the solder joints causing an increase in series resistance.

Table 6.9: Performance characteristics exhibited by the SnBi prototype at distinct time intervals during the Thermal cycle test

Thermal Cycles	0	50	80	115	140	170	200
SnBi P_{max} (W)	6.58	6.47	6.34	6.32	6.31	6.28	6.17
I_{sc} (A)	5.87	5.80	5.76	5.75	5.74	5.71	5.63
V_{oc} (V)	1.389	1.385	1.389	1.387	1.385	1.384	1.385

Table 6.9 presents the variations in performance parameters acquired via I-V measurements for the SnBi prototype at specific intervals during the thermal cycle test. The data clearly demonstrates a gradual decrease in power output as the number of cycles progresses. Additionally, a significant decline in I_{sc}

is observed. This outcome can be attributed to various factors, such as material degradation due to warping, damage of cell's optical texturing caused by warping, and non-uniform illumination during I-V measurements resulting from minor warping of the solar cells, which did not show retention or recovery of shape after the prototype was kept at room-temperature. Despite these fluctuations, the V_{oc} remains relatively consistent, with only a minor decrease noticed towards the conclusion of the 200 thermal cycles.

6.4.2 Prototype with Two Dog-bones Soldered to Each Other

As explained in section 5.2, the 2 Dog-bones soldered prototype utilizes an interconnection mechanism where two dog-bones are soldered to two solar cells, and they are interconnected in series by melting the tin coating between the overlapping contact regions of the two dog-bones to establish a connection.

Throughout the thermal cycle test, the 2 Dog-bones soldered prototype displayed visual changes within the PV module, notably minor warping. After 115 cycles, one of the spacers became detached from the glass, as illustrated in Figure 6.14a. During the prototyping phase, the spacer was affixed to the glass using commercial superglue, the only available option at that time. The detachment may have been caused by thermal cycling or improper gluing. Despite its small size, the spacer has the potential to obstruct incident light on the solar cells, which could impact performance. Additionally, its rough wooden material can cause damage to the texturing on the solar cells.

After 140 cycles, one of the molten joints connecting the contact regions became dislodged, resulting in the contact regions to no longer being connected (as illustrated in Figure 6.14b). This occurrence can be attributed to thermal expansion and contraction of the dog-bones, as well as the insufficiency of the molten joint's surface area to create a robust bond that adheres to the contact region surfaces.

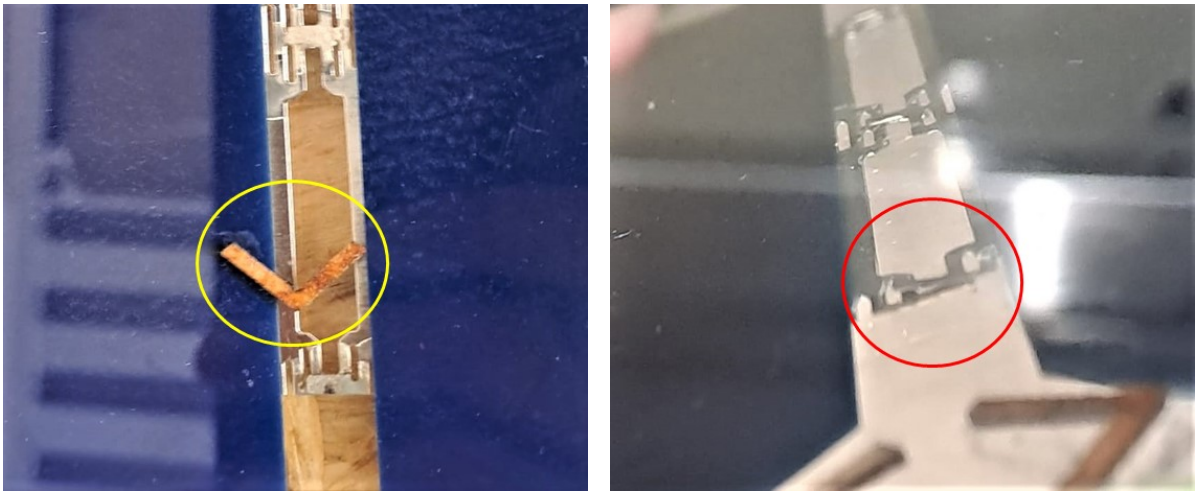

(a) **(b)**

Figure 6.14: (a) Displaced spacer in 2 Dog-bones soldered prototype after 115 thermal cycles, and (b) Broken connection between contact regions after 140 thermal cycles

The disrupted connection between the two contact regions illustrated in Figure 6.14b can lead to an elevation in series resistance as the flow of current is obstructed. This has the potential to affect the electrical performance of the prototype.

Figure 6.15 displays the EL images of 2 Dog-bones soldered prototype captured before the thermal cycle tests and at the specific intervals while conducting the thermal cycle tests.

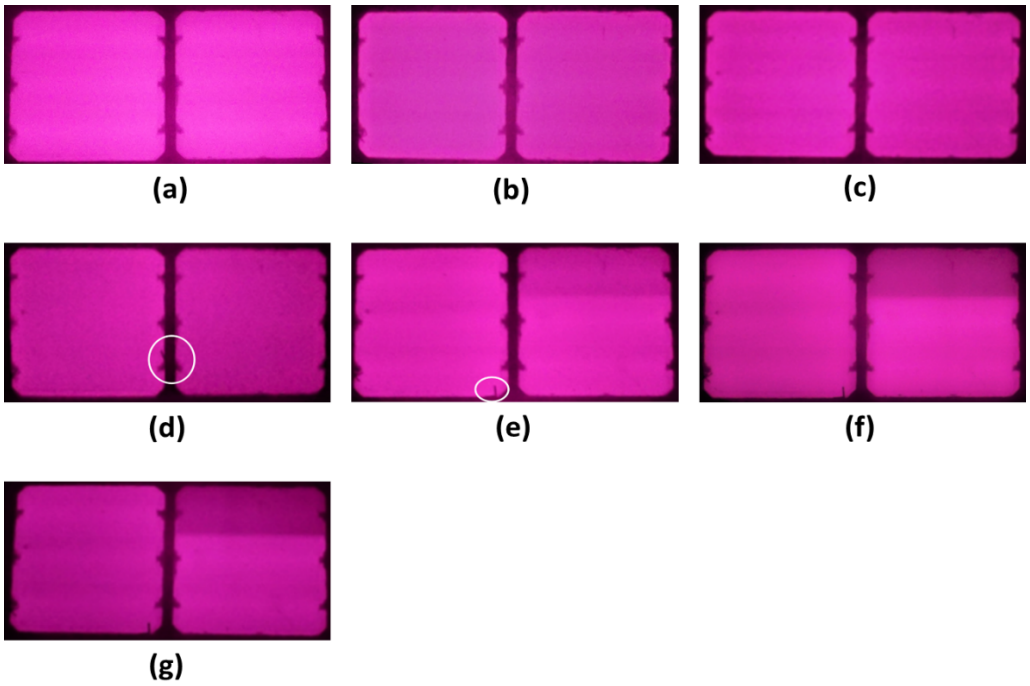

Figure 6.15: EL images of the 2 Dog-bones soldered prototype at (a) TC 0 (b) TC 50, (c) TC 80, (d) TC 115, (e) TC 140, (f) TC 170 and (g) TC 200

In Figure 6.15, the highlighted region in subfigure (d) reveals a displaced spacer seen in the EL image after TC 115, The highlighted area in subfigure (e) indicates the shifted position of the displaced spacer towards the bottom side of the left-sided solar cell after TC 140.

The EL images depicted in Figure 6.15 show a dark region on the top side of the right-sided solar cell, which becomes increasingly prominent after 140 cycles. This dark region corresponds to the area neighboring the broken contact region depicted in Figure 6.14b.

The appearance of the dark region can be attributed to the reduced current flow caused by the broken contact. The deepening darkness in this region can be attributed to the reasons such as reduced shunt resistance and material degradation mentioned in Sections 6.3 and 4.1 along with structural damage or cracks in the solder joints resulting from the warping of the solar cells.

Table 6.10: Performance characteristics exhibited by the 2 Dog-bones soldered prototype at distinct time intervals during the Thermal cycle test

Thermal Cycles	0	50	80	115	140	170	200
2 Dog-bones soldered P_{max} (W)	6.48	6.38	6.36	6.27	6.21	6.18	6.17
I_{sc} (A)	5.92	5.78	5.78	5.73	5.70	5.70	5.71
V_{oc} (V)	1.397	1.390	1.395	1.398	1.389	1.391	1.390

Table 6.10 presents the changes in performance parameters obtained through I-V measurements for the 2 Dog-bones soldered prototype at specific intervals during the thermal cycle test. The data clearly shows a gradual reduction in power output as the number of cycles increases. Moreover, a significant decrease in I_{sc} is observed. These outcomes can be attributed to the factors mentioned in Section 6.3 such as the warping of solar cells and reasons such as material degradation mentioned in Section 4.1, along with the broken connection between the two contact regions and the displacement of the spacer. Despite these fluctuations, the V_{oc} remains relatively consistent.

6.4.3 Prototype with Improved Cell-Bed

As described in section 5.3, the original interconnection design using the cell-bed with sliders had some drawbacks. To address these issues, adjustments were made to the cell-bed design, resulting in the creation of a prototype called the Cell-Bed improved prototype (depicted in Figure 5.12a).

In this prototype, the polymer material of the cell-bed was changed from PETG to ABS due to its higher glass transition temperature (Tg = 100°C). Additionally, out of the three contact strips, one was intentionally made from PETG (Tg = 85°C). The purpose of using PETG was to examine whether the strip's physical structure would undergo changes during the thermal cycle test and if it would have any impact on the interconnection. The PETG exhibited a notable increase in deformation after TC 115, as depicted in Figure 6.16a. Following 200 cycles, the left-sided solar cell and its connected dog-bone shifted towards the left side, resulting in a noticeable increase in the gap between adjacent cells, as observed in Figure 6.16b. These alterations seem to be attributed to the thermal cycles, which induced various effects including the warping of the PETG strip, possible structural changes or loosening of the screws leading to reduced contact pressure, and warping of the solar cells.

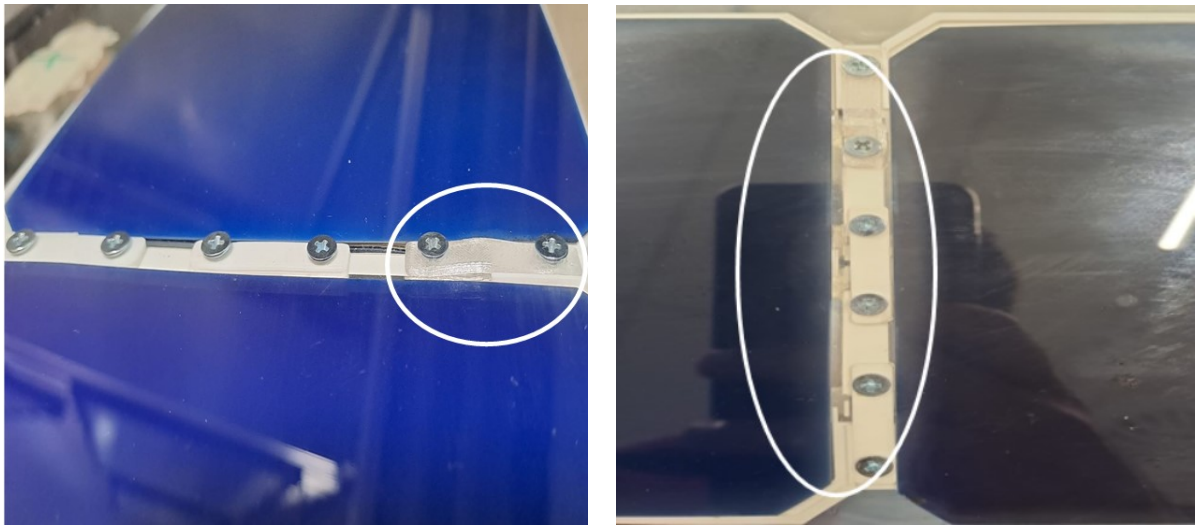

(a) (b)

Figure 6.16: (a) Deformed PETG strip (highlighted in white circle) after 115 cycles, and (b) Increased cell-cell distance due to displacement of dog-bone and solar cell noticed after 200 cycles (highlighted in white circle)

Moreover, from TC 80 onwards, the prototype displayed significant warping of the solar cells (as shown in Figure 6.17. This warping has the potential to damage the solder joints and lead to structural changes within the solar cell itself. This warping could be attributed to the cell-bed holding the cell tightly and the increased glass-glass height compared to the SnBi prototype. It is important to note that the warping did not lead to the solar cells touching the glass. Additionally, the solar cells did not show retention or recovery of their original shape after being kept at room temperature.

Figure 6.17: Warping of solar cell in the Cell-bed improved prototype

The deformation of the PETG strips diminishes the physical pressure applied on the contact regions connecting the two dog-bones. As a consequence, this can lead to non-uniform or reduced electrical contact, ultimately causing an increase in electrical contact resistance, which negatively impacts the electrical performance.

Furthermore, the increase in cell-cell distance counters the original design intent of the improved cell-bed design, which aimed to decrease the cell-cell distance and increase the percentage area of overlapping regions between the dog-bones to reduce electrical resistance.

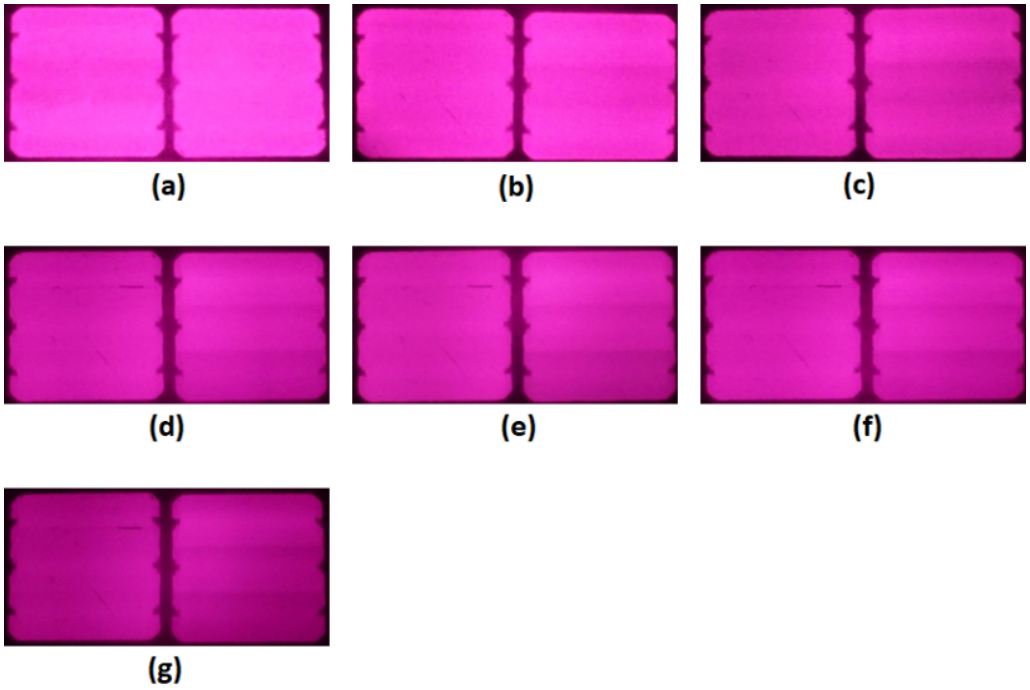

Figure 6.18: EL images of the Cell-Bed improved prototype at (a) TC 0 (b) TC 50, (c) TC 80, (d) TC 115, (e) TC 140, (f) TC 170 and (g) TC 200

Figure 6.18 presents the EL images of the Cell-Bed improved prototype captured before the thermal cycle test and at specific intervals during the test. These images clearly demonstrate that the light intensity in the EL images diminishes as the number of thermal cycles increases. This phenomenon can be attributed to the potential consequences of thermal cycling such as warping mentioned in Section 6.3 along with reasons such as reduced shunt resistance described in Section 4.1, increased series resistance due to solder joint damage, and disrupted contact between the overlapping regions of the two dog-bones.

Furthermore, the EL images present specific observations. Firstly, the central region of the right-sided solar cell displays a slight decrease in illumination intensity after TC 50 and TC 80. Secondly, from TC 115 onwards, a crack becomes apparent in the top section of the left-sided solar cell. This crack is a result of extensive warping of the solar cell during the thermal cycles. Thirdly, a darkened region in the bottom part of the right-sided solar cell is associated with the contact region overlapped with the PETG strip, which exhibits significant deformation starting from TC 115. The darkened region in the bottom part of the right-sided solar cell can be attributed to increased series resistance caused by reduced contact pressure due to the deformation of the PETG strip along with the reasons mentioned for the decrease in overall illumination intensity. Notably, this region shows a lesser reduction in light intensity compared to the darkened region shown in Figure 6.15, corresponding to the loosened contact region in the 2 Dog-bones soldered prototype. One potential explanation for this difference is that the loosened contact observed in the 2 Dog-bones soldered prototype shows the contact regions to move away from each other, whereas in the cell-bed improved prototype, the contact regions remain in contact with each other while the PETG strip deforms.

Table 6.11: Performance characteristics exhibited by the Cell-Bed improved prototype at distinct time intervals during the Thermal cycle test

Thermal Cycles	0	50	80	115	140	170	200
Cell-Bed improved P_{max} (W)	6.20	6.18	6.14	6.08	6.06	6.04	5.97
I_{sc} (A)	5.90	5.88	5.78	5.84	5.78	5.80	5.81
V_{oc} (V)	1.385	1.383	1.385	1.386	1.385	1.393	1.386

Table 6.11 displays the performance parameters obtained from I-V measurements at specific intervals during the thermal cycle test. It is evident from this table that the maximum power output (P_{max}) decreases as the number of thermal cycles increases. This decrease can be linked to the factors mentioned earlier, which also affected the changes observed in the EL images of the Cell-Bed improved prototype. During the measurements, the I_{sc} values exhibited variations. It is essential to note that the considerable warping of the solar cells during the thermal cycle test could lead to non-uniform illumination, thereby impacting the accuracy of the I-V measurements. The V_{oc} values showed minimal variation.

6.4.4 Magnets Prototype

As explained in Section 5.4, the Magnets prototype features an interconnection mechanism based on magnetic force for contact pressure.

Throughout the thermal cycle test, the most noticeable observation for the Magnets prototype was the bending of solar cells. This prototype exhibited the highest degree of warping. In this case, the warping also lead to occasional touching of the solar cells and the front glass, which could potentially damage the solar cells. As observed for the previously mentioned prototypes, the solar cells did not retain their original shape after being kept at room temperature.
Figure 6.19 showcases the warping of a solar cell in the Magnets prototype.

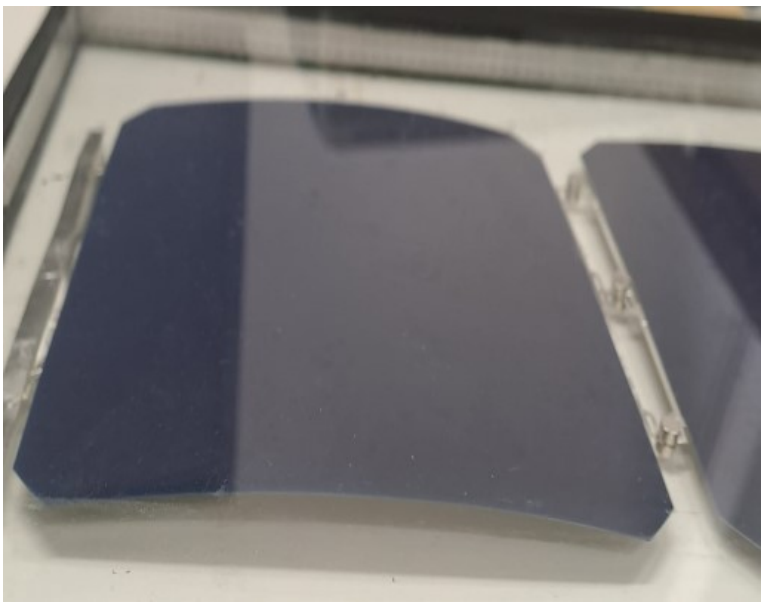

Figure 6.19: Warping of solar cell in Magnets prototype

As mentioned in the previous explanations, the warping of solar cells can have detrimental effects on both the solar cells themselves and the solder joints in interconnections.

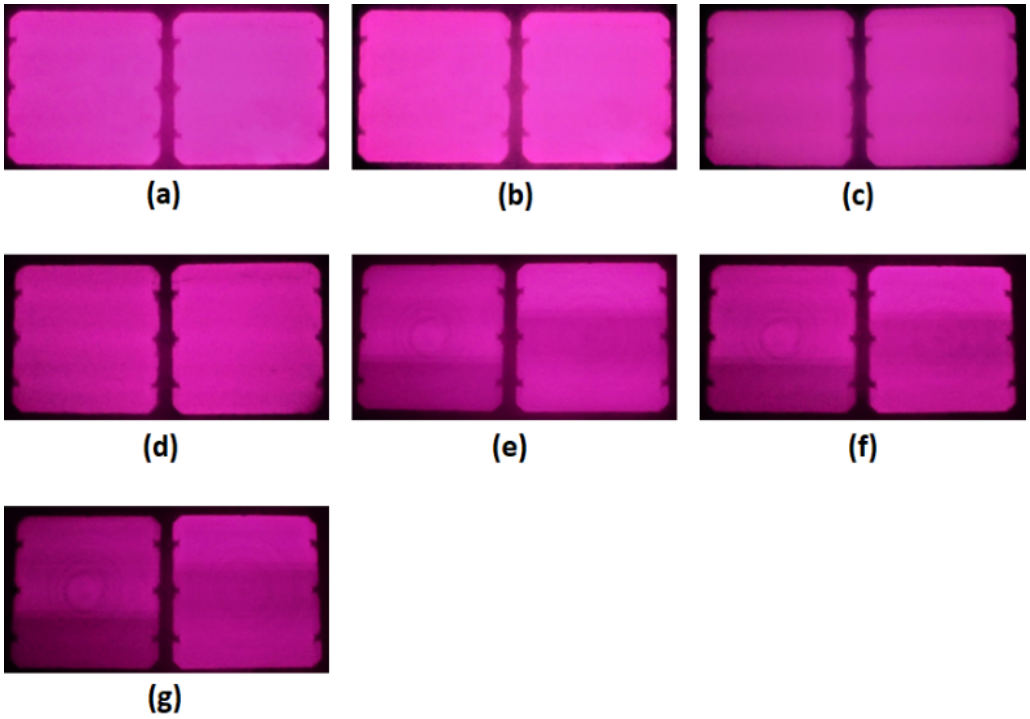

Figure 6.20: EL images of the Magnets prototype at (a) TC 0 (b) TC 50, (c) TC 80, (d) TC 115, (e) TC 140, (f) TC 170 and (g) TC 200

Figure 6.20 presents the EL images of the Magnets prototype captured before the thermal cycle test and at specific intervals during the test. Based on this Figure, it is evident that the illumination intensity decreases progressively with an increase in the number of thermal cycles which can be due to the potential reasons such as warping of solar cells due to thermal cycling mentioned in Section 6.3 and degradation of solar cell material as mentioned in Section 4.1.

Specific observations can be drawn from this image. Firstly, beginning at TC 140, lower illumination intensity patches are evident in the bottom area of the left-sided solar cell and the middle section of the right-sided solar cell. These occurrences could be attributed to several factors, including structural changes, series resistance in interconnections due to thermal stress on magnets. The reduction in the magnetic strength of the magnets could result from thermal cycles, as noted in Subsection 3.4.3, given that the chosen neodymium magnets have an operational temperature limit of 80°C. Additional factors include series resistance resulting from solder joint damage which can arise from thermal cycling. Secondly, a radial pattern becomes noticeable in the central region of both solar cells. This pattern could be arising due to the excessive warping of the solar cells causing changes in the material of the solar cells.

Table 6.12: Performance characteristics exhibited by the Magnets prototype at distinct time intervals during the Thermal cycle test

Thermal Cycles	0	50	80	115	140	170	200
Magnets P_{max} (W)	6.10	6.07	6.06	6.04	5.95	5.91	5.88
I_{sc} (A)	5.98	5.98	5.76	5.83	5.75	5.74	5.74
V_{oc} (V)	1.389	1.375	1.349	1.344	1.337	1.318	1.305

Table 6.12 reveals a notable decrease in the maximum power output (P_{max}) of the Magnets prototype as the number of thermal cycles increases. This decline can be linked to the aforementioned reasons that account for changes in EL images. In addition, significant variations in the I_{sc} are observed, with a decrease in values towards the end of 200 thermal cycles, along with a decrease in V_{oc} as the number of thermal cycles increases. Besides the factors mentioned earlier, such as structural changes due to thermal

stress, increased series resistance, and decreased shunt resistance, another potential contributing factor to this trend could be an increase in surface recombination [95]. A potential reason for this increase in surface recombination could be the damage of passivation layers caused due to the warping of solar cells.

6.4.5 SnAgCu Prototype

As discussed in Section 5.5, the SnAgCu prototype was developed as a standard reference, following the Biosphere Module PV structure with the standard SnAgCu solder alloy.

During the thermal cycle test, the SnAgCu prototype demonstrated minimal solar cell warping. However, a notable visual observation at TC 25 was the displacement of the bottom spacer. This displacement was caused by the super-glue's loss of adhesion to the back glass during the thermal cycles. Consequently, the spacer moved upwards and partly went beneath a solar cell, likely due to the combination of the superglue losing its adhesive properties and the solar cell warping.
After TC 33, the spacer was once again displaced and moved away from the cells, eventually becoming lodged against the internal side of the PIB edge seal. Figure 6.21 visually illustrates these observations. It's important to note that these observations were recorded at TC 25 and TC 33 because the thermal cycle program needed to be restarted, since it did not repeat after ending (as mentioned in Subsection 6.3.2).

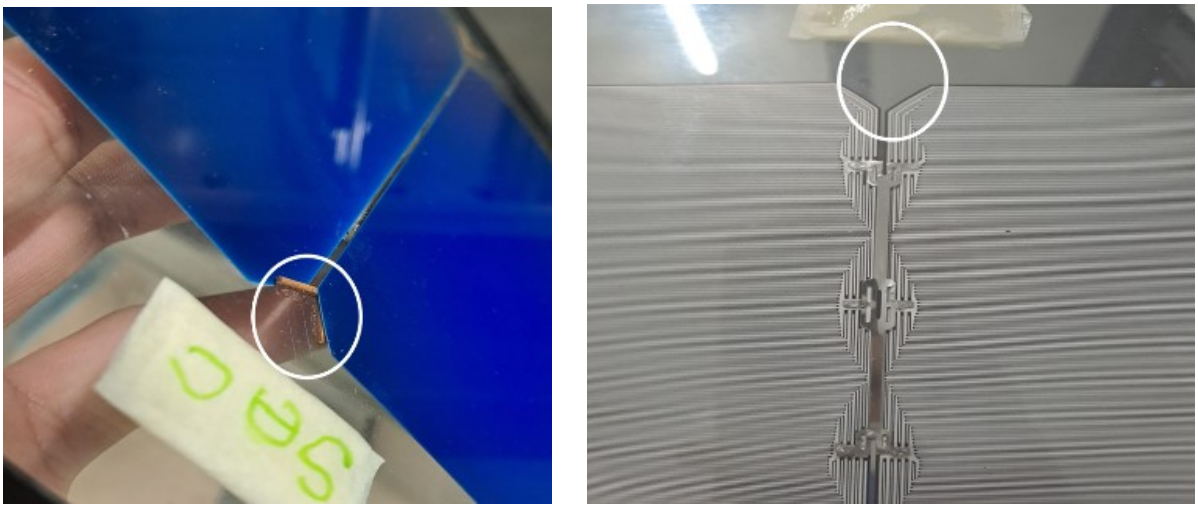

(a) (b)

Figure 6.21: (a) Displaced spacer (highlighted in white) after 25 cycles, and (b) Vacant space created (highlighted in white) due to further displacement of the spacer

The displacement of the spacer within the solar cell module can negatively impact both the performance and structural integrity of the cells. When the spacer shifts and ends up beneath a solar cell during the thermal cycle test, it subjects the cell to mechanical stress, which may lead to non-uniform bending, warping, and the formation of microcracks.

Moreover, the movement of the displaced spacer can interfere with the interconnection between adjacent solar cells. When it touches the dog-bone structure and applies physical force on it, combined with the potential damage to solder joints during thermal cycling, the interconnection between the cells can be compromised.

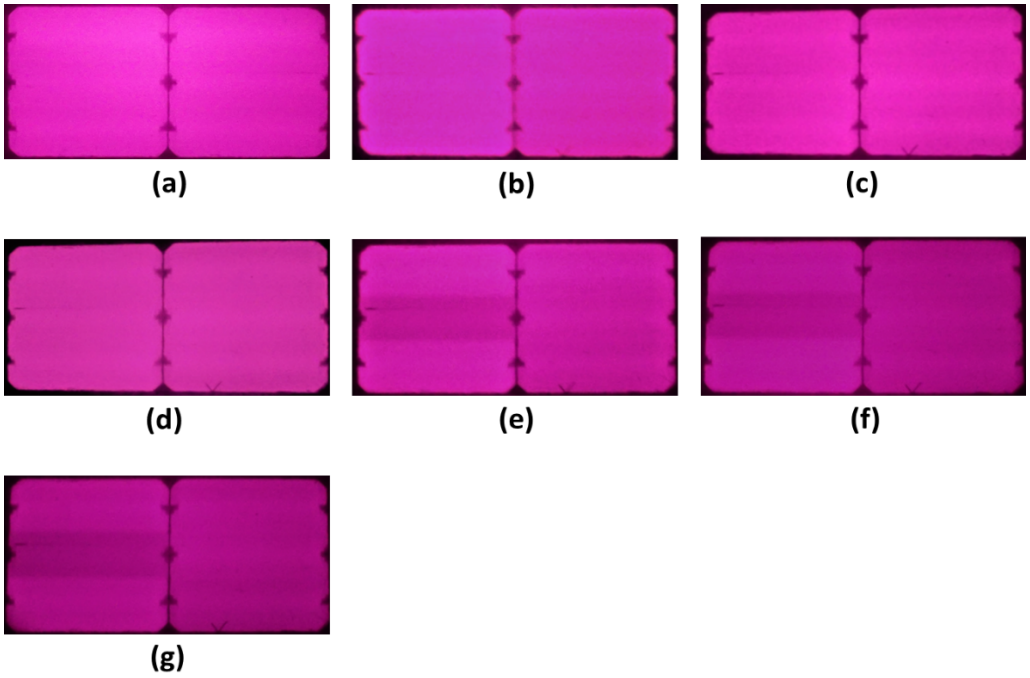

Figure 6.22: EL images of the SnAgCu prototype at (a) TC 0 (b) TC 50, (c) TC 80, (d) TC 115, (e) TC 140, (f) TC 170 and (g) TC 200

Figure 6.22 displays EL images of the SnAgCu prototype captured before and during specific intervals throughout the thermal cycles. The images reveal a decrease in illumination intensity with an increasing number of thermal cycles.

Two specific observations can be deduced from the EL images. Firstly, after TC 50, two cracks become evident - one in the middle region of the left-sided solar cell and another on the bottom region of the right-sided solar cell. The possible reasons for these cracks are the displacement of the spacer along with warping. Secondly, the middle section of the left-sided solar cell experiences a noticeable reduction in illumination intensity after 140 thermal cycles.
As stated in Sections 6.3 and 4.1, it is possible that there are multiple factors including damaged solder joints contributing to the darkened middle region.

Table 6.13: Performance characteristics exhibited by the SnAgCu prototype at distinct time intervals during the Thermal cycle test

Thermal Cycles	0	50	80	115	140	170	200
SnAgCu P_{max} (W)	6.60	6.50	6.43	6.37	6.32	6.32	6.25
I_{sc} (A)	5.90	5.94	5.78	5.80	5.75	5.79	5.76
V_{oc} (V)	1.389	1.395	1.396	1.394	1.393	1.394	1.391

According to Table 6.13, it can be observed that the maximum power output of the SnAgCu prototype decreases as the number of thermal cycles increases. These observations can be attributed with the reasons mentioned earlier regarding the EL image observations. It is crucial to note that, similar to other prototypes constructed following the Biosphere Solar PV module structure, this prototype also exhibits cell warping, leading to non-uniform illumination and potential measurement errors during I-V measurements.

The I_{sc} demonstrates noticeable fluctuations in its measured values throughout the thermal cycle test, ultimately showing a reduction towards the end of the test. This behavior can be linked to the reasons mentioned for the observations in EL images along with the aspect of non-uniform illumination mentioned previously. On the other hand, the V_{oc} displays minor fluctuations.

6.4.6 EVA prototype

As descrived in section 5.5, the primary objective of creating the EVA prototype was to establish an industrial standard reference to serve as a basis for comparing other prototypes. During the thermal cycle test, the EVA prototype displayed only one prominent observation. Specifically, cracks were observed on the back-side glass after TC 115, situated close to both the busbar and the edge of the solar cell, where the dog-bone connects it to the busbar (as illustrated in Figure 6.23).

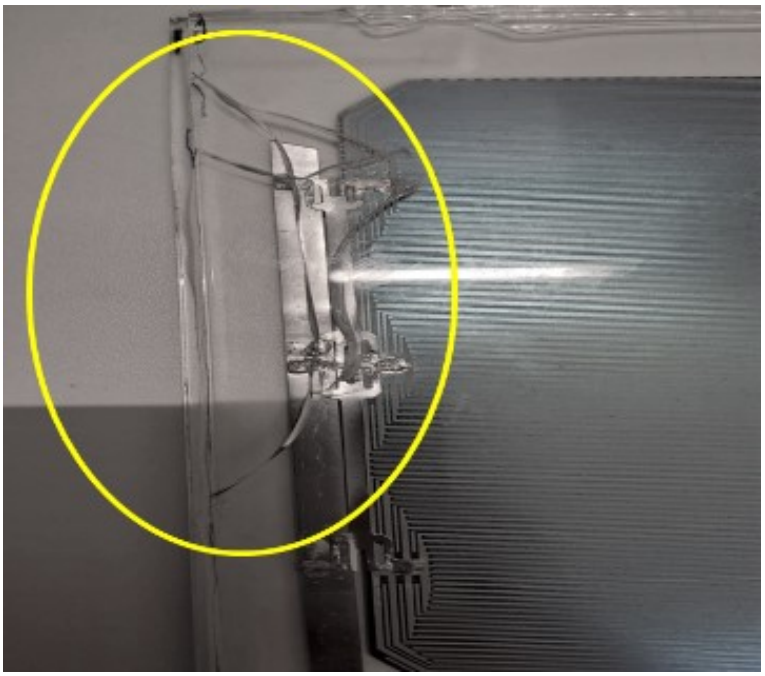

Figure 6.23: Glass cracking observed in EVA prototype (highlighted in yellow)

The cracks observed in the prototype's glass can be a result of various contributing factors such as the high lamination temperature of over 200°C. This temperature exceeded the typical requirement of 150°C due to a malfunction in the laminator's temperature sensor, which was discovered during the ongoing thermal cycle tests.

The elevated temperature can cause thermal stress, leading to differential expansion of the materials, ultimately resulting in the formation of cracks. Moreover, the repeated thermal cycling during the test can further intensify the thermal stresses on the prototype, causing the cracks to grow. It's possible that insufficient EVA bonding and potential manufacturing defects also played a part in the occurrence of these cracks.

Cracks found on the back-side glass of a solar cell, particularly in critical regions such as the busbar and cell's edge, can have a substantial negative impact on its performance. These cracks can degrade the mechanical structure of the cell and have the potential to spread over time due to various mechanical and environmental stresses. They can disrupt the flow of electrical current, and add extra series resistance by degrading the contact regions of the dog-bone and the solar cell. Furthermore, the presence of cracks can compromise the protective encapsulation, making the cell susceptible to moisture infiltration and material degradation.

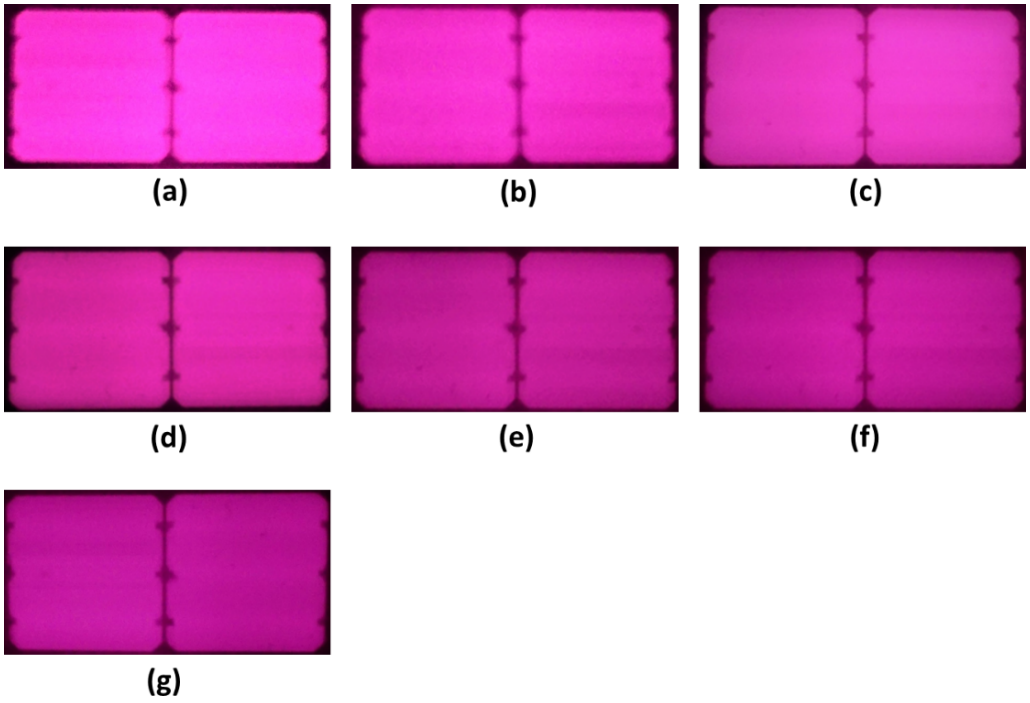

Figure 6.24: EL images of the EVA prototype at (a) TC 0 (b) TC 50, (c) TC 80, (d) TC 115, (e) TC 140, (f) TC 170 and (g) TC 200

Figure 6.24 depicts the EL images of the EVA prototype captured at specific intervals during the thermal cycle test. Based on this Figure, it can be observed that the brightness of the captured EL images of the EVA prototype decreases as the number of thermal cycles increases. This phenomenon can be explained by the factors discussed in sections 6.3 and 4.1, including potential material degradation and solder joint deterioration caused by the mentioned glass cracking issue.

Table 6.14: Performance characteristics exhibited by the EVA prototype at distinct time intervals during the Thermal cycle test

Thermal Cycles	0	50	80	115	140	170	200
EVA P_{max} (W)	6.73	6.62	6.35	6.31	6.29	6.20	6.18
I_{sc} (A)	6.07	6.07	6.01	6.02	6.02	6.01	6.00
V_{oc} (V)	1.394	1.387	1.350	1.350	1.335	1.324	1.320

According to the information in Table 6.14, it can be inferred that the maximum power output of the EVA prototype decreases as the number of thermal cycles increases. This decline can be attributed to the factors such as warping of solar cells, moisture induced degradation previously mentioned in Section 6.3 and decreased shunt resistance along with increased series resistance mentioned in Section 4.1.

The I_{sc} values exhibit minimal fluctuations compared to the other prototypes and demonstrate a slight decrease towards the end of 200 thermal cycles, unlike the other prototypes. This difference may be due to the absence of EVA lamination in the other prototypes, leading to noticeable warping of their solar cells. As mentioned earlier, such warping can cause damage to the solar cell structure and the optical texture which can lead to decreasing short circuit current.

On the other hand, the V_{oc} values exhibit a significant declining trend with the increasing number of thermal cycles. Besides the reasons mentioned for the observations in EL images, another potential explanation for this trend in V_{oc} could be an increase in the saturation current (I_o) within the solar cells [42].

Taking into account the Shockley diode equation 2.2, and adapting it for the V_{oc} and I_{sc} conditions, we obtain the following expressions:

$$V_{oc} = \frac{nKT}{q} ln\left(\frac{I_{ph}}{I_o}\right) \tag{6.3}$$

$$I_{sc} = I_{ph} \tag{6.4}$$

From equation 6.3, we can infer that the V_{oc} of a solar cell is inversely proportional to the saturation current (I_o). On the other hand, from equation 6.4, it can be deduced that the I_{sc} of a solar cell is not dependent on the saturation current.
The rise in saturation current may be linked to structural changes within the cell resulting from thermal cycling and the previously mentioned concern regarding higher lamination temperatures.

6.4.7 Comparison of Power Loss

Figure 6.25a illustrates the maximum output power (P_{max}) for each prototype as a function of the number of thermal cycles. Meanwhile, Figure 6.25b displays the percentage power loss for each prototype against the number of thermal cycles. The percentage decrease in P_{max} is computed by subtracting the P_{max} measured for the prototype at a specific thermal cycle from the P_{max} measured for the prototype at TC 0, and then dividing the result by the P_{max} measured for the prototype at TC 0.

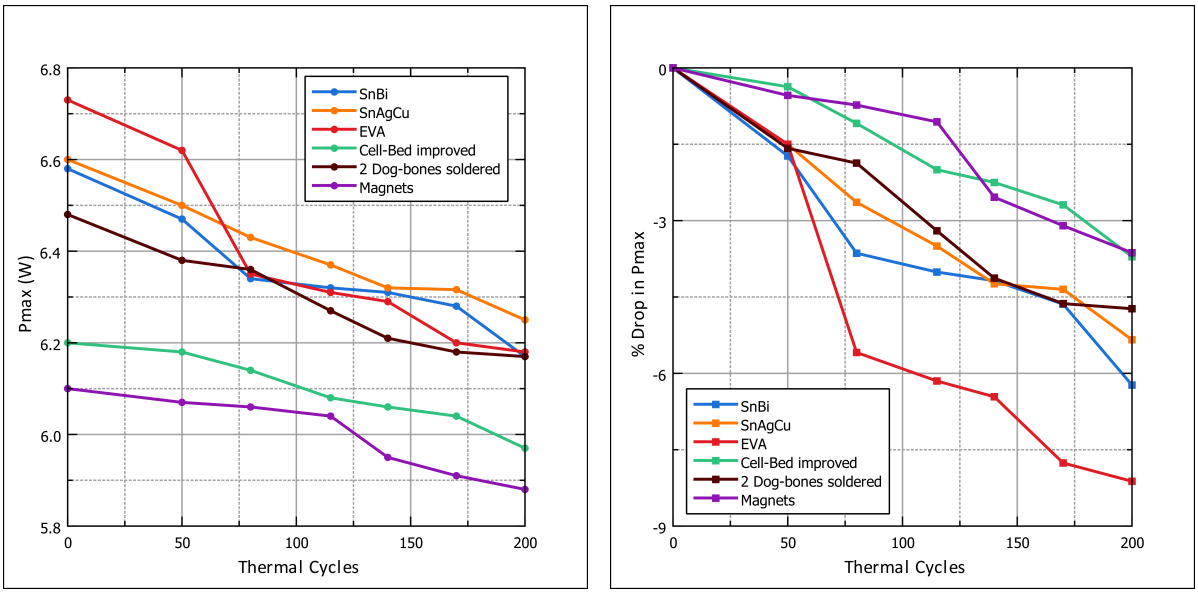

(a) **(b)**

Figure 6.25: (a) P_{max} (W) measured for all prototypes throughout the thermal cycle test, and (b) Percentage power loss of all the prototypes throughout the thermal cycle test

From the graphs shown in Figure 6.25, it can be observed that the EVA prototype experiences a significant decrease in measured power at TC 80, coinciding with a notable drop in V_{oc} during the same thermal cycle, impacting the maximum point voltage (V_{max}) measurements. The V_{max} decreases from 1.18 volts before the thermal cycle test to 1.1 volts after TC 80. The SnAgCu prototype shows a comparatively lower decline in measured power. In contrast, the SnBi prototype exhibits three sharp drops in measured power at TC 50, TC 80, and TC 200, with relatively smaller declines during other intervals. The 2 Dog-bones soldered prototype displays noticeable declines in measured power at TC 50, TC 115, and TC 140. The Cell-Bed improved prototype demonstrates minimal decline in measured power, despite facing challenges such as the PETG strip loosening, dog-bone displacement, and solar cell warping. Similarly, the Magnet prototype also exhibits minimal decline in measured power, despite a decrease in V_{oc}. The V_{max} remains constant (1.1V) before and during the thermal cycles in the Magnet prototype. This can be attributed to the strong contact pressure exerted by the magnets, minimizing any structural changes in the dog-bone due to thermal expansions and contractions.

The trends concerning percentage power loss observed in Figure 6.25b reciprocate with the trends observed in Figure 6.25a.

Figure 6.26a illustrates the percentage variation in P_{max} for the prototypes at TC 0 and TC 200 concerning the P_{max} of the EVA prototype. Meanwhile, Figure 6.26b depicts the equivalent comparison but with respect to the P_{max} of the SnAgCu prototype.

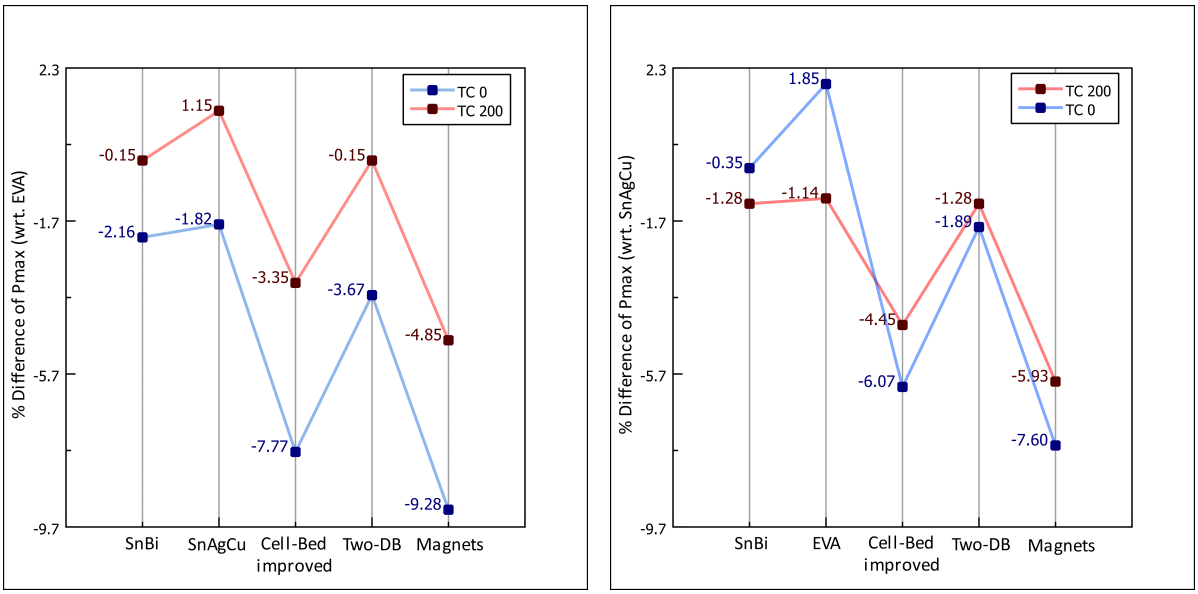

(a) **(b)**

Figure 6.26: (a) Percentage difference in P_{max} at TC 0 and TC 200 with respect to P_{max} of the EVA prototype, and (b) Percentage difference in P_{max} at TC 0 and TC 200 with respect to P_{max} of the SnAgCu prototype

Based on Figure 6.26a, it is evident that the percentage difference in P_{max} tends to decrease at TC 200 in most prototypes, except for the SnAgCu prototype, which experiences a rise in the percentage difference at TC 200, in contrast to the drop observed at TC 0. This inconsistency can be attributed to the substantial decrease in P_{max} of the EVA prototype when compared to the other prototypes, as shown in Figures 6.25a and 6.25b.
The key takeaway from this observation is that after 200 thermal cycles, both the SnBi prototype and the 2 Dog-bones soldered prototype display the lowest percentage difference in P_{max}, reaching the same percentage difference as their measured P_{max} becomes identical (6.17 W) after the 200 thermal cycles.

Figure 6.26b demonstrates a comparable pattern of decreasing percentage difference for most prototypes, except for the SnBi prototype and the EVA prototype. The SnBi prototype displays an increasing difference, with the drop in measured P_{max} rising from 0.02 W at TC 0 to 0.08 W after TC 200. Similar to the trend shown in Figure 6.26a, the percentage difference is at its lowest for both the SnBi prototype and the 2 Dog-bones soldered prototype, among the prototypes with disconnectable interconnection mechanisms. These two prototypes also exhibit the same percentage difference.

CHAPTER 7

Conclusions and Recommendations

7.1 Conclusion

This thesis explores different disconnectable interconnection concepts for Biosphere Solar's PV modules. The study explores four main concepts: the use of low melting point solder alloys for desolderable interconnections, creating connection and disconnection by melting contact regions between interconnection wires, integrating contact pressure mechanisms in the polymer-based cell-bed used for holding the solar cells, and implementing magnetic force-based contact pressure interconnections.

The Sn42Bi58 solder alloy exhibits promising results as a suitable option for desolderable interconnections based on a single dog-bone. This is due to its lower melting point, which reduces the physical force required to separate the dog-bone from the solar cell. This ensures successful desoldering without the risk of cracks, unlike the standard Sn96.5Ag3.0Cu0.5 alloy.

Using two dog-bones to link solar cells in series through melted tin coating at overlapping points is an easier disassembly method than single dog-bone soldering with Sn42Bi58. This is because the points where heat is applied to disconnect and physically separate the dog-bones are farther from the solar cells, unlike the closer points in the single dog-bone desoldering process.

The enhanced cell-bed design, incorporating a screw-based contact pressure mechanism, addresses initial shortcomings of the cell-bed design with a slider-based interconnection mechanism. This results in significantly higher efficiency and improved overall performance of the prototype compared to the prototype consisting of the cell-bed with a slider mechanism.

Despite facing challenges in aligning the magnets properly during assembly due to the magnetic strength of neodymium magnets, the magnetic force-based interconnection proves relatively easy to disassemble. However, issues such as misalignment of the magnets were observed.

The I-V measurements of the prototypes emphasize the SnBi prototype as the most efficient before undergoing thermal cycle testing, closely followed by the two dog-bones soldered prototype. A significant observation from these measurements is that interconnection mechanisms relying on solder joints outperform those based on contact pressure, most likely due to the uniform contact created by solder joints. Another notable finding from the interconnection design analysis is that the length of the interconnection should be minimized to enhance electrical performance, this can be related to the formula of series resistance, which indicates that the resistance is directly proportional to the length of the conducting material.

Furthermore, the thermal cycle tests provide valuable insights into the performance and resilience of the various interconnection mechanisms to thermal stresses. There are two key takeaways from this test. Firstly, it was observed that the prototypes without EVA lamination and reduced glass-glass distance exhibited minimal warping of the solar cells, whereas the ones without EVA lamination and increased glass-glass distance displayed significant warping of the solar cells. Another notable observation is that both before and after the thermal cycle tests, the interconnections based on soldering exhibited the highest electrical performance, further corroborating the potential of the desolderable interconnection based on a single dog-bone soldered using the SnBi solder alloy and the desolderable interconnection based on soldering two dog-bones.

7.2 Recommendations

1. Based on the observations of I-V measurements and thermal cycle tests (as described in sections 6.2.9 and 6.4.7), it is evident that the interconnection mechanisms based on soldering a single dog-bone using the SnBi solder alloy and soldering two dog-bones while creating a connection by melting the tin coating between the overlapping contact regions exhibit higher performance and efficiency. Despite the issue of separated contact regions in the 2 Dog-bones soldered prototype during the thermal cycle test (as shown in Figure 6.14b), the electrical performance of the prototype is relatively better compared to the contact pressure mechanism based prototypes. Additionally, this problem can be mitigated by introducing solder joints between the overlapping regions.
   Considering the critical aspect of bismuth supply and its potential impact on manufacturing, the interconnection based on soldering two dog-bones by utilizing the SnCu solder alloy can be an alternative option. The SnCu solder alloy comprises earth-abundant materials making the approach a more sustainable and resource-efficient interconnection method without compromising the overall performance and efficiency of the PV modules.

2. This thesis focuses on testing and prototyping using IBC solar cells. However, subsequent information revealed that Biosphere Solar intends to utilize front contact solar cells and Zebra IBC solar cells in their future PV modules. Therefore, the recommendations derived from this thesis aim to provide research suggestions for the development of modular interconnections specifically designed for front contact solar cells and Zebra IBC solar cells. Two potential research solutions have been identified to establish modular interconnections tailored for each solar cell type.
   For front contact solar cells with front-side metallization and busbars, the approach involves designing a PCB (printed circuit board) that facilitates localized desoldering. Figure 7.1(a) presents an initial PCB schematic, and Figure 7.1(b) illustrates potential internal routing to connect two cells in series.

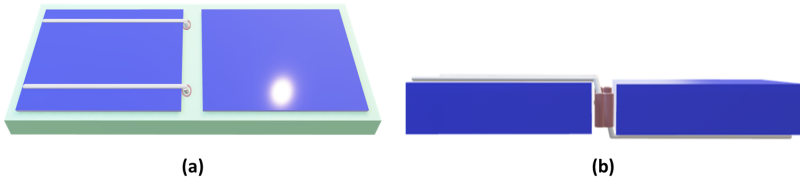

Figure 7.1: (a) Schematic representation of PCB based interconnection concept and (b) Possible routing for connecting the cells in series

Note that, for simplicity, the figures depict cells with only two busbars on one side. The proposed concept in Figure 7.1(b) incorporates copper grooves for soldering the busbars into place, utilizing the SnCu solder alloy. This design allows precise, localized desoldering near the solar cells using specialized tools. An additional advantage of PCB usage lies in its function as a holding mechanism for the solar cells, which can be utilized in the Biosphere Solar PV modules, where EVA lamination is absent.

Zebra IBC solar cells are bifacial cells, and to enable light penetration from beneath the solar cell, transparent PCBs can be employed, as depicted in Figure 7.2. It is important to note that it is essential to research the implications of interconnection designs on the optical performance of the PV modules.

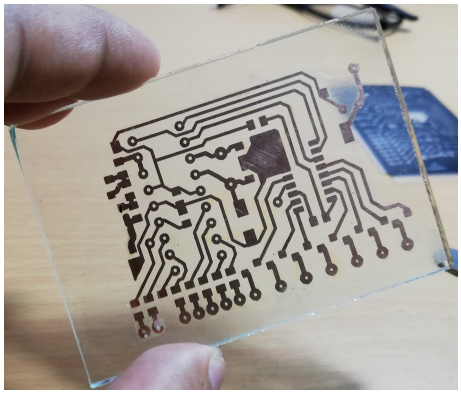

Figure 7.2: Glass PCB [96]

3. Based on the analysis of I-V curves comparing the reference prototype with EVA and the one without EVA (section 6.2.2), it was observed that the absence of EVA in the Biosphere Solar PV modules could result in reduced current generation.

   To address this issue, a potential solution involves texturing the top side of the front glass with an anti-reflective coating to enhance the scattering of incident light. Similarly, a texture can be applied to the bottom side of the front glass. Figure 7.3 provides a schematic representation of this idea, although the textures are not accurately sized for simplicity.

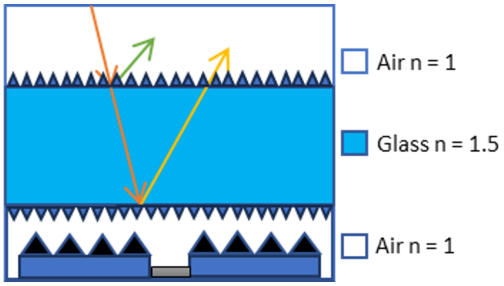

Figure 7.3: Schematic representation of pv module structure with textured glass

   Using texturing techniques can counteract the loss of current generation caused by the absence of EVA, enhancing PV module efficiency and performance.
   However, it is important to note that further research is required to determine which texture works best for the specific application.

4. During the thermal cycle test, it was observed that the solar cells in the prototypes designed following Biosphere Solar PV module structure experienced warping, unlike the EVA prototype, where the cells were not bending because they were kept in place by the two glasses, that are very close to the cells themselves due to the use of EVA. To address this issue while maintaining easy disassembly, a thermoplastic layer can be added in conjunction with EVA.
   The Industrial Technology Research Institute (ITRI) and United Renewable Energy (URE) have introduced a highly recyclable solar panel design featuring a bi-layered compound of thermoset EVA/PO and thermoplastic elastomer (TPE) as encapsulation material. The TPE layer serves as a protective buffer, safeguarding solar cells from cracking during the disassembly process.

   Figure 7.4 illustrates the structure of this module, allowing for effortless component separation and achieving 96% material recovery, including solar cells and front glass. The unique properties of TPE facilitate efficient recycling by isolating the thermoset EVA/PO (Polyolefin), streamlining the entire recycling process [97].

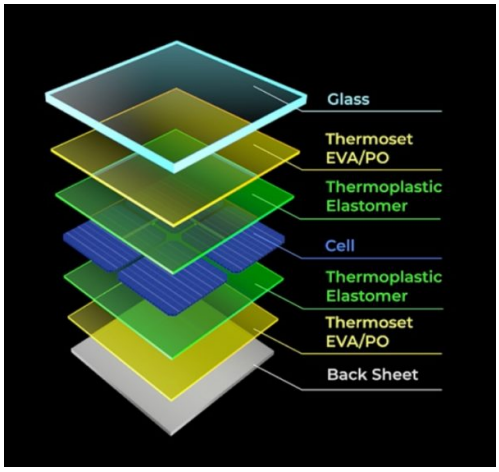

Figure 7.4: Structure of recyclable PV module developed by ITRI and URE [97]

References

[1] United Nations. *Renewable energy – powering a safer future | United Nations — un.org*. https://www.un.org/en/climatechange/raising-ambition/renewable-energy.

[2] Lee Phillips. "9 - Solar energy". In: *Managing Global Warming*. Ed. by Trevor M. Letcher. Academic Press, 2019, pp. 317–332. ISBN: 978-0-12-814104-5. DOI: https://doi.org/10.1016/B978-0-12-814104-5.00009-0. URL: https://www.sciencedirect.com/science/article/pii/B9780128141045000090.

[3] G.K. Singh. "Solar power generation by PV (photovoltaic) technology: A review". In: *Energy* 53 (2013), pp. 1–13. ISSN: 0360-5442. DOI: https://doi.org/10.1016/j.energy.2013.02.057. URL: https://www.sciencedirect.com/science/article/pii/S0360544213001758.

[4] *Solar Energy Solar Power Renewable Energy — futureforall.org*. https://www.futureforall.org/energy/solar_energy.htm.

[5] Andreas Wade et al. "IRENA andIEA PVPS (2016) - End-of-Life Management: Solar Photovoltaic Panels". In: (June 2016).

[6] Xiuwu Zhang et al. "Impacts of lead/zinc mining and smelting on the environment and human health in China". In: *Environmental Monitoring and Assessment* 184.4 (May 2011), pp. 2261–2273. DOI: 10.1007/s10661-011-2115-6. URL: https://doi.org/10.1007/s10661-011-2115-6.

[7] Paul B. Tchounwou et al. "Heavy metal toxicity and the environment". In: *EXS* 101 (2012), pp. 133–164. ISSN: 1023294X. DOI: 10.1007/978-3-7643-8340-4_6.

[8] "Study on Photovoltaic Panels supplementing the impact assessment for a recast of the WEEE Directive". In: (2011).

[9] J.L. Brown. *Environmental economics — Encyclopedia Britannica.com*. 2018.

[10] Iea PVPS Task et al. *End-of-Life Management of Photovoltaic Panels: Trends in PV Module Recycling Technologies End-of-Life Management of Photovoltaic Panels: Trends in PV Module Recycling Technologies Operating Agent*. 2018.

[11] Michele Calì et al. "The Design Value for Recycling End-of-Life Photovoltaic Panels". In: *Applied Sciences (Switzerland)* 12 (18 Sept. 2022).

[12] Chitra et al. "Structural composition and thermal stability of extracted EVA from silicon solar modules waste". In: *Solar Energy* 211 (2020), pp. 74–81. ISSN: 0038-092X. DOI: https://doi.org/10.1016/j.solener.2020.09.039. URL: https://www.sciencedirect.com/science/article/pii/S0038092X20309944.

[13] https://www.ulaginoli.com/author/admin/. *Components of a Solar Photo Voltaic Panel — ulaginoli.com*. https://www.ulaginoli.com/product-introduction-series/components-of-a-solar-photo-voltaic-panel/.

[14] *Researchers at NREL Find Fewer Failures of PV Panels and Different Degradation Modes in Systems Installed after 2000 — nrel.gov*.

[15] Anna Katharina Schnatmann, Fabian Schoden, and Eva Schwenzfeier-Hellkamp. "Sustainable PV Module Design—Review of State-of-the-Art Encapsulation Methods". In: *Sustainability (Switzerland)* 14 (16 Aug. 2022). ISSN: 20711050. DOI: 10.3390/su14169971.

[16] Roland Einhaus et al. "IEC CERTIFICATION AND EXTENDED AGEING TEST OF NICE MODULES Eric Pilat Atomic Energy and Alternative Energies Commission IEC CERTIFICATION AND EXTENDED AGEING TEST OF NICE MODULES". In: (). URL: https://www.researchgate.net/publication/265945583.

[17] *PIB Edge Sealant — sinovoltaics.com*. https://sinovoltaics.com/learning-center/materials/pib-edge-sealant/.

[18] *Figure 7 | Analysis of the Possibility of Using Energy Harvesters to Power Wearable Electronics in Clothing — hindawi.com*. https://www.hindawi.com/journals/amse/2019/9057293/fig7/.

[19] Matthew T. Boyd et al. "Evaluation and Validation of Equivalent Circuit Photovoltaic Solar Cell Performance Models". In: *Journal of Solar Energy Engineering* 133.2 (Mar. 2011), p. 021005. ISSN: 0199-6231. DOI: 10.1115/1.4003584. eprint: https://asmedigitalcollection.asme.org/solarenergyengineering/article-pdf/133/2/021005/5715350/021005_1.pdf. URL: https://doi.org/10.1115/1.4003584.

[20] E. L. Meyer. "Extraction of Saturation Current and Ideality Factor from Measuring Voc and Isc of Photovoltaic Modules". In: *International Journal of Photoenergy* 2017 (2017). ISSN: 1687529X. DOI: 10.1155/2017/8479487.

[21] Fahmi F. Muhammadsharif and Suhairul Hashim. "A Simple and Efficient Determination of the Ideality Factor of Solar Cells and Modules from the Knee Point of the Shunt Resistance Curve". In: *Arabian Journal for Science and Engineering* 48.6 (Apr. 2023), pp. 8217–8225. DOI: 10.1007/s13369-023-07860-3. URL: https://doi.org/10.1007/s13369-023-07860-3.

[22] Arno Smets et al. *Solar Energy*. Cambridge, England: UIT Cambridge, Jan. 2016.

[23] *Series Resistance | PVEducation — pveducation.org*. https://www.pveducation.org/pvcdrom/design-of-silicon-cells/series-resistance.

[24] Fadong Yan et al. "Evaluation of CIGS cell interconnection methods". In: June 2013, pp. 2064–2067. ISBN: 978-1-4799-3299-3.

[25] *Tabbing Ribbons: Design and Purpose — sinovoltaics.com*. https://sinovoltaics.com/learning-center/materials/tabbing-ribbons-design-and-purpose/.

[26] Yongxiang Yang et al. "REE Recovery from End-of-Life NdFeB Permanent Magnet Scrap: A Critical Review". In: *Journal of Sustainable Metallurgy* 3.1 (Sept. 2016), pp. 122–149. DOI: 10.1007/s40831-016-0090-4. URL: https://doi.org/10.1007/s40831-016-0090-4.

[27] Robert Darveaux et al. "Crack initiation and growth in WLCSP solder joints". In: (2011), pp. 940–953. DOI: 10.1109/ECTC.2011.5898624.

[28] Rumen Ogbomo et al. "Effect of operating temperature on degradation of solder joints in crystalline silicon photovoltaic modules for improved reliability in hot climates". In: *Solar Energy* 170 (June 2018). DOI: 10.1016/j.solener.2018.06.007.

[29] Hongtao Ma. "The Influence of Elevated Temperature Aging on Reliability of Lead Free Solder Joints". In: *2007 Proceedings 57th Electronic Components and Technology Conference* (2007). DOI: 10.1109/ECTC.2007.373867.

[30] A. Yeo, Charles Lee, and John Pang. "Flip chip solder joint reliability analysis using viscoplastic and elastic-plastic-creep constitutive models". In: *Components and Packaging Technologies, IEEE Transactions on* 29 (July 2006), pp. 355–363. DOI: 10.1109/TCAPT.2006.875893.

[31] Lukas Biele, Peter Schaaf, and Florian Schmid. "Influence of Contact Pressure on the Specific Electrical Contact Resistance of Copper". In: *IEEE Transactions on Components, Packaging and Manufacturing Technology* 12.6 (2022), pp. 973–980. DOI: 10.1109/TCPMT.2022.3176740.

[32] *IV Curve | PVEducation — pveducation.org*. https://www.pveducation.org/pvcdrom/solar-cell-operation/iv-curve#footnote1_mg6b8i5.

[33] *Solar cell series resistance - solaris-marketing.com — solaris-marketing.com*. http://www.solaris-marketing.com/solar-cell-series-resistance.html.

[34] *Top Contact Design | PVEducation — pveducation.org*. https://www.pveducation.org/pvcdrom/top-contact-design.

[35] *Metal Grid Pattern | PVEducation — pveducation.org*. https://www.pveducation.org/pvcdrom/design-of-silicon-cells/metal-grid-pattern.

[36] Antonin Faes et al. "SmartWire solar cell interconnection technology DISC (Double Side Contacted Cells)-a H2020 project View project Highly mismatched alloys View project SMARTWIRE SOLAR CELL INTERCONNECTION TECHNOLOGY". In: (2014). URL: https://www.researchgate.net/publication/311016229.

[37] Pierre J. Verlinden. *High-efficiency concentrator silicon solar cells*. Ed. by Tom Markvart and Luis Castañer. Oxford: Elsevier Science, 2005, pp. 371–391. URL: https://www.sciencedirect.com/science/article/pii/B9781856174572500159.

[38] Kurias K. Markose, Aldrin Antony, and M. K. Jayaraj. "Solar Cell Technologies: An Overview". In: *Energy Harvesting and Storage: Fundamentals and Materials*. Ed. by M. K. Jayaraj, Aldrin Antony, and P. P. Subha. Singapore: Springer Nature Singapore, 2022, pp. 1–59. ISBN: 978-981-19-4526-7. DOI: 10.1007/978-981-19-4526-7_1. URL: https://doi.org/10.1007/978-981-19-4526-7_1.

[39] *IBC Solar Cells — sinovoltaics.com*. https://sinovoltaics.com/learning-center/solar-cells/ibc-solar-cells/.

[40] *conector especial para células solares SunPower c60. Dog bone. — mrwatt.eu*. https://www.mrwatt.eu/en/shop/photovoltaic-accessories/soldering/special-connector-for-sunpower-c60-solar-cells-dog-bone-connector.html.

[41] *Wiki Factory | Biosphere Solar — https://wikifactory.com/@biosphere-solar*. https://wikifactory.com/@biosphere-solar.

[42] Mounir Bouzguenda et al. "Evaluating solar photovoltaic system performance using MATLAB". In: *2012 1st International Conference on Renewable Energies and Vehicular Technology, REVET 2012* (Mar. 2012). DOI: 10.1109/REVET.2012.6195248.

[43] *Tin - Element information, properties and uses | Periodic Table — rsc.org*. https://www.rsc.org/periodic-table/element/50/tin.

[44] *Eutectic point | chemistry — britannica.com*. https://www.britannica.com/science/eutectic-point.

[45] Paul Vianco and JA Rejent. "Properties of ternary Sn-Ag-Bi solder alloys: Part I—Thermal properties and microstructural analysis". In: *Journal of Electronic Materials* 28 (Oct. 1999), pp. 1127–1137. DOI: 10.1007/s11664-999-0250-4.

[46] Y. Liu and K. N. Tu. "Low melting point solders based on Sn, Bi, and In elements". In: *Materials Today Advances* 8 (Dec. 2020). ISSN: 25900498. DOI: 10.1016/j.mtadv.2020.100115.

[47] Morgana Ribas. *The Printed Circuit Assembler's Guide to... Low-Temperature Soldering*. 2018. ISBN: 9780999864845.

[48] Dr. Alaa Abd El-Rehim and Heba Zahran. "Investigation of microstructure and mechanical properties of Sn-xCu solder alloys". In: *Journal of Alloys and Compounds* (Jan. 2017).

[49] *Expansion coefficient | physics — britannica.com*. https://www.britannica.com/science/expansion-coefficient.

[50] *1.3 Thermal Expansion x2013; General Physics Using Calculus I — pressbooks.online.ucf.edu*. https://pressbooks.online.ucf.edu/phy2048tjb/chapter/1-3-thermal-expansion/.

[51] Morgana de Avila Ribas et al. *COMPREHENSIVE REPORT ON LOW TEMPERATURE SOLDER ALLOYS FOR PORTABLE ELECTRONICS*.

[52] *SAC305 datasheet*. https://www.techsil.co.uk/media/pdf/TDS/MGEN00015-tds.pdf.

[53] *SnCu cte*. https://www.ametek-coining.com/-/media/ametekcoiningecp/v2/files/productdownloadabledocuments/componentswire/solder-wire-product-sheet.pdf?la=en&revision=4687b98e-5241-4e2b-a04e-16463e083e23&hash=D5523901E6D412856CB831E2E69FBAAC.

[54] *SunPower Maxeon Gen II Solar Cells — us.sunpower.com*.

[55] Mulugeta Abtew and Guna Selvaduray. "Lead-free Solders in Microelectronics". In: *Materials Science and Engineering: R: Reports* 27.5 (2000), pp. 95–141. ISSN: 0927-796X. DOI: https://doi.org/10.1016/S0927-796X(00)00010-3. URL: https://www.sciencedirect.com/science/article/pii/S0927796X00000103.

[56] Likun Zang et al. "Wettability of molten Sn–Bi–Cu solder on Cu substrate". In: *Materials Letters* 63 (2009), pp. 2067–2069.

[57] Eimear Deady et al. "Bismuth: Economic geology and value chains". In: *Ore Geology Reviews* 143 (Apr. 2022). ISSN: 01691368. DOI: 10.1016/j.oregeorev.2022.104722.

[58] Yuchao Zhang et al. "Design considerations for multi-terawatt scale manufacturing of existing and future photovoltaic technologies: challenges and opportunities related to silver, indium and bismuth consumption". In: *Energy Environ. Sci.* 14 (11 2021), pp. 5587–5610. DOI: 10.1039/D1EE01814K. URL: http://dx.doi.org/10.1039/D1EE01814K.

[59] *Mineral commodity summaries 2021*. 2021. DOI: 10.3133/mcs2021. URL: https://doi.org/10.3133/mcs2021.

[60] *Mineral commodity summaries 2015*. 2015. DOI: 10.3133/70140094. URL: https://doi.org/10.3133/70140094.

[61] *What is a terminal block? | Significance and Types — electricaleasy.com*. https://www.electricaleasy.com/2018/03/terminal-block-types.html.

[62] Global Connector Technology. *Why Choose FFC / FPC Connectors? | Flat Flexible Cable Connectors — gct.co*. https://gct.co/fr/ffc-connector/why-choose-ffc-solution.

[63] *3pin Quick Connector Cable Clamp Terminal Block Spring Connector Wire 3pin — digilog.pk*. https://digilog.pk/products/3pin-quick-connector-cable-clamp-terminal-block-spring-connector-wire-3pin.

[64] Anshuman Shrivastava. "1 - Introduction to Plastics Engineering". In: *Introduction to Plastics Engineering*. Ed. by Anshuman Shrivastava. Plastics Design Library. William Andrew Publishing, 2018, pp. 1–16. ISBN: 978-0-323-39500-7. DOI: https://doi.org/10.1016/B978-0-323-39500-7.00001-0. URL: https://www.sciencedirect.com/science/article/pii/B9780323395007000010.

[65] Lee Tin Sin and Bee Soo Tueen. *Injection Molding and Three-Dimensional Printing of Poly(Lactic Acid)*.

[66] K. Jim Jem and Bowen Tan. "The development and challenges of poly (lactic acid) and poly (glycolic acid)". In: *Advanced Industrial and Engineering Polymer Research* 3.2 (2020), pp. 60–70. ISSN: 2542-5048. DOI: https://doi.org/10.1016/j.aiepr.2020.01.002. URL: https://www.sciencedirect.com/science/article/pii/S2542504820300026.

[67] Yanping Du et al. "Evaluation of photovoltaic panel temperature in realistic scenarios". In: *Energy Conversion and Management* 108 (2016), pp. 60–67. ISSN: 0196-8904. DOI: https://doi.org/10.1016/j.enconman.2015.10.065. URL: https://www.sciencedirect.com/science/article/pii/S0196890415009875.

[68] *IEC 62892:2019 | IEC Webstore — webstore.iec.ch*. https://webstore.iec.ch/publication/29329.

[69] Narendra Kumar et al. *Chapter 16 - Plastic pellets*.

[70] "Tensile Behavior of Acrylonitrile Butadiene Styrene at Different Temperatures". In: *Advances in Polymer Technology* 2020 (Apr. 2020), pp. 1–10. ISSN: 0730-6679. DOI: 10.1155/2020/8946591.

[71] Anand B. Balaji et al. "1 - Natural and synthetic biocompatible and biodegradable polymers". In: *Biodegradable and Biocompatible Polymer Composites*. Ed. by Navinchandra Gopal Shimpi. Woodhead Publishing Series in Composites Science and Engineering. Woodhead Publishing, 2018, pp. 3–32. ISBN: 978-0-08-100970-3. DOI: https://doi.org/10.1016/B978-0-08-100970-3.00001-8. URL: https://www.sciencedirect.com/science/article/pii/B9780081009703000018.

[72] Martin J. Brand et al. "Detachable electrical connection of battery cells by press contacts". In: *Journal of Energy Storage* 8 (2016), pp. 69–77. ISSN: 2352-152X. DOI: https://doi.org/10.1016/j.est.2016.09.011. URL: https://www.sciencedirect.com/science/article/pii/S2352152X16301682.

[73] *What Are Neodymium Magnets? | Blog Posts | OneMonroe — monroeengineering.com*. https://monroeengineering.com/blog/what-are-neodymium-magnets.

[74] Jae. *Magnetic Material — precisionmag.com*. https://www.precisionmag.com/index.php/magnetic-material.

[75] *Ferrite Ceramic Magnets magnetpartner.com*. https://magnetpartner.com/how-strong-are-ferrite-ceramic-magnets.

[76] Prabhat K. Tripathy, Kunal Mondal, and Amey R. Khanolkar. "One-step manufacturing process for neodymium-iron (magnet-grade) master alloy". In: *Materials Science for Energy Technologies* 4 (2021), pp. 249–255. ISSN: 2589-2991. DOI: https://doi.org/10.1016/j.mset.2021.07.001. URL: https://www.sciencedirect.com/science/article/pii/S2589299121000240.

[77] *Neodymium - American Chemical Society — acs.org*. https://www.acs.org/greenchemistry/research-innovation/endangered-elements/neodymium.html.

[78] Weibo Gao et al. "Determining the maximum operating temperature of permanent magnets via in-situ measurement of the magnetic flux". In: *Journal of Magnetism and Magnetic Materials* 562 (2022), p. 169744. ISSN: 0304-8853. DOI: https://doi.org/10.1016/j.jmmm.2022.169744. URL: https://www.sciencedirect.com/science/article/pii/S0304885322006485.

[79] *ndfebdatasheet*. https://www.supermagnete.de/eng/data_sheet_S-04-02-N.pdf.

[80] L Rohman et al. "Curie temperatures and critical exponent properties of FePd ferromagnetic materials by data simulations approach". In: *Journal of Physics: Conference Series* 1170.1 (Mar. 2019), p. 012018. DOI: 10.1088/1742-6596/1170/1/012018. URL: https://dx.doi.org/10.1088/1742-6596/1170/1/012018.

[81] Karl Georg Bedrich. *QUANTITATIVE ELECTROLUMINESCENCE MEASUREMENTS OF PV DEVICES*. 2017.

[82] Adeline Sugianto, Rhett Evans, and Weiwei Mao. "Interpreting module EL images for quality control". In: (2014). URL: https://www.researchgate.net/publication/299042226.

[83] Ziyao Meng et al. "Defect object detection algorithm for electroluminescence image defects of photovoltaic modules based on deep learning". In: *Energy Science & Engineering* 10.3 (2022), pp. 800–813. DOI: https://doi.org/10.1002/ese3.1056. URL: https://onlinelibrary.wiley.com/doi/abs/10.1002/ese3.1056.

[84] Peter Würfel and Uli Würfel. *Physics of Solar Cells: From Basic Principles to Advanced Concepts*. Wiley, 2009. ISBN: 978-3-527-41312-6.

[85] *Measurement of Solar Cell Efficiency | PVEducation — pveducation.org*. https://www.pveducation.org/pvcdrom/characterisation/measurement-of-solar-cell-efficiency.

[86] Vitro Architectural Glass. *Key Elements of an IGU — glassed.vitroglazings.com*. https://glassed.vitroglazings.com/topics/key-elements-of-an-igu.

[87] *Keithley*. https://www.testequipmenthq.com/datasheets/KEITHLEY-2651A-Datasheet.pdf.

[88] *Refractive index of Air - Ciddor — refractiveindex.info*. https://refractiveindex.info/?shelf=other&book=air&page=Ciddor.

[89] P. Spinelli et al. "Effect of EVA encapsulation on antireflection properties of mie nanoscatterers for c-Si solar cells". In: *IEEE Journal of Photovoltaics* 5 (2 Mar. 2015), pp. 559–564. ISSN: 21563381. DOI: 10.1109/JPHOTOV.2015.2392948.

[90] *Overview of materials for Ethylene Vinyl Acetate Copolymer (EVA), Film Grade — matweb.com*. https://www.matweb.com/search/datasheet_print.aspx?matguid=f34f846b98f1466780dfb3c0e5c0ca82&n=1.

[91] *SnBi datasheet*. https://www.qualitek.com/sn42_bi58_solder_wire_tech_data.pdf.

[92] *Dye Sensitized Solar Cells-Dye Solar Cells-DSSC-DSC Gamry Instruments — gamry.com*. https://www.gamry.com/application-notes/physechem/dssc-dye-sensitized-solar-cells/.

[93] Gerald Kunz and Andreas Wagner. "Internal Series Resistance Determined of Only One IV-Curve under Illumination". In: (2004), pp. 7–11. URL: https://api.semanticscholar.org/CorpusID:219629809.

[94] Christian H Schiller et al. "Accelerated TC test in comparison with standard TC test for PV modules with ribbon, wire and shingle interconnection". In: *Proceedings of the 36th EUPVSEC* (2019), pp. 995–999.

[95] Meijun Lu et al. *Optimization of interdigitated back contact silicon heterojunction solar cells by two-dimensional numerical simulation*. July 2009, pp. 001475–001480. DOI: 10.1109/PVSC.2009.5411332.

[96] *PCB on GLASS — instructables.com*. https://www.instructables.com/PCB-on-GLASS/.

[97] *Taiwanese consortium develops easily recyclable solar module — pv-magazine.com*. https://www.pv-magazine.com/2022/11/17/taiwanese-group-develops-recyclable-solar-panel/.

[98] Angela De Rose et al. *INTERCONNECTION OF SILICON HETEROJUNCTION SOLAR CELLS BY INFRARED SOLDERING-SOLDER JOINT ANALYSIS AND TEMPERATURE STUDY*.

[99] Chi-ming Lai, Chi-Hung Su, and Keh-moh Lin. "Analysis of the thermal stress and warpage induced by soldering in monocrystalline silicon cells". In: *Applied Thermal Engineering* 55.1 (2013), pp. 7–16. ISSN: 1359-4311. DOI: https://doi.org/10.1016/j.applthermaleng.2013.02.028. URL: https://www.sciencedirect.com/science/article/pii/S1359431113001336.

[100] Charles Ayieko et al. "Controlled Texturing of Aluminum Sheet for Solar Energy Applications". In: *Advances in Materials Physics and Chemistry* 05 (Jan. 2015), pp. 458–466. DOI: 10.4236/ampc.2015.511046.

[101] Matthias Leitner et al. "Thermophysical Properties of Liquid Aluminum". In: *Metallurgical and Materials Transactions A: Physical Metallurgy and Materials Science* 48 (6 June 2017), pp. 3036–3045. ISSN: 10735623. DOI: 10.1007/s11661-017-4053-6.

Appendix

Appendix A
A Testing contact-less soldering techniques

Biosphere Solar is presently in the process of establishing their own manufacturing and assembly facility. To enhance the scale of their soldering operations. IR soldering has been utilized in the PV sector and examined by researchers to assess its technical viability for interconnecting diverse types of solar cells. [98].

After consulting with the core-team members of Biosphere Solar, it was decided to conduct a trial using an IR lamp provided by Ushio, Germany. The trial period for the IR lamp was limited. Due to the requirement of a 3-phase supply with a current of 32 Amps, the setup had to be tested in the store room of the Green Village located at the TU Delft campus.

Figure 5 depicts the setup, including the control box (a) connected to the power supply (b) and the lamp (c), which incorporates a ventilation fan.

Figure 5: IR lamp setup at The Green Village.

This soldering technique utilized the solder paste form of the identical low temperature solder alloy Sn42Bi58 with the same melting point - 138° C.
Figure 6 shows the solder-paste applied on the contact regions on the rear-sides of two IBC solar cells.

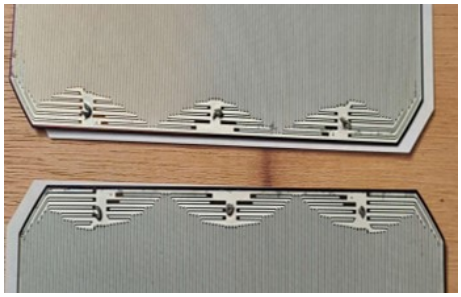

Figure 6: Application of Sn42Bi58 solder paste on the contact areas located at the rear surface of the IBC solar cells.

The datasheet from the lamp suppliers did not provide a temperature profile. However, the setup

included a control box (depicted in Figure 5) with a knob ranging from 1 to 10, allowing adjustment of the IR lamp's light intensity and consequently altering the temperature. Due to limited availability of the lamp during the trial period, there was no opportunity to employ a thermal camera or thermometer for temperature measurements.

Initially, the knob was set to 1, but even after 10 minutes, the solder paste showed minimal melting, and the dog-bone remained unsoldered. Increasing the knob setting to 2 also failed to achieve soldering, with slight melting observed after 10 minutes of exposure. Eventually, when the knob was set to 3, the dog-bone was soldered within 15 seconds. However, cell warping occurred before soldering of the dog-bone with visible changes in the structure typicially starting from 2 seconds after the knob was set to 3 as depicted in Figure 7

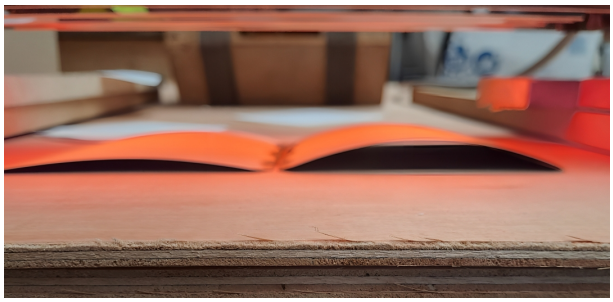

Figure 7: IBC solar cells with dog-bone positioned atop solder joints, undergoing soldering under an IR lamp.

According to the provided datasheet [54], Sunpower Maxeon Gen 2 solar cells have monocrystalline structure. The warping observed in monocrystalline silicon solar cells is mainly attributed to variations in the thermal expansion properties of the constituent materials [99]. A research article based on the investigation of the effects of hot-air soldering heat on warping and thermal stress is discussed. The Hot-air soldering employed three temperatures: 400°C, 500°C, and 600°C, with respective average maximum temperatures on the soldering track of around 180-200°C, 200-220°C, and 220-240°C. The solar cell was placed on a pre-heating plate with the temperature of the plate set to 150°C to reduce the thermal mismatch after the hot air-soldering is stopped [99].

Figure 8 in the study presents a graphical representation of the maximum warpage in millimeters versus time in seconds, using a Finite Element Method (FEM) analysis. Notably, irrespective of the temperature, the graph demonstrates consistent behavior, with the maximum warpage exhibiting a non-linear increase until around 10 seconds, followed by a relatively stable trend thereafter. In this stage, the cell and preheating plate reach thermal equilibrium, maintaining a relatively constant degree of warpage without further increase.

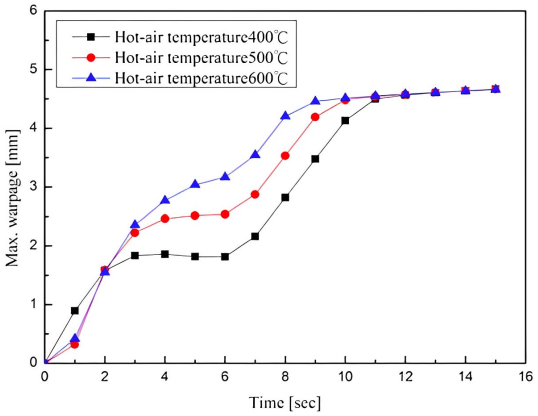

Figure 8: Maximum warping vs Time.
[99]

To address the problem of warping, a solution was implemented by cutting out an aluminum sheet mask from readily available aluminum sheets found in local grocery stores. The mask was placed at a distance above the rear side of the solar cells in order to avoid aluminum from touching the back-contact fingers of the IBC solar cells.

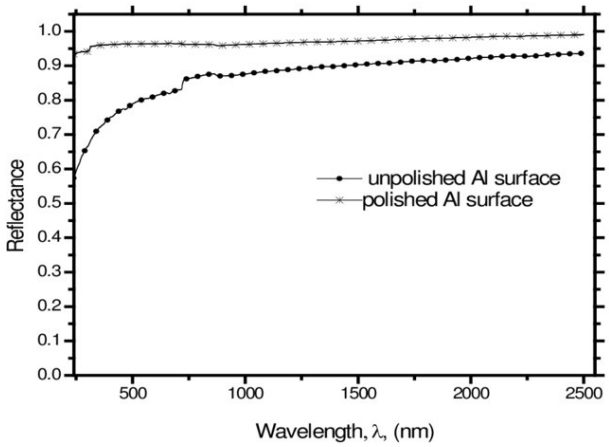

Figure 9: Spectral reflectance measurements were taken for polished and unpolished aluminum surfaces spanning a wavelength range of 300 to 2500 nm.
[100]

Aluminum exhibits excellent reflectivity in the infrared range (700nm to 1000nm). Additionally, the melting point of aluminum is 933.47 K (660.32°C). [101] Figure 9 depicts the reflectance profiles of both polished and unpolished aluminum surfaces across a wavelength range of 300 to 2500nm. The figure clearly demonstrates that polished aluminum displays a reflectivity exceeding 90% in the infrared region of the light spectrum.
Figure 10 illustrates the arrangement of two aluminum sheets positioned at a distance above the solar cells. The placement of these sheets ensures that the solder-contact regions and the dog-bone remain exposed to the heat emitted by the Infrared lamp, while the remaining backside of the solar cells is shielded from the lamp's heat.

Figure 10: Aluminum foil mask placed above solar cells.

Figure 11 showcases the soldering process of the solar cells, where the working is not visibly apparent.

Figure 11: Solar cells soldered below the aluminum mask.

To test the desoldering of the dog-bone under the IR lamp, attempts were made. Although desoldering the dog-bone was feasible, it proved challenging due to the absence of a suitable tool to exert physical force beneath the dog-bone. Automation through contact-based servo-motors could potentially address this issue.

Acknowledgements

First and foremost, I must express my deepest gratitude to my parents, whose relentless hard work and financial support made my dream of pursuing a master's degree possible. Their unwavering love and encouragement have been my guiding light throughout this journey.

I extend my sincerest appreciation to Dr. Patrizio Manganiello, my project supervisor, for his exceptional mentorship and kind-hearted nature. Your open-mindedness and receptivity to ideas made it incredibly easy for me to share my thoughts, doubts and learnings during our meetings. I am deeply grateful for your valuable insights and guidance, as well as the reality checks provided during our discussions on experiments. Your support and approval of my ideas for this thesis have been truly motivating.

I would like to extend my heartfelt gratitude to the exceptional team at Biosphere Solar for their invaluable contributions to my research. Tim, I am deeply thankful for your friendship and patient guidance in teaching me soldering, despite the initial challenges. The moments we spent building the DIY kit and celebrating Christmas dinner at your place in Amsterdam are cherished memories. Siemen, I appreciate your vast knowledge, thought-provoking discussions, and the delightful meals we shared together. Youp, I am thankful for your guidance and support in refining the cell-bed designs. And to Perine, Keshav, Myrthe, and Sam, I am grateful for the camaraderie and the joyful moments we shared.

Special thanks go to individuals from the 3ME department and the PVMD group. Dr. Ivan Buijnsters, Dr. Shoshan Abrahami, Dr. Rudi Santbergen, dr. Malte Vogt, Dr. Mirco Muttillo, Dr. Robin Vismara, Stefaan Heirman, Shuang Hao, Yilong Zhou, and Juan Camilo Ortiz Lizcano, your contributions and discussions have been invaluable in shaping this thesis.

I cannot forget to acknowledge my wonderful friends who have made this journey memorable. The Hoge Veld boys - Sanky, Sathya, and Ayman (Chicha) - thank you for being great friends and for sharing a house filled with laughter and beautiful memories. Salem, your friendship means a lot, thanks for introducing me to middle eastern food. Rahul, the discussions on climate change impacts have been fun. To Palash for being a friendly roommate and to all my other friends, thank you for the cherished memories we have created together.

With this thesis, I embark on a new chapter in my journey. I am excited about the opportunities that lie ahead and look forward to making meaningful contributions to the advancement of renewable energy solutions.

I extend my heartfelt gratitude to each person who has been a part of this incredible academic venture.

Mihir Mahajan
Delft, August 2023